CAPABILITY CHARTS FOR POWER SYSTEMS

A thesis presented for the degree of
Doctor of Philosophy in Electrical Engineering
in the
University of Canterbury,
New Zealand,

by

James Ranil de Silva, B.E.(Hons 1)

March 1987

Mostly for my father,

the late

Dr Fredrick Peter Rienzi de Silva

Abstract

This thesis extends the concept of the traditional synchronous generator capability chart to describe the steady state performance of transmission lines, HVDC links, and entire AC/DC power systems.

Each capability chart depicts an operating region on the complex power plane that represents the real and reactive power that may be supplied to a load from a particular busbar. The boundaries of the operating region are defined by a web of contours that represent the critical operating constraints of the system.

The charts for small systems can be constructed by manipulating the operating equations into a form suitable for drawing loci on the complex power plane. This technique is used in this thesis to construct charts for generators, transmission lines, and HVDC links.

The operating equations of large systems are not easily manipulated, so a different approach is used to construct charts for large systems. This approach involves iterative powerflows and contour plotting to avoid the formulation of explicit closed form locus equations.

Two algorithms for drawing the capability charts of large AC power systems are described. The first algorithm uses a contour tracing technique to plot the constraint loci. The knowledge gained from the use of this algorithm was then used to design the second, faster algorithm that uses a region growing technique to help plot the constraint loci.

Capability charts for large AC/DC systems are also discussed. The operating constraints of the AC/DC converters require special treatment due to discontinuities in the converter operating equations. An offshoot of the work on AC/DC charts is the development of an improved sequential AC/DC powerflow algorithm.

A practical example of the use of the capability charting algorithms is given by drawing charts for a proposed second New Zealand HVDC link.

The capability charting algorithms will make suitable additions to existing power system interactive graphics programs. On-line displays of capability charts in system control centres could also provide useful information to human dispatchers.

List of Contents

Page

Acknowledgements

My thanks to Dr Christopher P. Arnold for his supervision during the three years of research involved in this thesis.

I am also indebted to my employer, the Electricity Division of the Ministry of Energy, who gave me leave to do the work.

Thanks to the staff and postgraduate students at Ilam, particularly Bill Kennedy and Andrew Earl for the efforts they have put into the computing and graphics facilities. Also Professor Josu Arrillaga, Dr Patrick Bodger, Enrique Achadaza, Gordon Cameron, Neville Watson, and Chris Callaghan for their discussions and humour.

Special thanks to my family who completely and utterly approve of this work without actually knowing what it means.

Publications Associated with this Thesis

The following three publications are associated with the research presented in this thesis.

Arnold, C.P., and de Silva, J.R., "A Capability Chart for Power Systems", Second International Conference on Power System Monitoring and Control, Durham, UK, 1986.

de Silva, J.R., and Arnold, C.P., "Capability Charts for Analyzing Power Systems", to be presented at the Conference of the Institute of Professional Engineers New Zealand (IPENZ), 1987.

de Silva, J.R., Arnold, C.P., and Arrillaga, J., "A Capability Chart for an HVDC Link", accepted for publication in the IEE Proceedings-C Generation, Transmission, and Distribution, 1987.

The following paper has also been submitted for publication but has yet to be officially accepted (as of 11th March, 1987).

de Silva, J.R., and Arnold, C.P., "A Simple Improvement to Sequential AC/DC Powerflow Algorithms", submitted to the Electric Energy Systems Journal.

Chapter 1
Introduction

1.1 GRAPHICS, POWER SYSTEMS, AND CAPABILITY CHARTS

An old adage that claims "A picture paints a thousand words" conveys the essence of graphical presentation. A good diagram can be more easily understood than many pages of writing and, in particular, a good graph is preferable to tables of technical data. The appeal of graphical displays has grown as computer based graphics systems have progressively reduced the labour required to produce an effective display. The blossoming popularity of computer graphics is being reflected in the field of power systems as more research effort is committed to the development of graphics software specifically for power system analysis.

The best examples of the use of computer graphics for analyzing power systems are the interactive graphics programs that have been recently developed to model power system operation. Two such programs are IPSA (Interactive Power Systems Analysis) described by Lynch and Efthymiadis (1979) and ADAPOS (Advanced Analyzer of Power Systems) described by Fujiwara and Kohno (1985). These programs allow the user to interactively construct a power system model by drawing the circuit diagram on a graphics terminal. Powerflow, transient stability, and short circuit studies can then be performed with the results appearing alongside the circuit diagram.

Graphical displays of circuits are also commonly used in system control centres to monitor the operation of the network. These displays can be used interactively to directly control circuit breakers and generators. More than a decade of use has proven that graphical displays are beneficial for both modelling and monitoring power systems. Further improvements in power system graphics can be expected from continued research and development.

The particular development of power system graphics that is explored in this thesis involves the drawing of capability charts. The capability charts represent another method of graphically displaying power system performance. The programs used to draw the capability charts are

therefore related to other power systems graphics software and could be profitably included in existing power system interactive graphics packages.

The capability charts are drawn on the complex power plane and define the real and reactive power that may be supplied from a busbar during steady state operation. The power available is depicted by a region on the plane, the boundaries of the region represent the critical operating limits of the system.

The best known example of a capability chart is the operating chart of a synchronous generator as shown in figure 1.1 . The power available from the generator is restricted by the rotor current, stator current, turbine power, and synchronous stability limits. The work discussed in this thesis can be considered to be a generalization of this concept of a generator capability chart. This work can be placed in historical context by considering the origins of capability charts.

1.2 HISTORICAL BACKGROUND

The origins of the power system capability charts lie with the power circle diagrams that were introduced by Philip (1911) and later extended by Evans and Sels (1921) and Dwight (1922). The circle diagrams provide a graphical solution to the problem of relating the voltages and the real and reactive powers associated with a transmission line. A compass and ruler are the only tools required to construct the diagrams, providing that the system studied is restricted to only a single transmission line. This approach has proved to be very successful and is still used to solve transmission line problems.

Szwander (1944) applied the circle diagram approach to drawing a capability chart for round rotor synchronous turbo-generators. Walker (1953) later modified this chart to accommodate the characteristics of salient pole generators. A simple equivalent circuit was used to model the generators to simplify the derivation of equations and aid construction of the chart.

Kimbark (1971) used charts to describe the behaviour of the HVDC

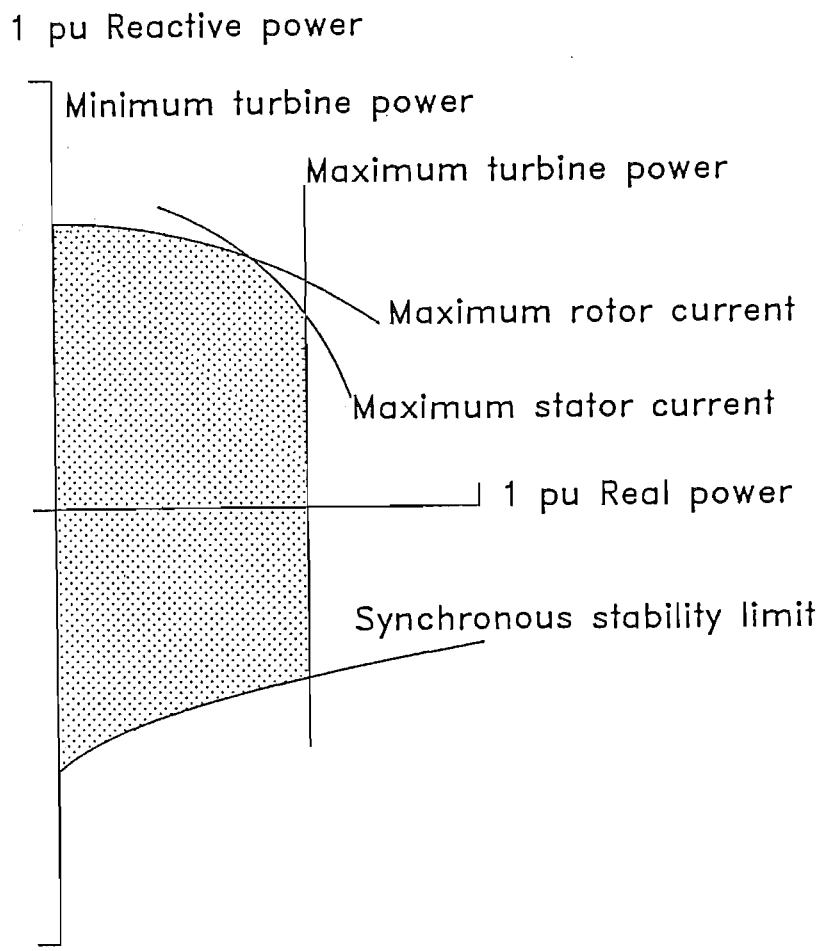

Figure 1.1 Capability Chart of a Synchronous Generator

The shaded operating region represents the real and reactive power that may be supplied by the generator. The boundaries of the region indicate the critical operating limits of the generator.

converters that were just beginning to proliferate at the time. Again a simple system representation was used to simplify the circuit analysis.

All of the charts mentioned so far are restricted to describing small, simple systems because the equations associated with each curve must be explicitly derived. If the curves can be shown to be circles or other simple geometric shapes then the chart can be easily constructed. If larger power systems are considered then the system equations rapidly become much more complicated and prevent the simple derivation of explicit curve equations.

The use of iterative solutions to large power system equations avoids the problem of formulating explicit derivations. A computer becomes necessary to handle the calculation burden that is involved in the iterative algorithms. A graphics output facility is also required to draw curves that are much more complicated than the simple circle diagrams.

Wirth et al. (1983) used the iterative approach to draw contour maps of system eigenvalues on the complex power plane. These contour maps describe the steady state stability of the power system. Price (1984) also used the iterative approach to draw a contour map of the powerflow function for large systems on the complex power plane.

Price's work is probably the closest relative to the capability charting algorithms that are described in this thesis. These algorithms combine the contours associated with the most critical operating limits to form capability charts for large power systems.

1.3 CHAPTER REVIEW

The discussion on capability charts progresses from small, simple systems to larger, more complicated networks. The capability charts of two small systems are discussed in chapter 2. First the standard method of constructing the chart for a synchronous generator is reviewed. A modification of the circle diagram approach is then used to draw the capability chart for a single transmission line.

The capability chart for an HVDC link is described in chapter 3. A growing interest in HVDC links makes this chart particularly useful. The New Zealand Benmore-Haywards HVDC system is used as an example to demonstrate the technique for drawing the chart.

The generator, transmission line, and HVDC link systems all have small, specific configurations. An algorithm for drawing capability charts for larger, general AC systems is described in chapter 4. This algorithm uses an iterative powerflow solution to handle the large number of system equations. The algorithm also incorporates a contour tracing technique to draw the chart boundaries.

The experience gained from drawing a large number of capability charts has suggested possible improvements to the original charting algorithm described in chapter 4. These improvements are incorporated into a fast capability charting algorithm that is described in chapter 5. The fast algorithm uses a region growing procedure to plot the critical operating curves in preference to the contour tracing technique used by the original algorithm.

The capability charts for large AC/DC systems are then examined in chapter 6. The charting algorithms are modified to incorporate the operating constraints of rectifiers and two terminal HVDC links. The AC/DC systems are analyzed by a new sequential AC/DC powerflow algorithm that converges to a solution faster than previous sequential algorithms.

Chapter 7 describes the application of capability charts to help study a proposed second HVDC link between the North and South Islands of New Zealand.

The future prospects of research into capability charts are examined in chapter 8. More detailed modelling of the power system is envisaged to allow a greater variety of operating limits to be portrayed on the charts. Generation cost contour maps are suggested to help minimize operating costs. Consideration is given to the possibility of using optimal powerflows and stochastic powerflows within the capability charting algorithms. The incorporation of capability charts into existing power systems interactive graphics programs is also discussed. Finally, the potential application of capability charts for system monitoring is examined.

Chapter 2
Charts for Simple Power Systems

2.1 INTRODUCTION

The traditional capability chart for a synchronous generator was introduced by Szwander (1944) to display the relationship between the operating limits of a round rotor machine. The steady state operation of a round rotor generator can be described by a few equations and modelled by a simple equivalent circuit. The generator capability chart is easily constructed by manipulating the operating equations into a suitable form for drawing loci on the complex power plane.

The same approach can be used to construct the capability charts for other simple power system circuits such as the transmission line chart and the HVDC link chart that are also described in this thesis.

The operation of larger power systems is described by a large number of equations that cannot be easily manipulated into a suitable form for drawing loci. A different technique is used to construct the charts for these systems and this is treated in chapters 4 to 7 of this thesis.

The capability charts of small, simple systems still retain a valuable role that is not negated by the development of the algorithms to draw charts for larger, more complicated networks. The charts associated with large networks cannot offer the same insights that can be gained from the explicit derivation of locus equations for small systems.

Many of the loci for small systems can be drawn by hand without the assistance of a computer. If facilities are not available to implement the programs for drawing charts for large systems then it may be possible to model the system being studied by a simple equivalent circuit that can be analyzed by hand.

This chapter describes the construction of capability charts for two simple power systems. First the traditional chart for a synchronous generator is reviewed then a chart is developed to describe the performance of a transmission line.

2.2 THE CAPABILITY CHART FOR A SYNCHRONOUS GENERATOR

The capability chart for a round rotor synchronous generator was originally developed by Szwander (1944). The concept was later extended by Walker (1953) to include the operation of salient pole synchronous generators . This section reviews the construction of a chart for a salient pole generator and regards the round rotor generator as a special case of salient pole machines.

Figure 2.1 shows the circuit model of a synchronous generator supplying power to an infinite busbar. The purpose of the capability chart is to describe the range of complex power that may be delivered from the generator to the busbar.

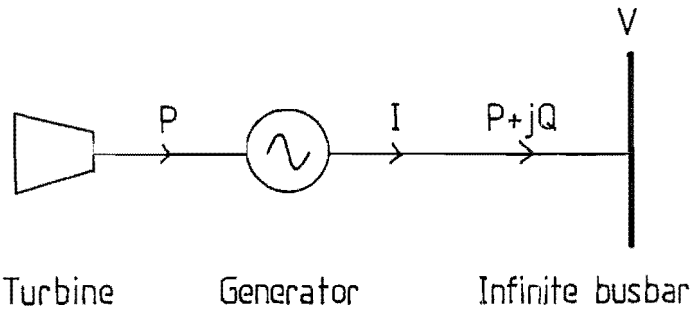

Figure 2.1 Circuit Model of Synchronous Generator

Power from the turbine drives the lossless generator which then delivers the power to an infinite busbar. The synchronous generator capability chart portrays the real and reactive power (P+jQ) that may be supplied from the generator to the infinite busbar.

2.2.1 Simplifying Assumptions

To simplify the analysis the following assumptions have been made ;

1. The generator is connected to an infinite busbar. This is a strong system that is able to maintain a constant voltage and frequency.

2. Only steady state operation is considered. All changes take longer than the machine's transient time constant.

3. Magnetic saturation is neglected. All inductive reactances in the model are therefore constant and independent of current.

4. Losses due to hysteresis, eddy currents, and winding resistance are neglected.

2.2.2 Generator Vector Diagrams

The vector diagram shown in figure 2.2 illustrates the relationship between the voltage, current, and magnetic flux phasors of the generator. The phasors have been superimposed onto a diagram representing the position of the rotor and the position of the stator winding. The current and flux phasors are resolved into components along the direct and quadrature axes of the rotor. This resolution is necessary to deal with the magnetic assymmetry of the salient pole rotor.

The rotor field current produces the flux F_f along the direct axis of the rotor. This rotating flux varies sinusoidally at the stator winding and induces the sinusoidal open circuit terminal voltage E. The instantaneous value of E reaches a maximum when the vector F_f is cutting directly through the stator winding hence E lies along the quadrature axis.

The vector F_f may alternatively be regarded as a complex phasor that represents the component of flux passing perpendicularly through the plane of the stator winding. The induced voltage E is equal to the time derivative of F_f by Faraday's law. Therefore the sinusoidal flux F_f must lead the sinusoidal voltage E by 90 degrees, and E must lie along the quadrature axis. This is in agreement with the previous argument based on flux cutting through the stator windings.

When the generator is loaded the stator current I lags the terminal voltage V by the power factor angle ϕ. The current I can be resolved into a direct axis component I_d and a quadrature axis component I_q. The current I_d produces a flux F_d that lies along the direct axis. The current I_q produces a flux F_q that lies along the quadrature axis. F_d and F_q are added to F_f to produce the effective rotating flux F_e.

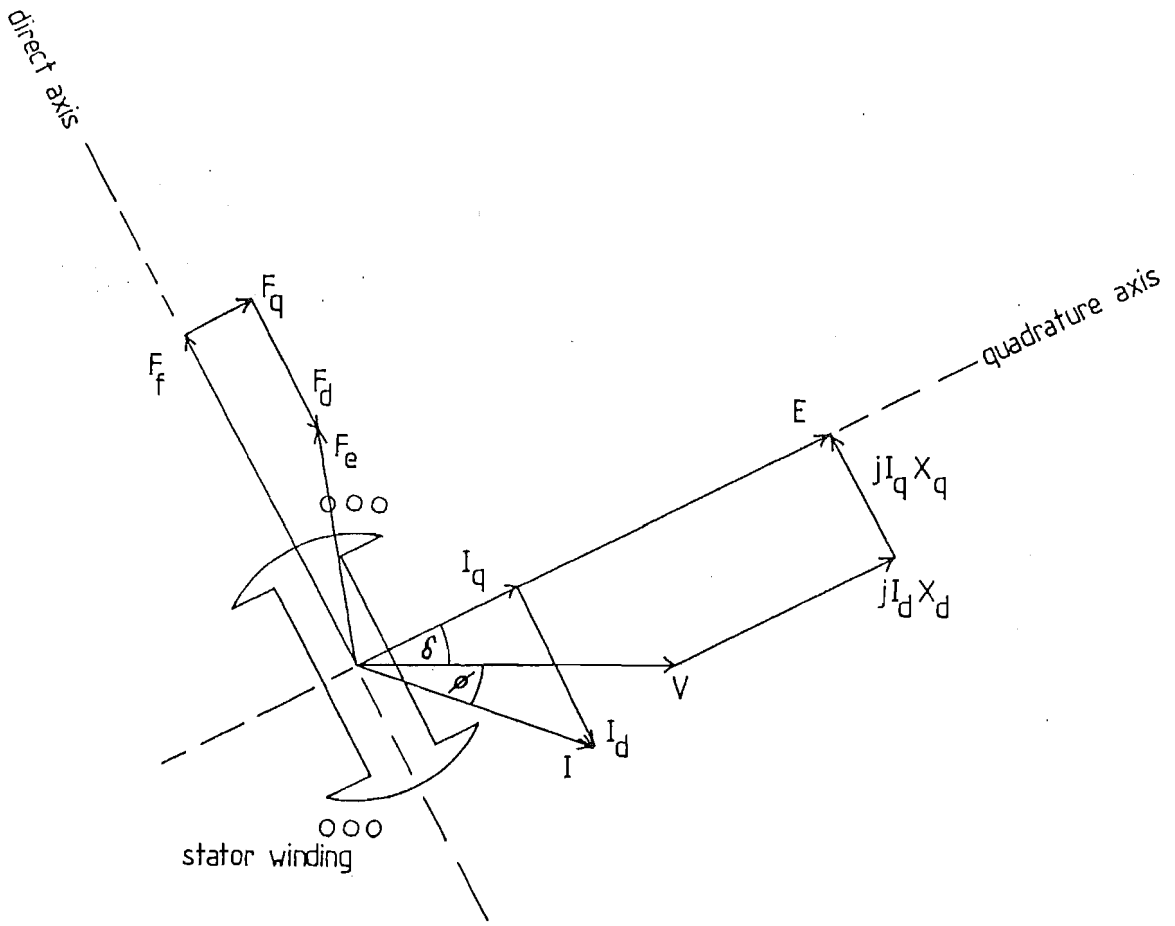

Figure 2.2 Vector Diagram of Salient Pole Synchronous Generator

The voltage, current, and magnetic flux phasors have been superimposed on the rotor and the stator winding. The current and flux phasors have been resolved into components along the direct and quadrature axes of the rotor.

The combined effect of F_d and F_q is called the 'armature reaction' which tends to reduce the magnitude of F_e and lower the induced voltage E . This can be conveniently simulated by one voltage drop due to I_d flowing through a direct axis armature reactance jX_{ad} and another voltage drop due to I_q flowing through a quadrature axis armature reactance jX_{aq}.

In a salient pole machine the direct axis has a lower magnetic reluctance path than the quadrature axis due to the larger air gap along the quadrature axis. The value of jX_{ad} is therefore larger than the value of jX_{aq} . In a round rotor machine the reluctances of the two paths are almost identical and jX_{ad} is considered equal to jX_{aq} .

The two components of the current I both flow through the stator leakage reactance jX_l . This reactance can be added to the armature reactances to form an effective direct axis reactance jX_d and an effective quadrature axis reactance jX_q .

$$jX_d = jX_{ad} + jX_l \qquad (2.2.2.1)$$

$$jX_q = jX_{aq} + jX_l \qquad (2.2.2.2)$$

The vectorial addition of the voltage drops jI_dX_d and jI_qX_q to the terminal voltage V produces the no load terminal voltage E. The angle δ between V and E is called the rotor angle. This angle tends to increase as more power is delivered from the generator.

Inspection of the vector diagram leads to the following steady state operating equations that relate the magnitudes of the vectors.

$$|V|.\sin(\delta) = |I_q|.X_q \qquad (2.2.2.3)$$

$$|V|.\cos(\delta) = |E| - |I_d|.X_d \qquad (2.2.2.4)$$

$$|I|.\cos(\phi) = |I_q|.\cos(\delta) + |I_d|.\sin(\delta) \qquad (2.2.2.5)$$

$$|I|.\sin(\phi) = |I_d|.\cos(\delta) - |I_q|.\sin(\delta) \qquad (2.2.2.6)$$

It is convenient to directly relate E, V, and I without the use of the orthogonal components I_d and I_q. To achieve this, the voltage vectors of figure 2.2 can be modified as shown in the vector diagram of figure 2.3 . The voltage drop jI_qX_q has been extended to jI_qX_d so that the current I can be directly incorporated into the diagram as the voltage drop jIX_d .

The no load voltage E is translated by $jI_q(X_d-X_q)$ to E' and a line is extended backward to intersect with the path of V. As the rotor angle δ changes the angle between E' and $jI_q(X_d-X_q)$ is maintained at 90 degrees. Hence the intersection point of E' and $jI_q(X_d-X_q)$ travels in a circle as δ changes. The diameter of the circle is $|V|(X_d/X_q-1)$.

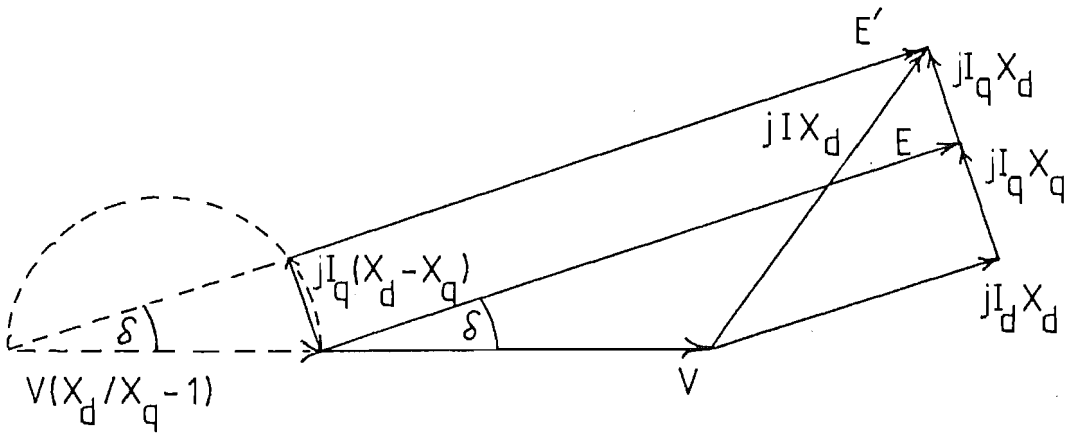

Figure 2.3 Geometric Modification of Generator Voltage Vectors

The original generator voltage vector diagram is modified to show E', V, and jIX_d as part of the sides of a triangle.

This geometrical manipulation serves to portray E' , V and jIX_d as part of a simple triangle. This triangle can be mapped onto the complex power plane by imposing the following transformation on each vector A to map it onto the corresponding vector A' on the complex power plane.

$$A' = |V|.(A/jX_d)^* \qquad (2.2.2.7)$$

Where the symbol * represents complex conjugation.

The triangle on the complex power plane is shown in figure 2.4 . The axes on the plane represent the real power P and the reactive power Q that are delivered from the generator to the busbar.

$$P = |V|.|I|.\cos(\phi) \qquad (2.2.2.8)$$

$$Q = |V|.|I|.\sin(\phi) \qquad (2.2.2.9)$$

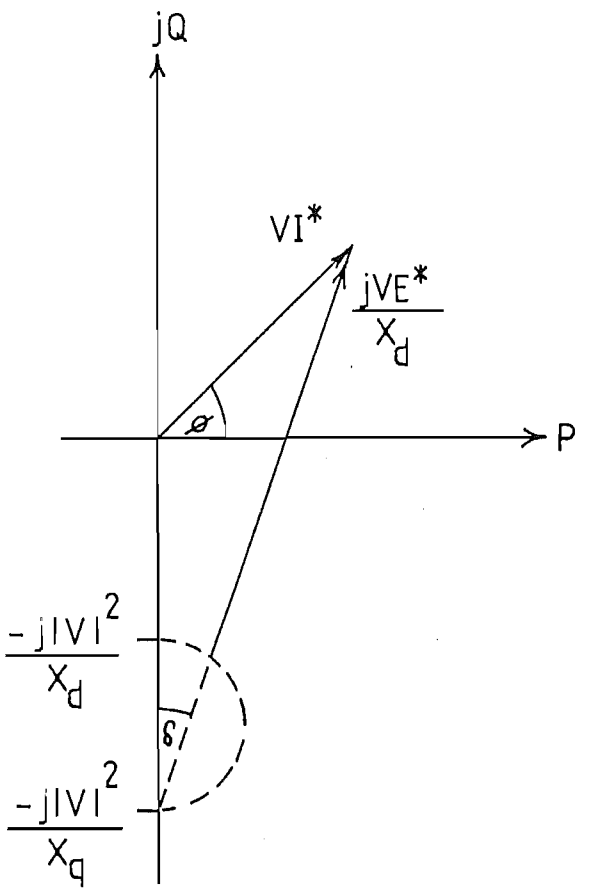

Figure 2.4 Generator Vector Diagram on the Complex Power Plane

The capability chart for the generator can be directly constructed from this diagram.

2.2.3 Construction of the Capability Chart

The vector diagram shown in figure 2.4 is in a suitable form for easily constructing the capability chart of a salient pole generator. A generator with the following specifications is used to demonstrate the construction technique ;

1. Turbine power range of 0 MW to 60 MW
2. Generator apparent power rating of 75 MVA
3. Excitation system capable of providing rotor field current corresponding to a no load voltage range of 0.1 to 2.0 pu
4. Direct axis reactance X_d = 1.5 pu
   Quadrature axis reactance X_q = 1.1 pu
5. Infinite busbar voltage V = 1.0 pu

A 100 MVA power base is used for the per unit system.

The capability chart is illustrated in figure 2.5 and depicts the real and reactive power that can be supplied from the generator to the infinite busbar. Each critical operating constraint is represented by a separate locus on the chart. The shaded area denotes the safe operating region of the generator.

Turbine Power Limits

The generator has been assumed to be lossless so the entire turbine power output is delivered to the infinite busbar. The maximum and minimum turbine power limits are therefore represented as straight vertical lines that intersect the real power axis at 0.0 pu and 0.6 pu .

Maximum Stator Current

The apparent power rating of 75 MVA indicates that the stator current I is limited to 0.75 pu to prevent overheating of the stator windings. If I is fixed at this value the vector VI^* in figure 2.4 traces out a circle of radius $|VI|$ centred on the origin. A small portion of this circle contributes to the boundary of the operating region on the capability chart.

Rotor Current Limits

The upper limit of the rotor field current is determined by the heating of the field winding and the maximum current that can be delivered by the excitation system. The excitation system also imposes a lower limit on the rotor current. The no load terminal voltage E is directly proportional to the field current if magnetic saturation is neglected. Therefore the upper and lower limits of the rotor current also correspond to upper and lower limits on the magnitude of E.

The loci that represent these limits are constructed by maintaining E at its limiting value in figure 2.4 and varying the rotor angle δ. The locus traced out by VI^* is in the shape of a slightly distorted circle called a 'Limacon of Pascal'.

On the capability chart the locus of maximum rotor current limits the reactive power that can be generated and the locus of minimum rotor current limits the reactive power that can be consumed at small leading power factors.

If X_q is increased to the same value as X_d to simulate a similar round rotor generator then the rotor current loci become circles centred on $-j|V|^2/X_d$. The locus of maximum rotor current for a round rotor generator is almost indistinguishable from the locus of maximum rotor current for a salient pole generator. The loci of minimum rotor current are more easily distinguished because the effect of saliency is more pronounced for small values of E.

Steady State Stability Limit

The steady state stability of a generator is determined by its ability to respond to small disturbances without losing synchronism. During these disturbances generators with slow acting exciters will maintain a constant rotor current and a constant open circuit terminal voltage E. Under these conditions the real power output P becomes strongly dependent on the rotor angle δ. The relationship between P and δ can be obtained by first substituting (2.2.2.5) into (2.2.2.8) to give

$$P = |V|.[|I_q|.\cos(\delta) + |I_d|.\sin(\delta)] \qquad (2.2.3.1)$$

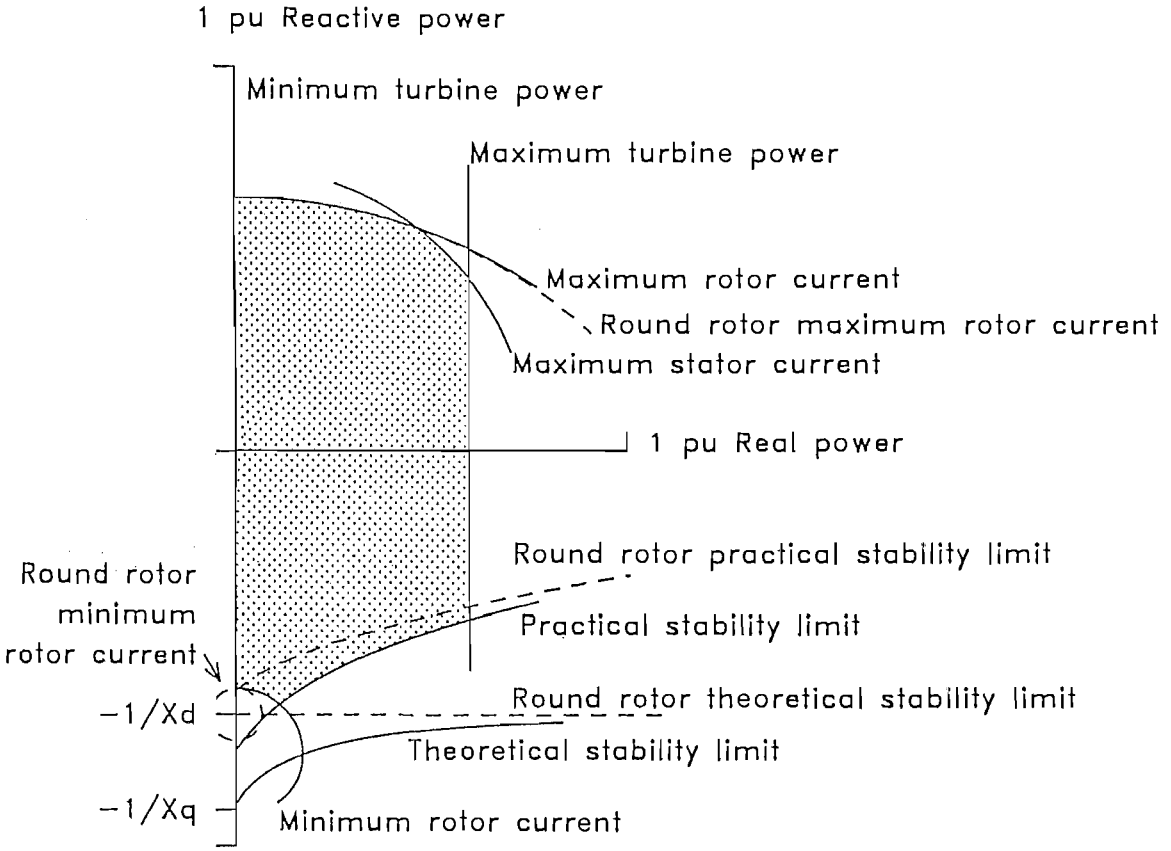

Figure 2.5 Capability Chart of a Salient Pole Generator

The chart portrays the real and reactive power that may be supplied from the generator to the infinite busbar. The shaded area denotes the safe operating region which is bounded by loci that represent the critical operating limits of the generator. The chart of a similar round rotor generator differs in the positions of the rotor current and stability loci. For comparison these round rotor loci are drawn on the chart with dashed lines.

then substitution of I_q and I_d from (2.2.2.3) and (2.2.2.4) gives

$$P = |V|.\left[\frac{|V|.\sin(\delta).\cos(\delta)}{X_q} + \frac{[|E|-|V|.\cos(\delta)].\sin(\delta)}{X_d}\right]$$

$$= \frac{|V|.|E|.\sin(\delta)}{X_d} + \frac{|V|^2.(X_d - X_q).\sin(2.\delta)}{2.X_d.X_q} \qquad (2.2.3.2)$$

A graph of (2.2.3.2) is shown in figure 2.6 . An increase in the power output can be met by an increase in the rotor angle until the peak of the curve is reached. After this point an increase in the rotor angle is accompanied by a decrease in the power output and consequently there is a loss of synchronism.

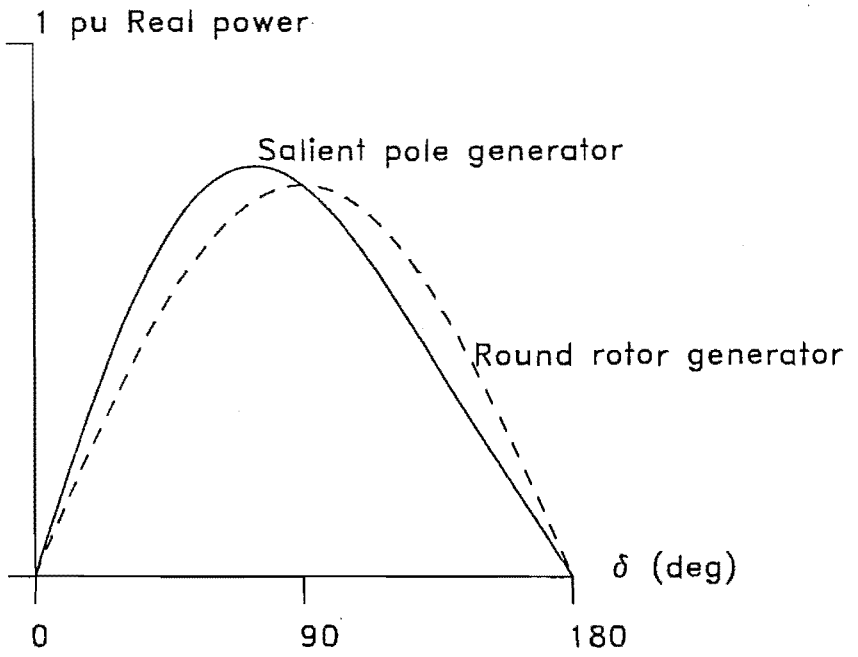

Figure 2.6 Power/Angle Curve for a Synchronous Generator

In a round rotor generator the second term of (2.2.3.2) is zero and the corresponding power/rotor angle graph is sinusoidal. In this case synchronism can be theoretically maintained until the rotor angle exceeds 90 degrees. The locus of the theoretical stability limit for a round rotor generator is shown on the chart as a horizontal straight line intersecting the reactive power axis at $-1/X_d$.

The theoretical stability limit for a salient pole generator is obtained by differentiating (2.2.3.2) with respect to δ to find the maximum power output.

$$\frac{dP}{d\delta} = \frac{|V|.|E|.\cos(\delta)}{X_d} + \frac{|V|^2.\cos(2.\delta).(X_d-X_q)}{X_d.X_q} \qquad (2.2.3.3)$$

This can then be solved for $\cos(\delta)$.

$$\cos(\delta) = \frac{\frac{-|E|.X_q}{|V|.(X_d-X_q)} + \sqrt{\left[\frac{|E|.X_q}{|V|.(X_d-X_q)}\right]^2 + 8}}{4} \qquad (2.2.3.4)$$

The locus of the theoretical stability limit is drawn by gradually varying E in (2.2.3.4) and obtaining the corresponding stability angle δ. The pairs of E and δ values are then used in the vector diagram of figure 2.4 to obtain the corresponding points on the complex power plane.

The theoretical stability limit does not allow for a margin of safety so a practical stability limit is defined. The practical limit allows for a power increase of 10% of the turbine rating before the theoretical limit is reached. Each point on the locus of practical stability is found by choosing a point on the theoretical stability locus and reducing δ whilst keeping E constant until the real power has dropped by 10% of the turbine rating.

The theoretical and practical stability loci for salient pole generators are asymptotic to the corresponding loci for round rotor generators. This behaviour reflects the reduced effect of saliency as E increases.

2.2.4 Summary of Synchronous Generator Chart

The capability chart for a salient pole generator is drawn on the complex power plane and portrays the real and reactive power that may be delivered by the generator to an infinite busbar. The safe operating region of the chart is bounded by loci that represent the critical operating limits of the generator.

The critical operating limits considered are the maximum and minimum turbine power output, the maximum stator current, the maximum and minimum rotor current, and the synchronous stability limit.

The chart for a round rotor generator can be drawn by treating it as a special case of a salient pole machine with the direct axis reactance equal to the quadrature axis reactance.

2.3 THE CAPABILITY CHART FOR A TRANSMISSION LINE

Philip (1911) originally described a chart to graphically analyze the behaviour of a transmission line. This work was later extended by Evans and Sels (1921) and Dwight (1922) and is now commonly referred to as the 'circle diagram' approach to analyzing transmission line behaviour.

The circle diagrams consist of a series of circles drawn on the complex power plane. Each circle represents the locus of real and reactive power that may be delivered by the line at a particular voltage magnitude. These diagrams can easily be constructed by using a compass so they were particularly popular before computer analysis became available and are still used to study the performance of transmission lines.

The circle diagrams can provide the voltage constraint loci that form part of the capability chart for a transmission line. To complete the chart the voltage circles must be supplemented by other loci that represent the remaining operating limits of the line.

2.3.1 Transmission Line Model

The transmission line is modelled by an equivalent pi section as shown in figure 2.7 . The pi section consists of a series impedance Z and a shunt admittance Y at either end of the line. The line delivers power from an infinite busbar at voltage E to a load busbar at voltage V. The shunt admittance F at the load busbar is used to represent a reactive power compensation capacitor or any other device that can be modelled as an admittance.

The complex power delivered to the load is given by

$$S = V.I_3^* - |V|^2.F^* \qquad (2.3.1.1)$$

The load busbar voltage can be related to the supply busbar voltage by considering the voltage drop across the line.

$$E = V + I_2.Z \qquad (2.3.1.2)$$

The current I_2 that produces the voltage drop must be combined with the currents flowing in the shunt admittances to obtain the total line current measured at either end of the line.

$$I_1 = I_2 + E.Y \qquad (2.3.1.3)$$

$$I_3 = I_2 - V.Y \qquad (2.3.1.4)$$

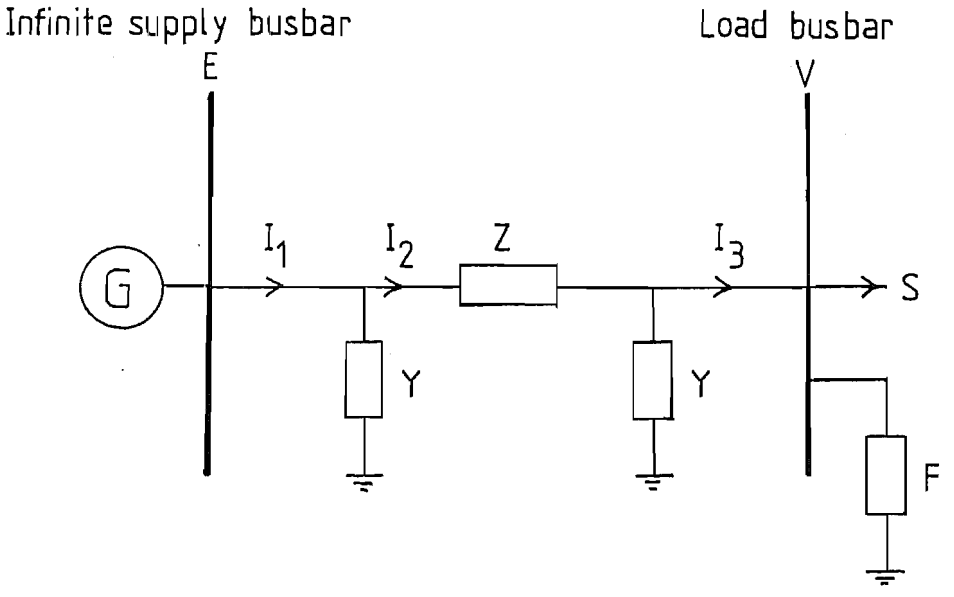

Figure 2.7 Circuit Model of Transmission Line

Equations (2.3.1.1) to (2.3.1.4) form the complete set of operating equations that model the behaviour of the transmission line. These equations can be manipulated to describe loci that represent the operating constraints of the line.

A 33 kV transmission line is used to demonstrate the construction of the chart. The circuit parameters correspond to a power base of 10 MVA.

E = 1 pu
Z = 0.118595 + j0.25911 pu
Y = 0.0 + j0.000216 pu
F = 0.0 + j0.2 pu

2.3.2 Operating Constraints

Each operating constraint of the system must be represented by a separate locus on the capability chart. The constraints that are considered in this transmission line system are

1. Maximum (1.1 pu) and minimum (0.9 pu) voltage at the load busbar.

2. Voltage stability at the load busbar.

3. Maximum current of 1.9 pu entering and leaving the line.

The magnitude of the line voltage and current is known to vary as a hyperbolic function along the length of the line (Steinmetz, 1916). On long lines the maximum voltage and the maximum current may occur at points part way along the line and not necessarily at the busbars at the ends of the line.

To simplify this analysis the transmission line is assumed to be sufficiently short so that the critical voltages and currents do occur at the ends of the line. This assumption gradually loses its validity as the length of the line increases beyond a quarter wavelength (1500 km at 50 Hz) because the hyperbolic function exhibits more maxima with increasing line length.

Load Busbar Voltage Limits

The maximum and minimum acceptable voltage at the load busbar can be represented on the chart by using the circle diagram approach. Equation (2.3.1.1) can be rewritten in terms of V by using (2.3.1.2) and (2.3.1.4).

$$S = V.(E/Z)^{*} - |V|^{2}.(1/Z + Y + F)^{*} \qquad (2.3.2.1)$$

If E is constant and the magnitude of V is constant then (2.3.2.1) describes a circular locus on the complex power plane as the phase angle of V changes. The centre of the circle is at $-|V|^{2}(1/Z+Y+F)^{*}$ and the radius is $|VE/Z|$.

Figure 2.8 shows a series of load busbar voltage circles drawn on the complex power plane. All of the circles fit into a parabolic region on the plane. There are two possible busbar voltage solutions corresponding to each complex load power within the parabola. Only one possible voltage solution exists along the edge of the parabola and no solutions exist outside the parabola.

Of the two possible voltage solutions that can be obtained within the parabola, only the voltage with the larger magnitude is associated with a stable operating point. The smaller voltage is associated with an unstable operating point that will lead to a voltage collapse at the load busbar. The rate of collapse is dependent on the type of load and may occur over a period of several minutes (Venikov and Rozonov,1961 and Weedy,1968).

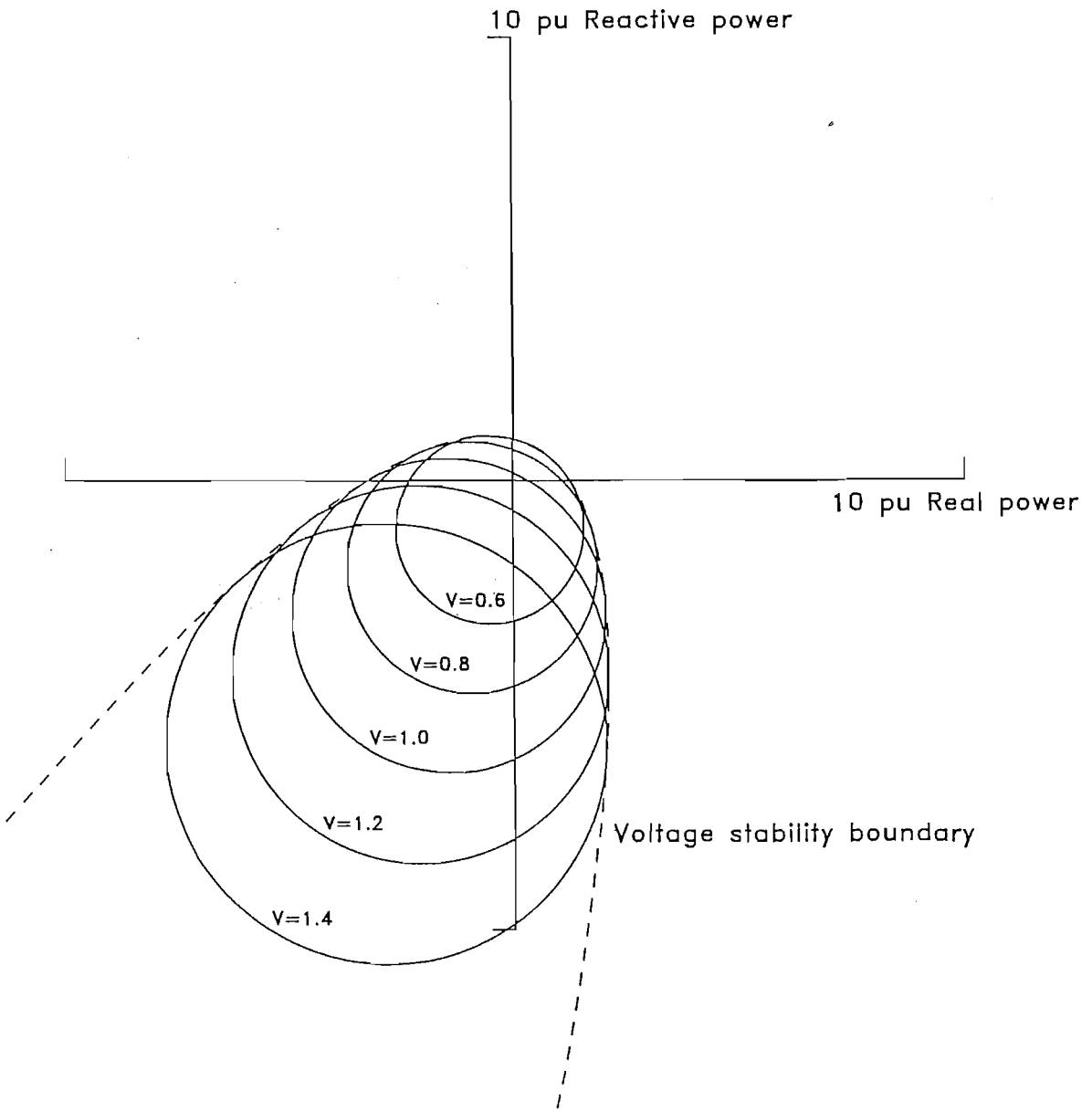

Figure 2.8 Voltage Circle Diagram

Each circle represents a locus of constant voltage magnitude at the load busbar. All of the circles fit into a parabolic envelope which represents the voltage stability boundary.

Voltage Stability

The theoretical boundary of the stable voltage region is defined by the parabolic envelope that contains the voltage circles. It is convenient to form a simple Thevenin equivalent of the circuit model to investigate the nature of the envelope. The Thevenin equivalent shown in figure 2.9 consists of a voltage source E' and a series impedance Z' where

$$E' = E/(1 + Y.Z + F.Z) \qquad (2.3.2.2)$$

$$Z' = Z/(1 + Y.Z + F.Z) \qquad (2.3.2.3)$$

The load busbar voltage V and the load power S both retain the same significance in the Thevenin circuit.

The variables of the Thevenin circuit are related by the equation

$$S = E'.V/Z'^{*} - |V|^2/Z'^{*} \qquad (2.3.2.4)$$

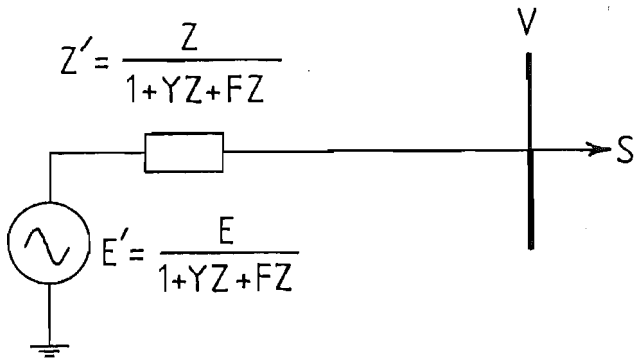

Figure 2.9 Thevenin Equivalent of Transmission Line Model

The parabolic envelope is characterized by the existence of only one solution for V corresponding to a given S in (2.3.2.4). This unique solution can be found by first expressing the complex variables of (2.3.2.4) in terms of their real and imaginary components. E' is used as a real reference vector.

$E' = e + j0$

$S = p + jq$

$V = u + jv$

$Z' = r + jx$

The solution for V in (2.3.2.4) in terms of u and v is then

$$u = \frac{e \pm \sqrt{\{e^2 - 4[pr + qx + (qr-px)^2/e^2]\}}}{2} \qquad (2.3.2.5)$$

$$v = (qr-px)/e \qquad (2.3.2.6)$$

The unique solution for V is identified by a zero valued argument in the square root term of (2.3.2.5) . Hence V lies on the stability boundary if $u=e/2$.

The relationship between the stable and unstable solutions for V is shown in the vector diagram of figure 2.10 . The original supply voltage E is used as the reference vector and the theoretical stability boundary is shown as a straight line bisecting the Thevenin voltage E'. As the theoretical boundary is approached from the stable side the load voltage fluctuations will become more pronounced until a total collapse occurs in the unstable region.

A safety margin is provided by the practical stability boundary that lies parallel to the theoretical boundary and intersects the Thevenin voltage at 0.8E'. The factor of 0.8 is a compromise between the need for a reasonable safety margin and the need to allow for low but stable load voltages. If a greater quality of voltage stability is required then the factor of 0.8 should be increased.

If the shunt admittances are neglected then the Thevenin voltage E' is identical to the original supply voltage E and the stability boundary becomes a vertical line passing through E/2 .

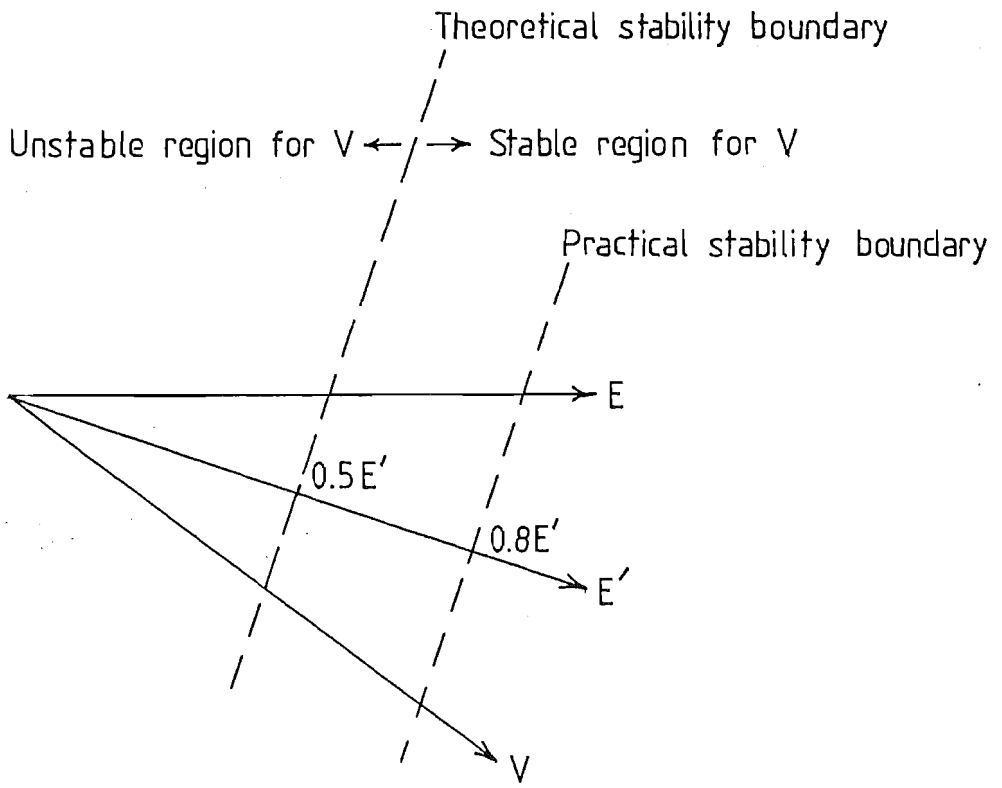

Figure 2.10 Relationship of Stability Boundary to Voltage Vectors

The theoretical voltage stability boundary bisects the Thevenin equivalent voltage vector E' at a right angle. The load voltage vector V should normally lie to the right of the practical voltage stability boundary to allow for a safety margin.

The theoretical and practical voltage stability boundaries are drawn on the complex power plane by gradually shifting V along the appropriate boundary in figure 2.10 and generating a sequence of S values from (2.3.2.4) . Both the theoretical and practical stability boundaries are shown on the capability chart in figure 2.11 .

The maximum and minimum voltage limits are also represented on the capability chart by arcs from the corresponding voltage circles that were drawn in figure 2.8 .

Maximum Transmission Line Current

The maximum line current has been assumed to flow at one of the ends of the line. The current entering the line from the supply end is I_1 and the current leaving the line at the load end is I_3.

The locus of the maximum current I_1 can be obtained by using equations (2.3.1.2) to (2.3.1.4) to rewrite (2.3.1.1) in terms of I_1. This yields

$$S = A.I_1 + B.I_1^* - C.|I_1|^2 - D \qquad (2.3.2.7)$$

where the complex constants A,B,C, and D are given by

$$A = E^*.(2.Y.Z+Y.Y.Z.Z^*+F.Z^*+ F.Y.Z.Z^*)^*$$

$$B = E.(1+Y.Z +Y^*.Z^*+Y.Y^*.Z.Z^*+F^*.Z^*+F^*.Y.Z.Z^*)$$

$$C = Z+Y^*.Z.Z^*+F^*.Z.Z^*$$

$$D = E.E^*.(2.Y+Y.Y.Z+2.Y.Y^*.Z^*+Y.Y.Y^*.Z.Z^*+F+F.Y.Z+F.Y^*.Z^*+F.Y.Y^*.Z.Z^*)^*$$

Equation (2.3.2.7) describes an elliptical locus as the magnitude of I_1 is held constant at its maximum value and the phase angle of I_1 is varied through a full 360 degrees.

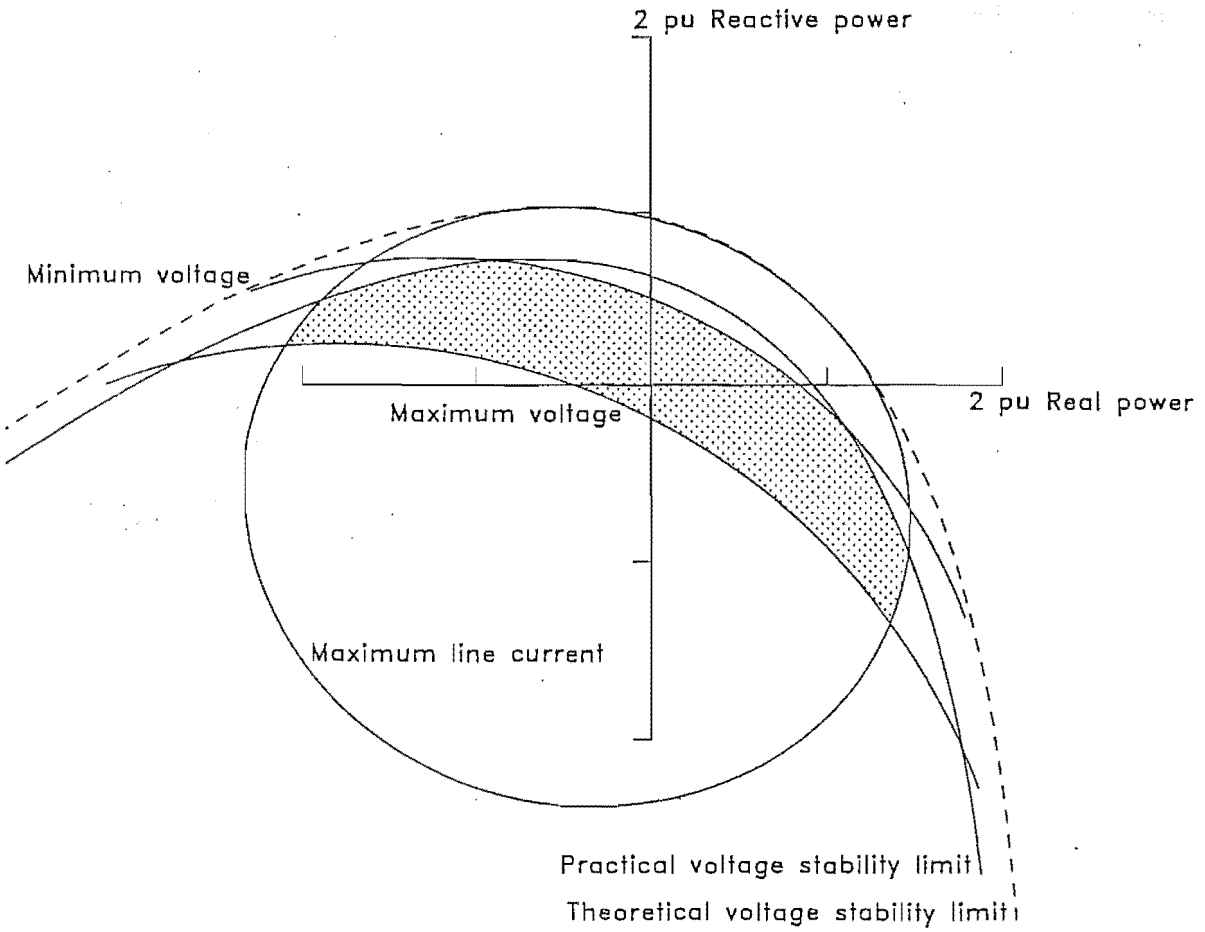

Figure 2.11 Capability Chart of Transmission Line

The shaded area denotes the range of real and reactive power that may be supplied to the load. This area is bounded by loci that represent the critical operating limits of the system.

At the load end of the line the locus of I_3 can be found in a similar fashion by rewriting (2.3.1.1) in terms of I_3. This yields

$$S = A.I_3 + B.I_3^* - C.|I_3|^2 - D \qquad (2.3.2.8)$$

where the complex constants A,B,C, and D are given by

$$A = \frac{E^*.F^*.Z}{|1 + Y.Z|^2}$$

$$B = \frac{E.(1 + Y.Z + F.Z)^*}{|1 + Y.Z|^2}$$

$$C = \frac{Z.(1 + Y.Z + F.Z)^*}{|1 + Y.Z|^2}$$

$$D = \frac{|E|^2.F^*}{|1 + Y.Z|^2}$$

Equation (2.3.2.8) also describes an elliptical locus as the magnitude of I_3 is held constant and the phase angle is varied through 360 degrees. If the shunt admittance F is zero then this locus becomes circular.

The two loci of maximum current are indistinguishable on the capability chart of figure 2.11 . The ellipses become more distinct as the value of the shunt admittances increases.

2.3.3 Capability Chart on the Admittance Plane.

If the load is a soft admittance load rather than a stiff constant power load then it is more appropriate to draw the capability chart on the complex admittance plane instead of the complex power plane. The chart on the admittance plane is shown in figure 2.12 .

The maximum and minimum load voltage limits and the maximum line current limit are shown on the admittance chart. A voltage stability limit is not shown because the voltage collapse phenomenon does not exist for pure admittance loads.

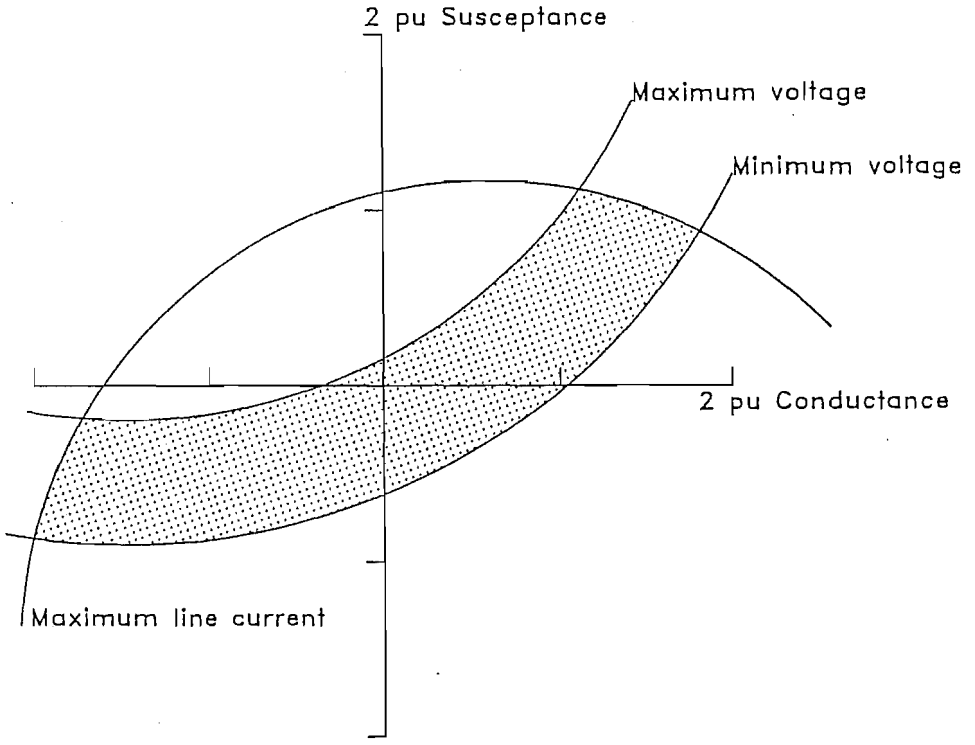

Figure 2.12 Capability Chart of Transmission line on the Complex Admittance Plane

If the complex power S is replaced by a complex load admittance G then G is given by

$$G = I_3/V - F \qquad (2.3.3.1)$$

This equation is used in place of the complex power equation (2.3.1.1) to formulate the equations describing the constraint loci on the complex admittance plane.

Voltage Limits

The loci corresponding to the maximum and minimum load voltage are obtained by combining (2.3.1.2), (2.3.1.4) and (2.3.3.1) to yield

$$G = E/(V.Z) - (1/Z + F + Y) \qquad (2.3.3.2)$$

If the magnitude of V is held constant at the maximum or minimum value and the phase angle of V is varied through 360 degrees then (2.3.3.2) describes a circle on the complex admittance plane. The radius of the circle is $|E/(VZ)|$ and the centre is at $-(1/Z+F+Y)$.

Two arcs from the voltage circles are drawn on the admittance chart in figure 2.12 . The voltage circles are concentric and their common centre represents the shunt admittance that would produce a resonance between the series impedance Z and the shunt admittances Y, F, and G at the load busbar.

Line Current Limit

The locus of maximum current entering the line from the supply busbar is obtained by using (2.3.1.2) to (2.3.1.4) to rewrite (2.3.3.1) in terms of I_1.

$$G = \frac{I_1 - E.Y}{E + E.Y.Z - I_1.Z} - Y - F \qquad (2.3.3.3)$$

If the magnitude of I_1 is held at its maximum value and the phase angle of I_1 is rotated through 360 degrees then (2.3.3.3) describes an ellipse on the admittance plane.

The locus of maximum current leaving the line at the load busbar is also elliptical and is found by rewriting (2.3.3.1) in terms of I_3 to give

$$G = \frac{I_3.(1 + Y.Z)}{E - I_3.Z} - F \qquad (2.3.3.4)$$

The two elliptical loci of maximum current flowing through the ends of the line are indistinguishable on the admittance capability chart. As with the power capability chart the loci gradually become separated if the line shunt admittances of Y are greatly increased in value.

2.3.4 Summary of Transmission Line Capability Charts

Two capability charts have been constructed to describe the performance of a transmission line. One chart is drawn on the complex power plane and the other is drawn on the complex admittance plane.

The operating limits represented on the complex power chart are the minimum and maximum voltage at the load busbar, the voltage stability boundary, and the maximum current flowing at either end of the line.

These limits are also represented on the complex admittance chart apart from the voltage stability boundary which is not applicable.

Power system operators tend to regard loads from the complex power viewpoint rather than the complex admittance viewpoint. This tendency reduces the importance of the admittance capability chart. The predominance of the complex power viewpoint has also influenced the rest of the work in this thesis to concentrate on the complex power capability charts.

2.4 CONCLUSION

This chapter has described the capability charts for two simple power systems. First the chart for a salient pole generator is constructed by using the method described by Walker (1953). The round rotor generator is regarded as a special case of the salient pole machines.

The chapter then describes the capability chart for a transmission line. The traditional voltage circle diagrams are used to construct the loci that represent maximum and minimum voltage limits. The equations of other loci are then derived to represent the maximum line current and voltage stability limits.

A capability chart for the transmission line is also constructed on the complex admittance plane which is more appropriate for admittance loads. The admittance chart is not considered in the rest of this thesis because of the prevalent tendency to regard loads in complex power terms.

The equations of the loci for these simple systems are derived by algebraic and geometrical manipulation of the basic operating equations and vector diagrams. This technique is restricted to small systems because the algebraic manipulation rapidly becomes too unwieldy as the complexity of the system grows.

Chapter 3
A Chart for an HVDC Link

3.1 INTRODUCTION

The development of a capability chart to describe the steady state performance of an HVDC link is particularly attractive because of the increasing use of HVDC links in power systems. Kimbark (1971) developed charts to describe the operation of individual static converters, but a capability chart for a complete HVDC link has not been considered before. The work described in this chapter has been accepted for publication by the IEE (de Silva, Arnold, and Arrillaga, 1987).

The HVDC link capability chart is constructed by using a similar technique to that used for simple systems, such as the synchronous generator and transmission line described in chapter 2. The basic operating equations that describe the behaviour of the HVDC link are manipulated into a suitable form for drawing loci on the complex power plane.

A simplified model of the New Zealand Benmore-Haywards HVDC link has been chosen to demonstrate the construction of the capability chart. The technique used is also applicable to any other two terminal HVDC link.

3.2 CIRCUIT MODEL OF THE HVDC LINK

The New Zealand HVDC link can transfer 600 MW between the North and South Islands of New Zealand. The southern terminal of the link is at Benmore power station and the northern terminal is at Haywards. 600 km of overhead transmission line and 40 km of undersea cable connect the two terminals.

A circuit diagram of the HVDC link is shown in figure 3.1 . The locus equations described in chapter 2 for single generators and transmission lines were not simple to derive. This indicates that considerable mathematical difficulties can be expected in the derivation of locus

equations for the actual HVDC scheme which includes several transformers, generators, and AC/DC converters. Therefore the simplified circuit model shown in figure 3.2 has been chosen instead for the development of the capability chart.

At the Benmore converter terminal the six 90 MW hydro-electric generators are modelled by a single equivalent 540 MW generator feeding a single 16 kV busbar. The voltage level of the busbar is regulated by the generator AVR. The equivalent generator can also operate as a synchronous compensator to deliver up to 324 MVAR or consume a maximum of 378 MVAR.

The two three-winding transformers that interconnect the 16 kV busbars and the South Island 220 kV system are modelled by a single, two winding, 400 MVA interconnecting transformer, having a 3.3 % reactance. This reactance is derived from a power base of 100 MVA that has been chosen for the entire AC/DC system.

The two banks of harmonic filters that are attached to the tertiary windings of the three-winding transformers are modelled as a single bank of filters attached to the 16 kV busbar. The filters absorb the harmonic currents from the converter and also supply 100 MVAR of reactive power. The behaviour of these filters is considered to be ideal so that the voltage waveform on the 16 kV busbar is assumed to be sinusoidal. This assumption is adequate for a steady state, fundamental frequency analysis of the HVDC link.

The converter terminal at Benmore consists of two 250 kV DC poles. Each pole consists of two six pulse bridges in series. The mercury arc valves in the bridges are rated to carry a continuous DC current of 1.2 kA . A 30 degree phase difference between the converter transformers allows an overall twelve pulse operation for each pole.

The four bridges operate under identical control so the bridges and converter transformers can be modelled by a single equivalent twelve pulse bridge and transformer (Arrillaga et al., 1983). The equivalent bridge is rated to carry 1.2 kA DC current. The equivalent lossless converter transformer is rated at 750 MVA and has a reactance of 2% . Since it has been assumed that the converter transformer is fed from a sinusoidal voltage source, the transformer reactance can also be regarded as the commutation reactance of the converter.

An overhead transmission line and an undersea cable transmit the power from the Benmore converter to the Haywards converter. The large smoothing reactors at each end of the line are assumed to maintain a constant DC current. The total resistance of the converters, smoothing reactors, transmission line, and cable is 25.56 Ω.

The Haywards converter terminal also consists of four six pulse bridges in series. The three winding converter transformers connect the bridges to a 110 kV busbar as well as to four synchronous compensators. This arrangement is modelled by a single equivalent bridge, and a two winding converter transformer. The equivalent bridge and transformer have the same parameters as the equivalent Benmore converter.

In the model, the synchronous compensators are connected directly to the 110 kV busbar instead of a tertiary transformer winding. This particular simplification introduces the greatest error in the modelling of the Benmore-Haywards scheme, but also results in a closer correspondence to other HVDC schemes that use two winding converter transformers (Vancouver Island, Pacific Intertie, Skagerrak, Square Butte, CU, Nelson River Bipole II, Inga-Shaba, and Gotland II).

The voltage level of the 110 kV busbar is maintained by the AVR on the equivalent synchronous compensator which can provide up to 260 MVAR of reactive power. This is supplemented by 110 MVAR from the harmonic filters which are assumed to maintain a sinusoidal voltage on the busbar. The 110 kV busbar feeds the North Island AC network.

Similarly to the capability chart of a synchronous generator, which represents the complex power available from the generator terminals, the most useful information to be derived from the HVDC link capability chart is the complex power available to the Haywards 110 kV busbar from the equivalent converter transformer.

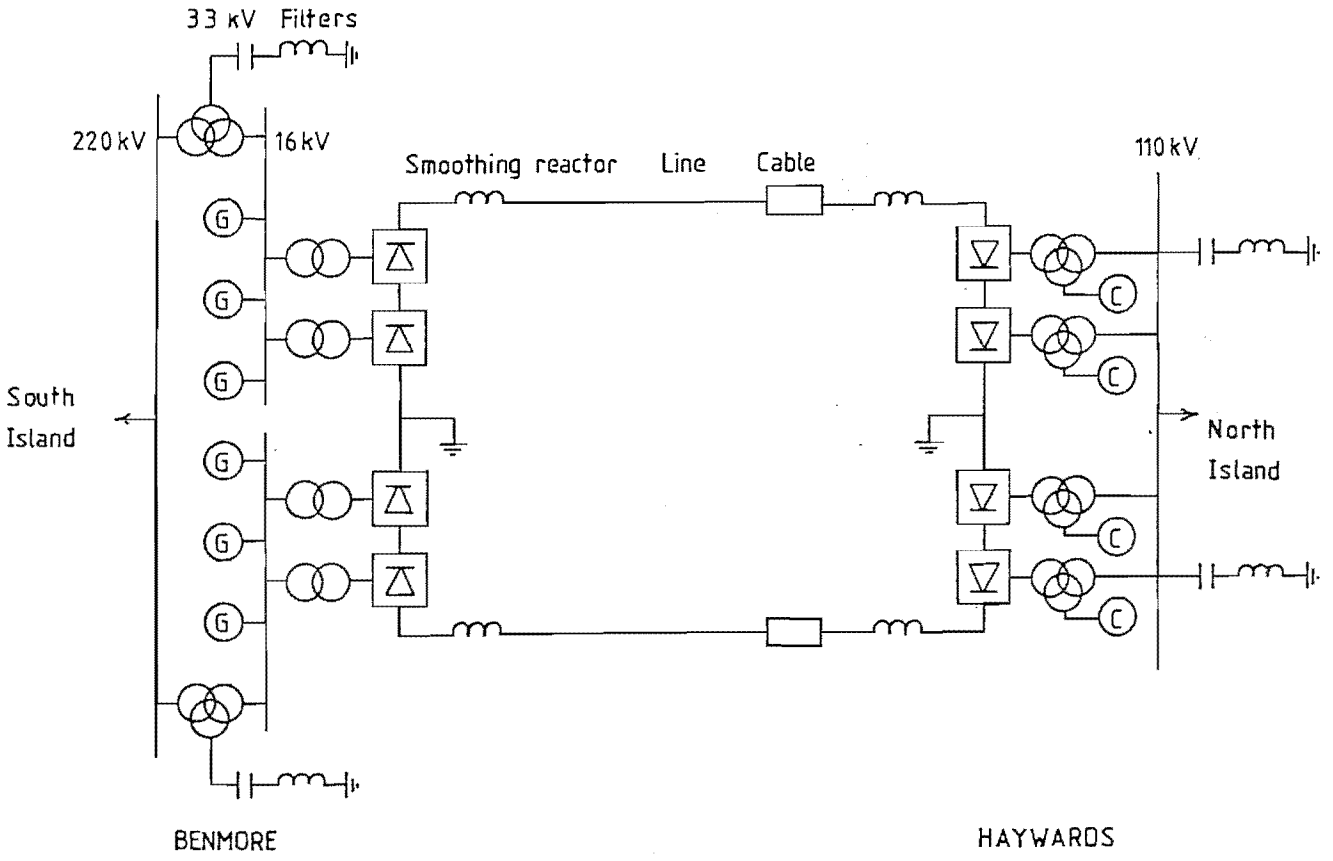

Figure 3.1 New Zealand HVDC Scheme

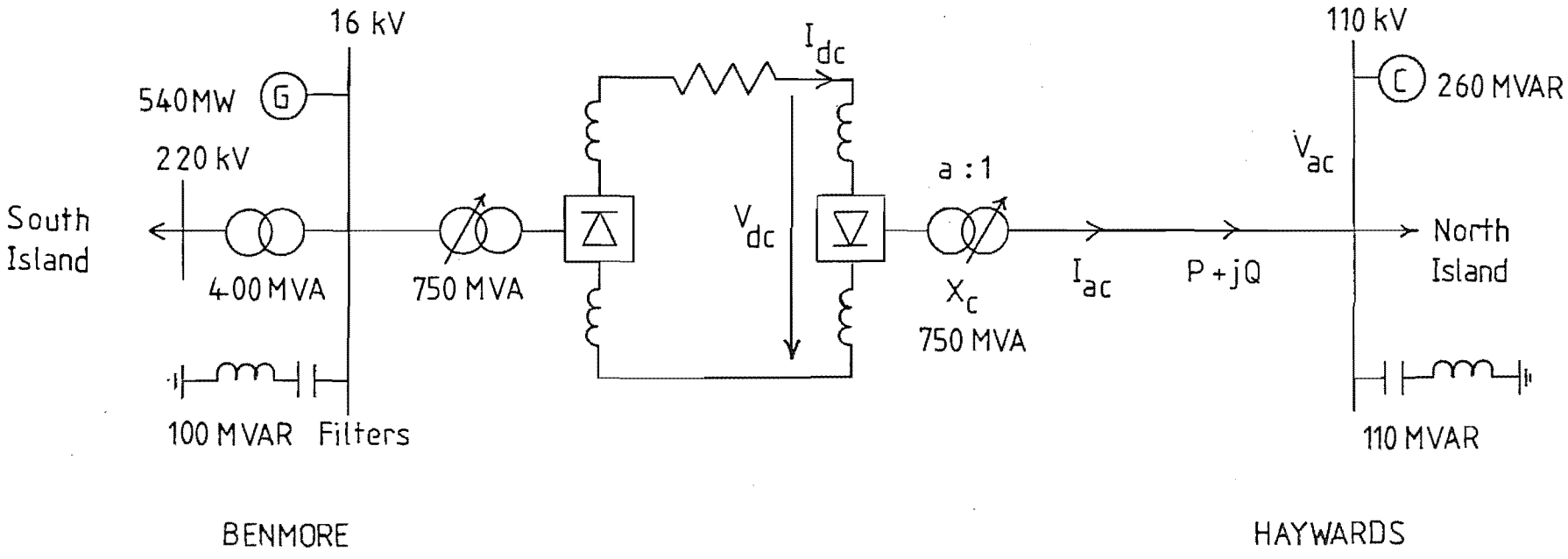

Figure 3.2 Simplified Model Of New Zealand HVDC Scheme

The capability chart of the HVDC link portrays the real and reactive power (P+jQ) that can be supplied from the Haywards converter transformer to the Haywards 110 kV busbar.

3.3 OPERATING CONSTRAINTS OF THE HVDC LINK

Each operating constraint of the HVDC link must be represented as a locus on the capability chart.

Converter Transformer Current

The heat dissipation capability of each 750 MVA converter transformer determines the maximum RMS current that may flow through the transformer windings. This current consists of a fundamental frequency component as well as several harmonic frequency components. All of these components must be considered even though only the fundamental current contributes to the useful power available.

Converter Valve Current

The DC line current flows through the converter valves, smoothing reactors, transmission line, and cable. Of these four components, the converter valves possess the smallest current rating of 1.2 kA, and they therefore determine the maximum DC current that may flow in the link.

The converter valves also require a minimum holding current of 0.1 kA. This is the DC current necessary to sustain valve conduction whilst each valve is nominally on.

Harmonic Filter Current

The DC line current is also related to the harmonic currents flowing in the filter banks. If commutation effects are neglected then the harmonic current levels can be assumed to be directly proportional to the DC current. This is a safe assumption because the inclusion of commutating effects tends to reduce the calculated harmonic current levels (Arrillaga, 1983).

The filters are designed to cope with the harmonic currents associated with the maximum expected DC current, as well as the fundamental frequency reactive current. Therefore operation within the

maximum converter valve current locus will also ensure a safe level of harmonic filter current.

DC Voltage Rating

The DC voltage of the transmission line and cable has a reasonably smooth waveform during steady state operation. The maximum continuous DC voltage that may be borne is 525 kV. This is determined by the continuous voltage ratings of the transmission line insulators, surge arrestors, and cable insulation. Each of these components will also tolerate a much higher transient overvoltage, but this is not represented on the steady state capability chart.

Converter Control Angles

A minimum limit is set on both converter control angles. During rectification, the firing angle α must be at least 3 degrees to ensure that the valve turn-on voltage is sufficient to reliably establish valve conduction.

During inversion, the extinction angle δ must be at least 18 degrees to allow the valve to recover from forward conduction in time to block the reverse voltage which will be impressed at the next voltage crossover.

Converter Commutation Angle

The reactance of the converter transformers causes a commutation overlap to occur as one valve takes over conduction from another valve. When the overlap angle increases above 60 degrees, periodic phase to phase short circuits occur through the valves.

Although the converter may continue to operate with commutation angles greater than 60 degrees, the simple equations used to model the converter are only valid for angles up to 60 degrees. The requirement that the commutation angle be less than 60 degrees is therefore due to the mathematical model used rather than a real converter constraint. However, as the commutation angle rarely exceeds 30 degrees during

practical steady state operation, the simple mathematical model is perfectly adequate.

Capability of the Benmore Generator

The performance restrictions of the Benmore generator can be represented on a capability chart as described in chapter 2. To simplify the analysis, the generator chart is approximated by a rectangle on the complex power plane as shown in figure 3.3 . The minimum and maximum real power limits on the rectangle correspond to the minimum and maximum turbine power limits. The maximum reactive power limit corresponds to the maximum rotor current and the minimum reactive power limit corresponds to the synchronous stability limit.

If the Benmore lake level is low then the generator is used as a synchronous compensator. In this case the performance of the generator is restricted to zero real power output and a reactive power variation of -378 MVAR to +324 MVAR.

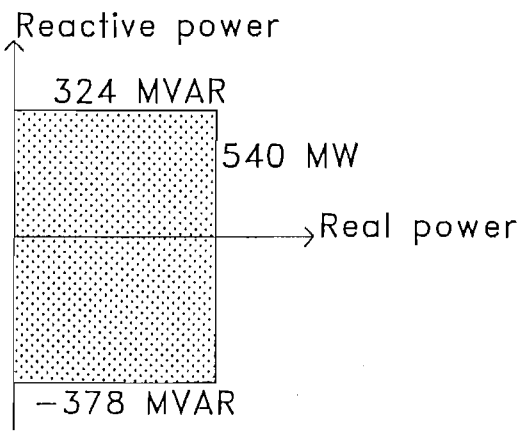

Figure 3.3 Rectangular Approximation to Capability Chart of Benmore Generator

Interconnecting Transformer Current

The power that can be supplied from the South Island network is restricted by the rating of the 400 MVA Benmore interconnecting transformer. This restriction is especially important when the Benmore generators are acting as synchronous compensators and are not contributing any real power to the HVDC link.

3.4 LOCI OF OPERATING CONSTRAINTS

The equations that describe the locus of each operating constraint are formulated from the basic steady state operating equations of the HVDC link. The operating equations can be conveniently written in terms of the combined AC/DC per unit system described by Arrillaga et al. (1983).

3.4.1 AC/DC Per Unit System

In this system the conventional per unit quantities are used for the AC networks. The DC per unit quantities are defined by choosing the same base power and base voltage for both the AC and DC sides of each converter bridge.

The power base S_b for the entire circuit model is 100 MVA . The DC voltage base V_{bdc} is the same as the converter transformer secondary voltage rating of 420 kV.

The DC current base I_{bdc} must be $\sqrt{3}$ times the AC current base in order to maintain consistent quantities of per unit power throughout the entire network.

$$I_{bdc} = S_b/V_{bdc} = \sqrt{3}.I_{bac} = 0.238 \text{ kA} \qquad (3.4.1.1)$$

Consequently the DC valve current rating of 1.2 kA is represented as 5.04 pu current.

The DC resistance base R_{bdc} is the same as the AC impedance base Z_{bac}.

$$R_{bdc} = Z_{bac} = V_{bdc}^2/S_b = 1.764 \text{ k}\Omega \quad (3.4.1.2)$$

Hence the total 25.56 Ω series resistance of the DC circuit is represented as 0.014 pu resistance.

3.4.2 Basic AC/DC Converter Operating Equations

According to Arrillaga et al. (1983), the steady state operation of the Haywards converter can be described by the following equations.

$$P = -V_{dc}.I_{dc} \quad (3.4.2.1)$$

$$P^2+Q^2 = V_{ac}^2.I_{ac}^2 \quad (3.4.2.2)$$

$$I_{ac} = a.K_1.K_3.I_{dc} \quad (3.4.2.3)$$

$$V_{dc} = K_1.a.V_{ac}.\cos(\alpha) - K_2.X_c.I_{dc} \quad (3.4.2.4)$$

$$I_{dc} = [a.V_{ac}/(\sqrt{2}.X_c)].[\cos(\alpha) - \cos(\alpha+\mu)] \quad (3.4.2.5)$$

where the converter variables are signified by

V_{dc} DC voltage
I_{dc} DC current
a Transformer tap ratio
X_c Transformer reactance (=commutation reactance)
I_{ac} AC current
P Real power output from converter transformer
Q Reactive power output from converter transformer
V_{ac} AC voltage

The constants K_1, K_2, and K_3 are given by

$K_1 = 3.\sqrt{2}/\pi$

$K_2 = 3/\pi$

$K_3 = 0.995$ for twelve pulse converter operation with a commutation angle μ well below 60 degrees.

3.4.3 Loci of Haywards Converter

The operating constraint loci of the Haywards converter are examined first. All of the Haywards loci are shown on the chart in figure 3.4 . The scale of the chart must accommodate the large locus that represents the maximum commutation angle hence the other smaller loci appear cramped. Figure 3.5 portrays the smaller loci on a larger scale for clarity.

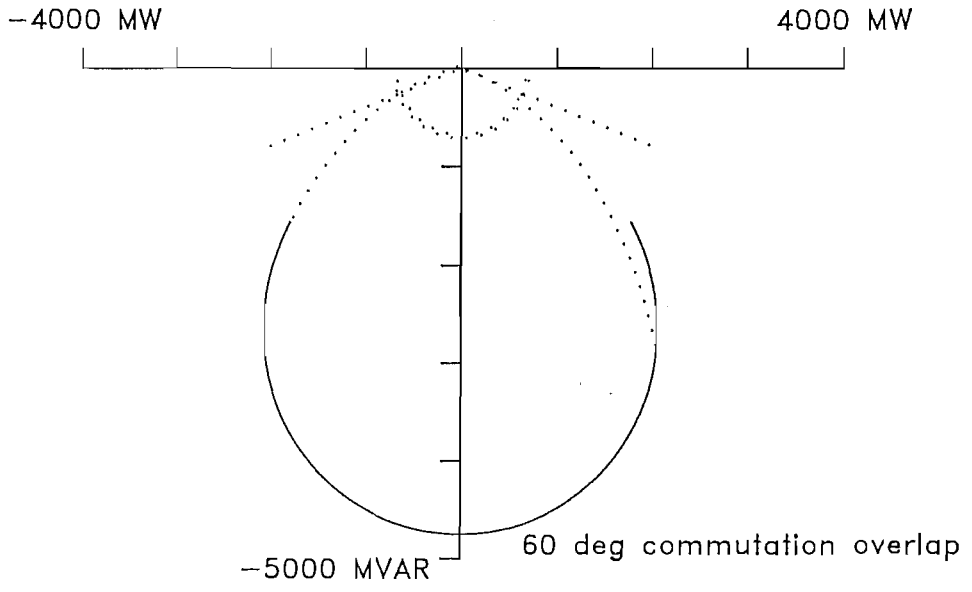

Figure 3.4 Loci of Haywards Converter

The locus representing the maximum commutation angle dominates this chart. The other constraint loci drawn with dashed lines restrict the converter operation such that the maximum commutation angle is not approached.

Commutation Overlap Locus

The locus representing the maximum commutation angle is drawn by using a parametric approach. The commutation angle μ is held constant at its maximum value of 60 degrees and the firing angle α is chosen to be the variable parameter. Under these conditions the mathematical model's valid range of α is from 0 degrees to 120 degrees (at which point the extinction angle δ is 0 degrees). α is gradually increased through its full valid range and (3.4.2.5) is used to calculate a value of I_{dc} for each value of α.

(3.4.2.4) is then used to find the corresponding values of V_{dc} and (3.4.2.1) provides the real power coordinate on the chart for each value of α. The reactive power coordinate is obtained by substituting (3.4.2.3) into (3.4.2.2) to give

$$Q = -\sqrt{[(a.V_{ac}.K_1.K_3.I_{dc})^2 - P^2]} \qquad (3.4.3.1)$$

The other loci shown in figure 3.4 restrict the converter operation such that the overlap angle is always much less than 60 degrees. This justifies the mathematical model used and also allows the commutation overlap locus to be ignored in the rest of this analysis.

Loci of DC Current Limits

The loci representing the maximum DC valve current and minimum DC valve holding current are obtained by substituting (3.4.2.3) into (3.4.2.2) to give

$$P^2+Q^2 = (a.V_{ac}.K_1.K_3.I_{dc})^2 \qquad (3.4.3.2)$$

which is the equation of a circle centred on the origin with a radius of $a.V_{ac}.K_1.K_3.I_{dc}$.

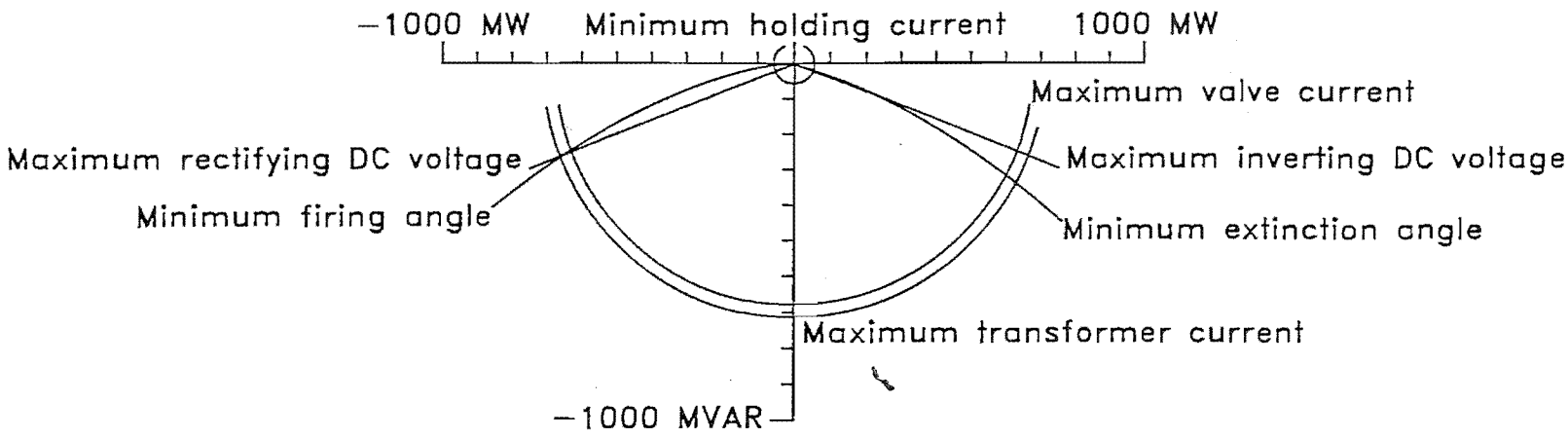

Figure 3.5 Loci of Haywards Converter on Large Scale

The locus representing the maximum commutation angle has been omitted.

Locus of Maximum Converter Transformer Current

The maximum RMS converter transformer current I_t is equal to the per unit MVA rating of the transformer. If the effects of commutation are ignored then the converter transformer current can be related to the DC current in per unit by (Arrillaga, 1983)

$$I_t = \sqrt{2}.I_{dc} \qquad (3.4.3.3)$$

The DC current from (3.4.3.3) can then be substituted into (3.4.3.2) to produce a circular locus describing maximum converter transformer current. The radius of the circle is slightly larger than the circle that represents the maximum valve current.

If the effects of commutation are considered, then the RMS converter transformer current would correspond to a slightly larger DC current, and the locus would be an approximate circle with a slightly larger radius. Consequently there is a small margin of safety inherent in the circular locus described here.

Loci of Maximum DC Voltage

The maximum DC voltage is represented by two loci, one corresponds to the rectifying state and the other to the inverting state. Combining (3.4.2.1), (3.4.2.2), and (3.4.2.3) gives

$$Q = -|P|.\sqrt{[(a.V_{ac}.K_1.K_3/V_{dc})^2 - 1]} \qquad (3.4.3.4)$$

If V_{dc} is held at its maximum value then this describes two straight lines extending from the origin. The gradients of the lines are $\pm\sqrt{[(a.V_{ac}.K_1.K_3/V_{dc})^2 - 1]}$.

As the maximum allowable DC voltage increases, the two straight lines approach the horizontal. The maximum DC voltage that can possibly be attained by the link in steady state operation is $a.V_{ac}.K_1.K_3$ which corresponds to horizontal loci. If the maximum allowable DC voltage exceeds this value then the maximum voltage loci will not appear on the chart.

Locus of Minimum Firing Angle

A parametric approach is used to draw the locus that represents the minimum firing angle α_{min} . The variable parameter that has been chosen is the DC current I_{dc} which is gradually increased from zero to slightly beyond its maximum value. For each value of I_{dc} the real power coordinate of the locus is obtained by substituting (3.2.4.4) into (3.2.4.1) to give

$$P = -[K_1.a.V_{ac}.\cos(\alpha_{min}).I_{dc} - K_2.X_c.I_{dc}^2] \qquad (3.4.3.5)$$

The reactive power coordinate is obtained from (3.4.3.1) . These two equations describe a cycloid. As α_{min} decreases the cycloid twists toward the horizontal.

Locus of Minimum Extinction Angle

The locus representing the minimum extinction angle δ_{min} is obtained by changing the sign of the powerflow in (3.4.3.5) and replacing α_{min} with δ_{min} to give a real power coordinate of

$$P = K_1.a.V_{ac}.\cos(\delta_{min}).I_{dc} - K_2.X_c.I_{dc}^2 \qquad (3.4.3.6)$$

The reactive power coordinate is again provided by (3.4.3.1) hence this locus is also a cycloid. Similarly to the minimum firing angle locus, the minimum extinction angle locus twists towards the horizontal as δ_{min} decreases.

3.4.4 Loci of Benmore Converter

The constraint loci of the Benmore converter must be combined with the Haywards converter loci to complete the capability chart of the HVDC link.

DC Link Power Transfer Mapping

The operating constraints of the Benmore circuit can be easily referred to the Haywards end of the link by using a DC link power transfer mapping. This is a point to point mapping that relates the complex power entering the link from the Benmore 16 kV busbar (P_i+jQ_i) to the complex power leaving the link at the Haywards 110 kV busbar (P_r+jQ_r) . The subscript r refers to the nominal rectifier at Benmore , and the subscript i refers to the nominal inverter at Haywards.

The mapping is obtained by considering the real power loss in the DC line resistance (R)

$$P_i = P_r - I_{dc}^2.R \qquad (3.4.4.1)$$

Combining (3.4.2.2), (3.4.2.3), and (3.4.4.1) provides the point to point mapping

$$P_i = P_r - \frac{(P_r^2+Q_r^2).R}{(K_1.K_3.a_r.V_{acr})^2} \qquad (3.4.4.2)$$

$$Q_i = -\sqrt{[(a_i/a_r)^2.(V_{aci}/V_{acr})^2.(P_r^2+Q_r^2) - P_i^2]} \qquad (3.4.4.3)$$

The constraint locus equations of the Benmore converter can now be first formulated in the same manner as those of the Haywards converter. This produces a set of Benmore converter loci which refer to the power entering the link at the Benmore 16 kV busbar. These loci are identical to the Haywards converter loci shown in figures 3.4 and 3.5 . The DC link power transfer mapping is then used to transform these loci, point by point, to produce a new set of Benmore converter constraint loci which are referred to the Haywards 110 kV busbar.

The transformed Benmore converter loci are shown in figure 3.6 . All of the constraints involving current flow are still represented by arcs of circles. However the shapes of all other loci have been altered by the transformation.

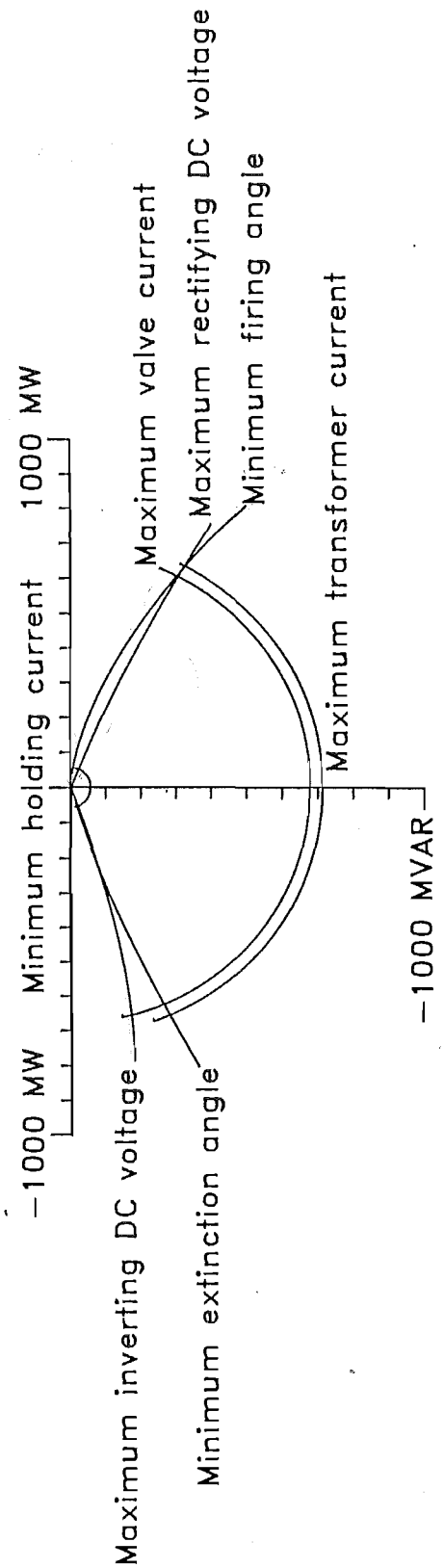

Figure 3.6 Loci of Benmore Converter

These Benmore converter loci are referred to the Haywards 110 kV busbar. This allows these loci to be directly superimposed onto the Haywards loci shown in figure 3.5 .

3.4.5 Loci of South Island Power Generation

The South Island AC system behind the Benmore converter also places its own restrictions on the power available to the Haywards 110 kV busbar.

The complex power supplied from the South Island 220 kV busbar to the Benmore 16 kV busbar is dependent on the voltage angle between the busbars. This can be analyzed by using the approach described in chapter 2 for drawing voltage loci for transmission lines. In this case the transmission line is replaced by a 3.3% reactance that represents the 400 MVA interconnecting transformer.

If the voltages at the South Island 220 kV busbar and the Benmore 16 kV busbar are both held at 1 pu then the power delivered to the Benmore 16 kV busbar is represented by a circular locus. An arc of this circle is shown in figure 3.7 . The power is also restricted by the maximum current rating of the 400 MVA interconnect transformer. This is represented by the area within another circular locus. The full range of power delivery is therefore represented by the portion of the arc that lies within the maximum current circle.

If the Benmore generator is run as a synchronous compensator then the generator reactive power variation of -378 MVAR to 324 MVAR will augment the power delivered from the South Island busbar. Taking into account the 100 MVAR contribution of the harmonic filters, the range of reactive power variation becomes -278 MVAR to 424 MVAR.

This reactive power variation is added to each point on the power delivery arc on figure 3.7 to produce the chart shown in figure 3.8 . The shaded region in this chart represents the power that may be delivered to the Benmore converter from the Benmore 16 kV busbar.

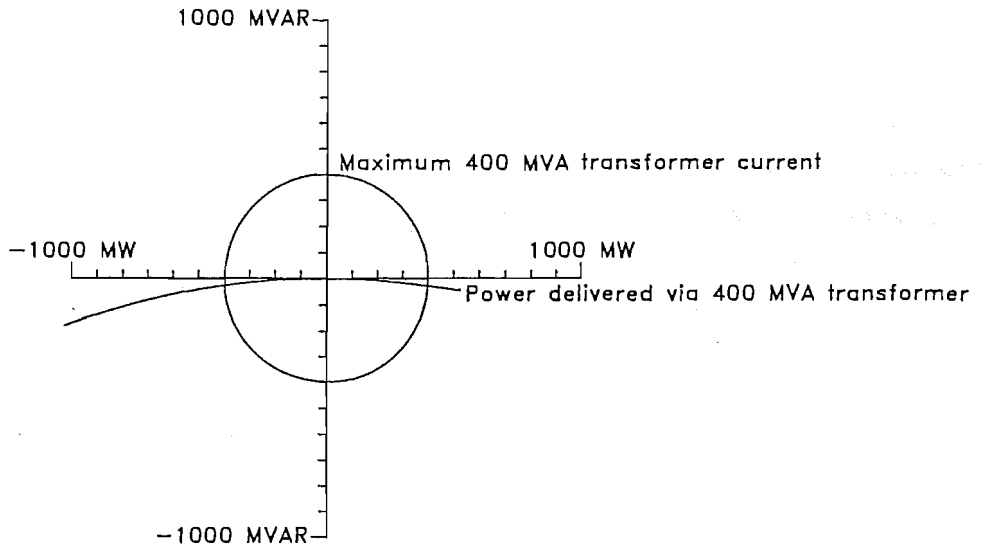

Figure 3.7 Power Delivered to Benmore from South Island

The arc within the maximum current circle represents the power available to the Benmore 16 kV busbar from the South Island 220 kV busbar via the 400 MVA transformer.

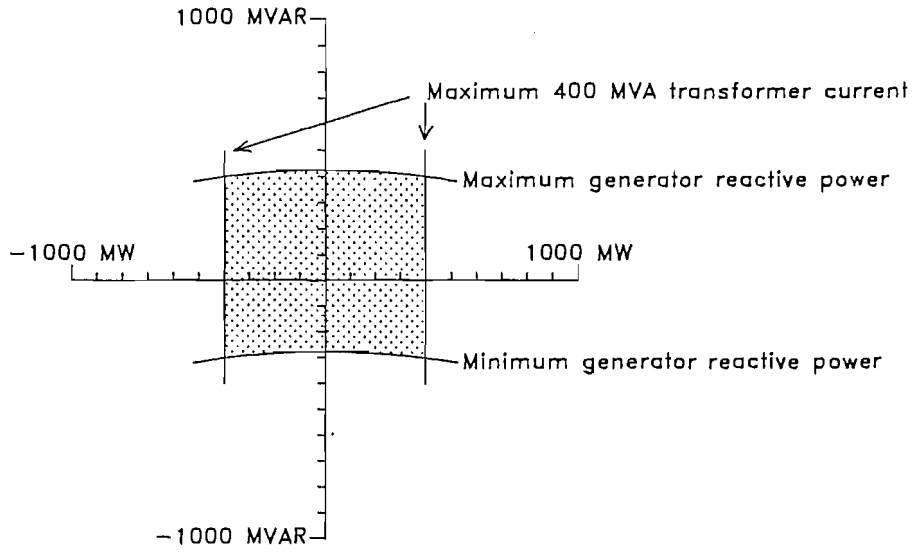

Figure 3.8 Power to HVDC Link from Benmore 16 kV Busbar

This can be regarded as a capability chart of the South Island when the Benmore generator is used as a synchronous compensator.

3.4.6 Complete Capability Chart

The complete capability chart of the HVDC link is constructed by combining all of the constraint loci. The wedge shaped capability chart shown in figure 3.9 is formed by superimposing the Benmore converter loci from figure 3.6 onto the Haywards converter loci on figure 3.5 . Only the critical operating constraints that border the operating region are shown, the other constraints have been omitted for clarity.

This chart describes the real and reactive power that may be delivered to the North Island from the link, assuming that an infinitely strong 16 kV busbar exists at Benmore. The operating point can be moved around the operating region by adjusting the converter control angles. Under normal operating conditions, with real power being delivered from Benmore to Haywards, the operating point is located at the corner of the wedge by the intersection of the maximum valve current locus and the minimum Haywards extinction angle locus.

The reactive power coordinate of this operating point (-316 MVAR) matches the reactive power consumption of the actual Haywards converter. The real power coordinate of the operating point (598 MW) differs slightly from the 580 MW supplied from the actual converter. This 3% error is attributed to the simplifications made during the analysis.

The shaded operating region shows the theoretical ability of the HVDC link to supply a wide range of complex power to the AC system. The present operating modes of constant current or constant power control do not fully utilize the entire operating region. More sophisticated control strategies, such as power modulation, are needed to make better use of the range of complex power available.

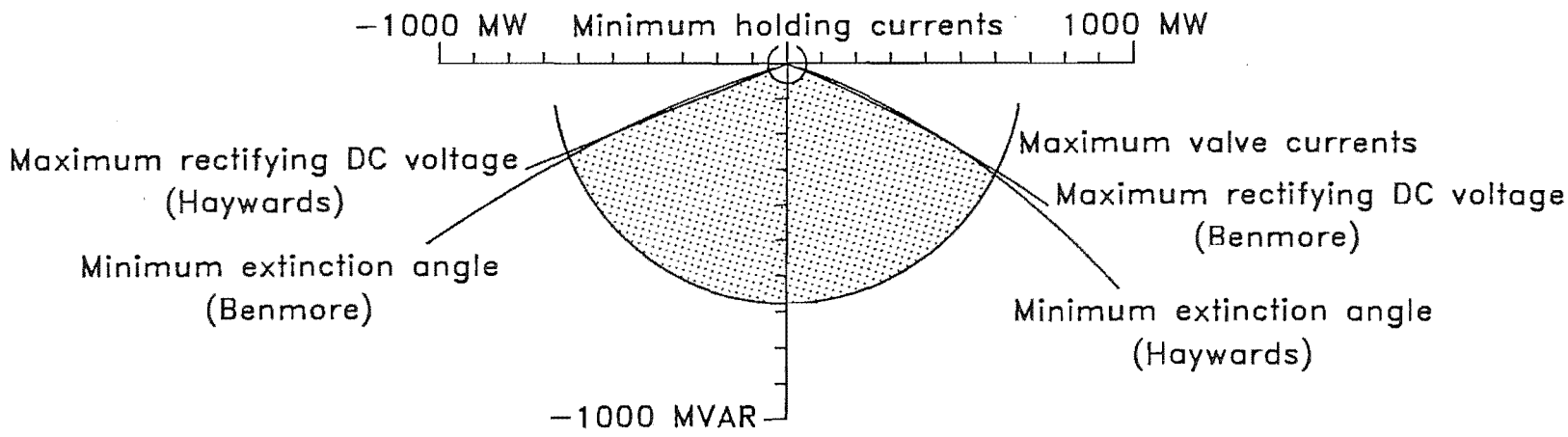

Figure 3.9 Capability Chart of HVDC Link

The shaded area represents the real and reactive power that may be supplied from the Haywards converter transformer to the Haywards 110 kV busbar.

If the Benmore generators are run as synchronous compensators, and the power generation capability of the South Island is considered, then the chart shown in figure 3.8 must be incorporated into the complete capability chart. This is achieved by applying the DC link power transfer mapping to the loci of figure 3.8, and superimposing the transformed loci onto the chart in figure 3.9 . The region of negative reactive power in figure 3.8 cannot be transformed because the converters must always consume reactive power.

The resultant capability chart is shown in figure 3.10 .The shaded region of this chart shows that the maximum real power transfer is restricted by the maximum current rating of the 400 MVA Benmore interconnecting transformer.

3.5 CONCLUSION

This chapter has described the construction of a capability chart to portray the performance of an HVDC link. A simplified model of the New Zealand Benmore-Haywards HVDC scheme has been chosen to demonstrate the construction technique.

The approach used to construct the chart involves the explicit derivation of the equations that describe the constraint loci. This approach is similar to that used in chapter 2 for the construction of charts for a generator and a transmission line.

Unlike the generator and transmission line loci, the HVDC link loci cannot be easily drawn by hand and the assistance of computer plotting equipment is essential.

The wedge shaped capability chart shows the wide range of complex power that is theoretically available from HVDC links.

While the approach of explicit equation derivations was again successful, it has also emphasised the enormous amount of effort that is associated with the derivation of equations for a moderately complicated power system.

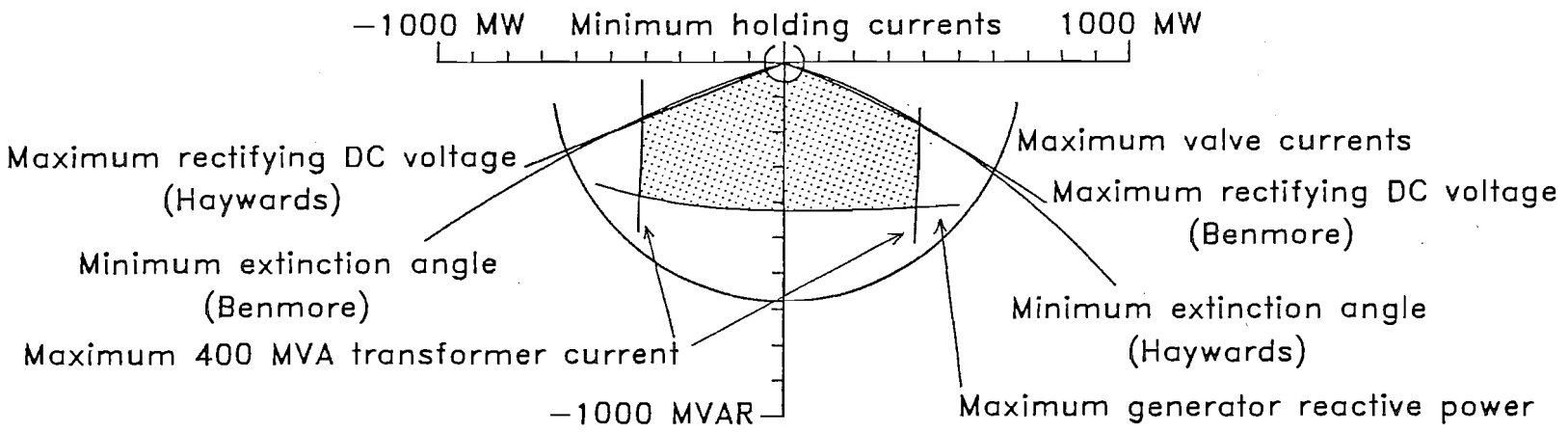

Figure 3.10 Capability Chart of Combined HVDC Link and South Island System

The operating constraints of the South Island system prevent the full utilization of the wedge shaped operating region of the HVDC link.

Chapter 4
Charts for Large AC Systems

4.1 INTRODUCTION

The concept of a capability chart can be extended to describe the performance of any large general power system, in addition to the small systems previously described in chapters 2 and 3. In the context of a large system, the capability chart portrays the real and reactive power available to a load from any particular busbar in the system.

The two dimensional capability chart associated with a particular busbar can be regarded as being a single slice of an overall 2n dimensional capability chart for the n busbars that make up the general power system. This overall capability chart describes all of the combinations of complex power simultaneously available from the n busbars.

The critical operating constraints of the system are represented on the overall chart by 2n-1 dimensional hypersurfaces that bound the operating region. Unfortunately we cannot easily visualise regions of such a high dimensional order, and must be content with observing two dimensional slices of the overall chart. Each slice describes the allowable load variation at one busbar whilst the loading at other busbars is kept fixed.

The generator, transmission line, and HVDC link charts that were described in chapters 2 and 3 were all constructed by using the technique of manipulating the system operating equations into a suitable form for drawing loci on the complex power plane. This technique is satisfactory if the power system is small, because only a few simple operating equations need to be considered. The same technique cannot be used for large power systems because the large number of operating equations cannot be so easily manipulated.

The difficulty of forming explicit locus equations can be circumvented by using a contour plotting approach to gradually trace out each locus on the complex power plane. A powerflow algorithm is used to

iteratively solve the operating equations at each point on the contour, without having to resort to an explicit closed form solution.

Contour tracing has been used before by Price (1984) to display families of contours for a power system. Price's work concentrated on voltage contour maps and showed that the contours were often looped and twisted. Only one family was considered at a time and the contours were not combined to portray a capability chart.

This chapter describes a capability charting algorithm for large general power systems that uses a similar contour tracing approach to cope with the expected twists and loops in the contours. This algorithm was the subject of a paper presented at the Second International Conference on Power System Monitoring and Control (Arnold and de Silva, 1986).

4.2 SYSTEM OPERATING CONSTRAINTS

The performance of a large power system is restricted by numerous operating constraints. The categories of operating constraint that are considered by the capability charting algorithm are

1. Minimum/maximum voltage at a load busbar.
2. Minimum/maximum reactive power generation from a generator busbar.
3. Minimum/maximum real power generation from a slack generator busbar.
4. Maximum current in a transmission line or transformer.
5. Maximum voltage phasor angle difference across a transmission line or transformer.
6. Maximum angular deviation of any generator busbar voltage phasor from the swing busbar voltage phasor.

This set of operating constraints is adequate for most AC power systems. In principle, any other constraint that can be numerically evaluated may also be included in the algorithm if necessary.

4.2.1 Voltages and Currents on Transmission Lines

The transmission line capability chart described in chapter 2 assumed that the maximum values of voltage and current along the transmission line occurred at the busbars at the ends of the line. To simplify calculations, the same assumption is used for transmission lines in large systems.

This assumption becomes less valid as the length of transmission lines increases beyond a quarter wavelength (1500 km at 50 Hz). Therefore long lines should be modelled as a concatenated series of short lines with intermediate busbars. The values of voltage and current at the intermediate busbars will then represent the corresponding values of voltage and current part way along the line.

4.2.2 Generator Capability

The generator capability chart described in chapter 2 identifies the operating constraints that restrict the performance of each generator in the power system. In chapter 3, the true generator capability chart was approximated by a rectangular chart to simplify the analysis of the AC/DC system. The capability charting algorithm described in this chapter also uses a rectangular approximation to the true generator chart. The borders of each rectangle are represented by the maximum and minimum real and reactive power constraints on generators.

4.2.3 Steady State Stability

The voltage angle constraints imposed across branches and the voltage angle deviation of generator busbars are an attempt to impose a form of steady state stability on the system. It is acknowledged that such constraints are extremely crude and do not guarantee stability, however the voltage angles have the advantage of being easily defined and evaluated.

The actual choice of values for the constraining angles depends on the power system and must be left to the judgement of the algorithm's user. A large value of 30 degrees has been used for the systems described in this thesis.

A better measure of steady state stability could be obtained from an eigenvalue analysis of the system. This approach is briefly examined as a proposed development in chapter 8.

4.2.4 Total Constraint Number

Considering only the categories listed, the total number of possible operating constraints in a power system is

$$\begin{aligned} \text{Constraint number} = \quad & 4 \times \text{number of slack busbars} \\ + \quad & 3 \times \text{number of generator busbars} \\ + \quad & 2 \times \text{number of load busbars} \\ + \quad & 2 \times \text{number of branches} \end{aligned} \qquad (4.2.4.1)$$

4.3 TEST SYSTEM

The power system chosen for demonstrating the capability charting techniques is the well known IEEE 14 Busbar Test System. A single line diagram of this power system is shown in figure 4.1 . The appendix provides the detailed circuit data for the system. Table 4.1 summarizes the operating constraints that have been adopted for demonstration purposes. The test system is governed by a total of 74 individual operating constraints.

The synchronous compensators are regarded as being generators with zero real power output. Busbar 7 is a virtual busbar in the three winding transformer and does not have meaningful voltage constraints. To prevent the busbar 7 voltage from becoming a critical constraint it is assigned extreme voltage limits.

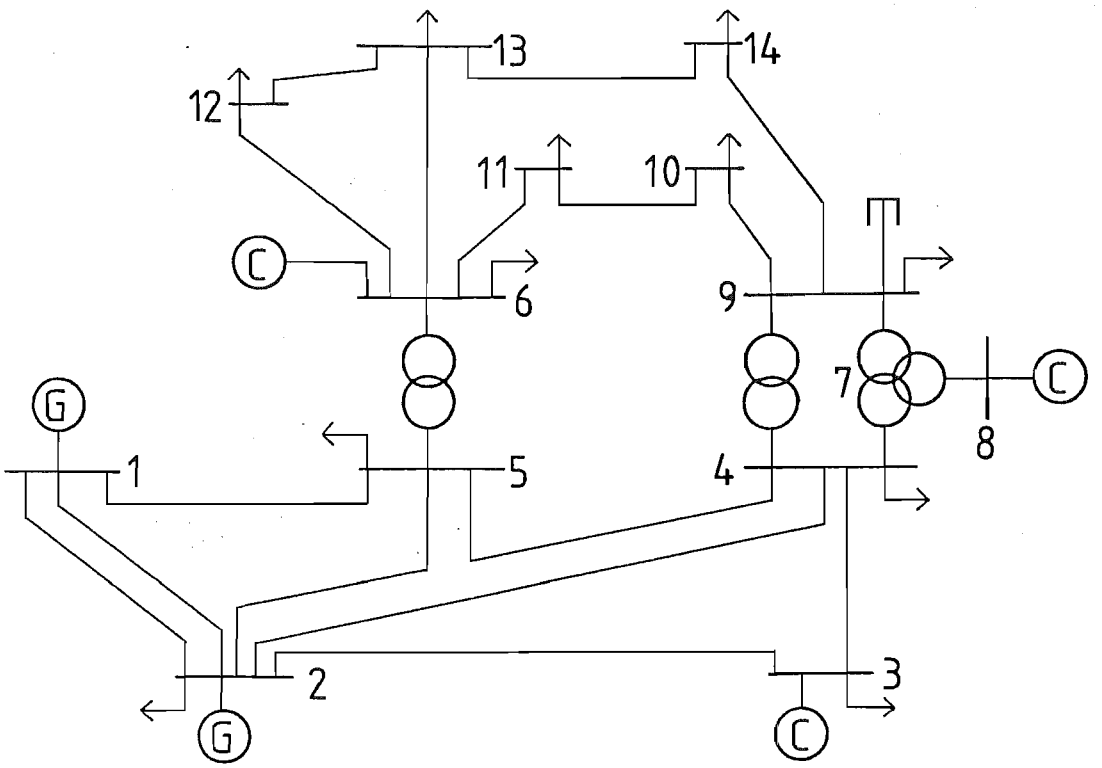

Figure 4.1 IEEE 14 Busbar Test System

TABLE 4.1 OPERATING LIMITS OF IEEE 14 BUSBAR TEST SYSTEM

Minimum voltage at any busbar	0.85 pu
Maximum voltage at any busbar	1.15 pu
Maximum line currents for high voltage transmission system	1.60 pu
Maximum line currents for low voltage distribution system	0.80 pu
Maximum transformer winding currents	1.00 pu
Maximum voltage angle difference across any branch	30.00 deg
Maximum voltage angle deviation of generator busbars from slack busbar 1	30.00 deg
Minimum real power generation from slack busbar 1	0.00 MW
Maximum real power generation from slack busbar 1	300.00 MW

Reactive power generation limits

Busbar	Minimum (MVAR)	Maximum (MVAR)
1	-200.	200.
2	-40.	50.
3	0.	40.
6	-6.	24.
8	-6.	24.

4.4 CAPABILITY CHARTING ALGORITHM

The capability charting algorithm for general power systems uses a contour tracing approach to construct a web of loci on the complex power plane.

The constraint loci can be divided into three classes. The primary constraints are those that form parts of the boundary of the operating region. The secondary constraints are represented by other loci that lie near the boundary of the operating region. The remaining tertiary constraints are relatively unimportant and are represented by loci that lie far from the operating region.

Some consideration was given to tracing only the primary loci around the boundary of the operating region. This approach was eventually rejected for two reasons. Firstly, the sole selection of primary loci would obscure any important secondary loci. Secondly, the model of the power system cannot be expected to perfectly represent the behaviour of the actual system. In this case the true primary constraint may be any one of a group of constraints that verge on the boundary of the operating region. It is therefore important to be aware of the existence of the secondary constraints.

4.4.1 Definition of the Vicinity of the Operating Region

The capability charting algorithm identifies primary and secondary constraints by tracing all constraint loci that lie within the vicinity of the operating region. The vicinity of the operating region can be defined by first considering a violation index for the system.

Each system constraint has an associated excess defined by

$$\text{Excess} = \text{Value of constrained variable} - \text{Limiting constraint value} \qquad (4.4.1.1)$$

The excess is negative when the variable is within the stated limit and positive beyond the limit. For consistency, the negative excess must be considered for minimum voltage and minimum power constraints.

The violation index is equal to the largest constraint excess in the system. This index is negative within the operating region, zero on the boundary of the region, and positive outside the region.

The contour on the capability chart corresponding to a violation index of 0.1 surrounds the operating region. This contour has been chosen to define the perimeter of the vicinity of the operating region. The algorithm traces all constraint loci that lie within this vicinity.

The value of 0.1 has been chosen to be large enough for the vicinity to accommodate areas of interest that lie just outside the operating region yet it is also small enough to avoid unrealistic operating states. By restricting the investigation to the vicinity the algorithm saves the unnecessary computation associated with the unrealistic states.

4.4.2 Structure of the Capability Charting Algorithm

The structure of the capability charting algorithm is shown in figure 4.2 . This algorithm produces a capability chart for busbar 9 as shown in figure 4.3 .

System Data Input

The system data file is first read in and the operating constraints are identified. The number of constraints is reduced by recognizing that a set of identical parallel transmission lines will attain their maximum current and voltage angle limits simultaneously. Hence the constraints of only one transmission line of the set needs to be observed. This reduction in the total number of constraints helps to speed up the algorithm. The number of constraints associated with identical parallel transformers is also reduced in the same way.

In the test system the parallel lines between busbar 1 and busbar 2 are identical, hence the constraints of one of these lines are ignored. The total number of observed constraints is consequently reduced from 74 to 72. In this particular case the reduction in the observed constraints is insignificant. A system with a larger proportion of parallel lines or transformers would produce a more impressive reduction.

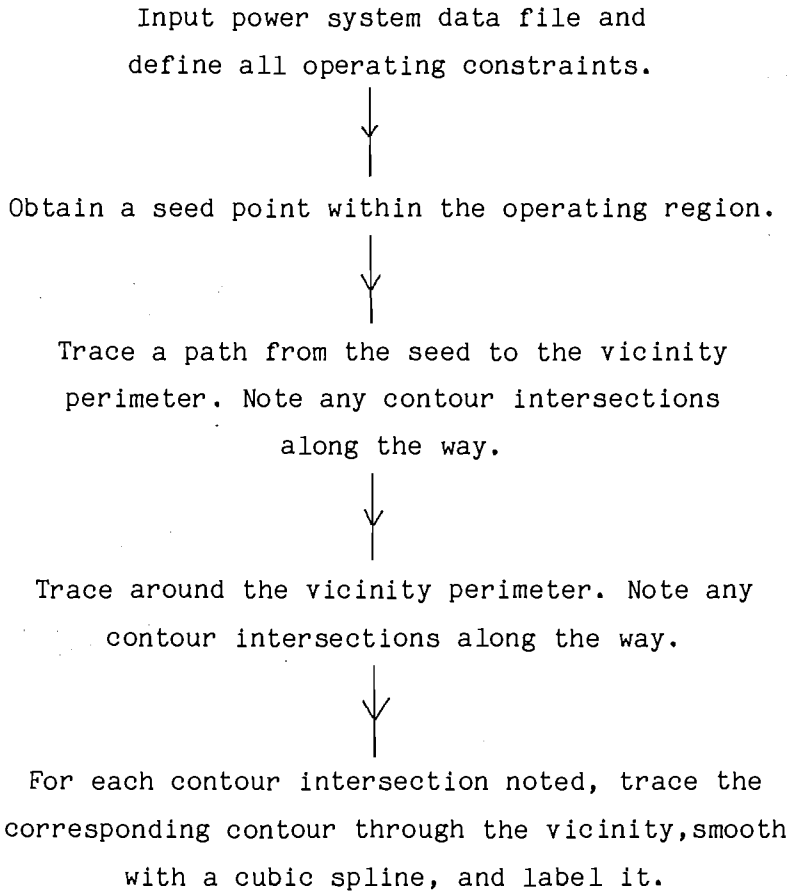

Figure 4.2 Structure of Capability Charting Algorithm Using the Contour Tracing Technique

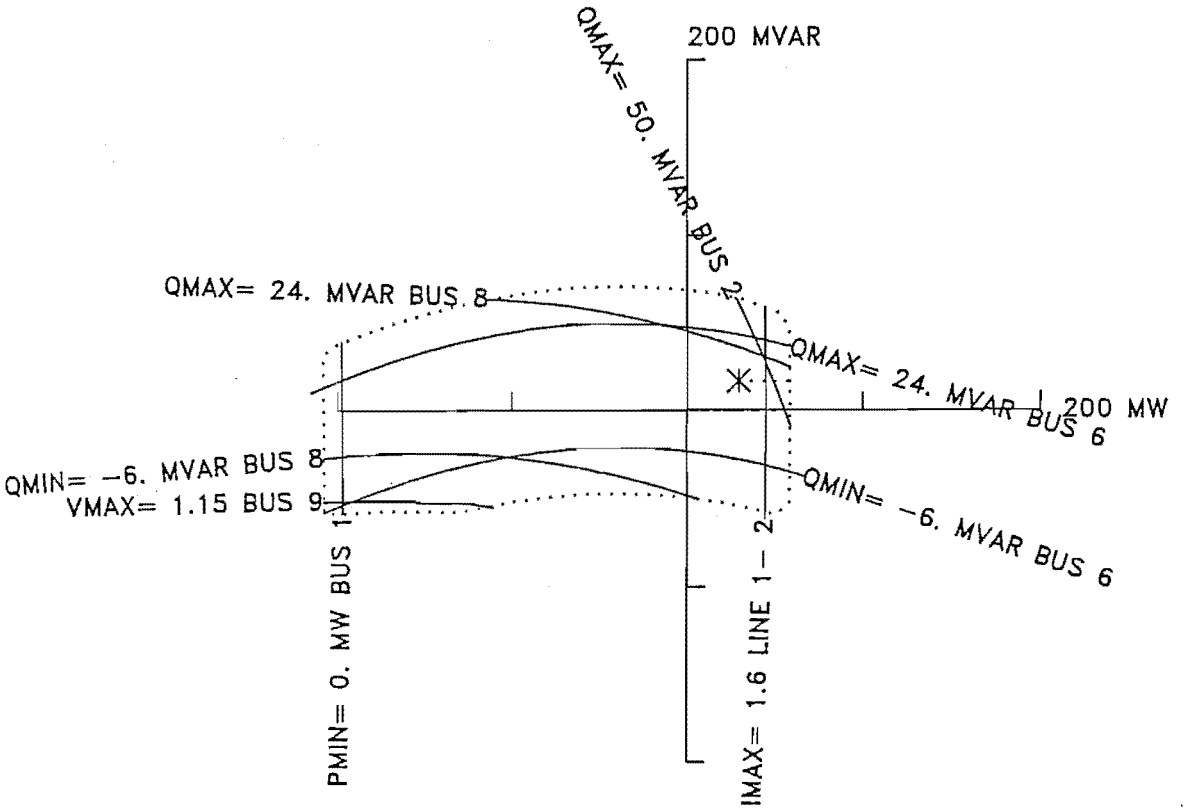

Figure 4.3 Capability Chart for Busbar 9

The specified busbar load is marked by a star in the operating region. This load is used as a seed for the capability charting algorithm. The dotted vicinity perimeter is constructed first, then all contours that intersect with the perimeter are traced through the vicinity.

Seed Point

An initial seed point within the operating region is provided by the user. The most convenient seed is usually the normal operating point of the system. In this case the normal operating point is a load of 29.5 MW and 16.6 MVAR at busbar 9 and has been identified by a star on the chart.

A fast decoupled powerflow algorithm as described by Stott and Alsac (1974) is then used to determine the state of the power system and to confirm that the seed is within the operating region. This powerflow technique has been chosen because of its proven reliability and speed. The matrices need to be factorised only once since the system configuration remains constant for each chart study. Any other powerflow could be substituted for the fast decoupled powerflow without altering the rest of the capability charting algorithm. In this case a worst power mismatch of 0.01 MVA was used as the criterion for powerflow convergence.

Search for Vicinity Perimeter

The next step in the charting algorithm is an exploration along a path heading away from the seed and searching for the vicinity perimeter. The exploration path consists of separate powerflow test points spaced 10 MVA apart. The path is marked on the chart by a dotted line extending from the seed, however this path is not normally displayed.

The excess values of each constraint are monitored along the path and intersections with constraint loci are recognized by the change of sign of the excess. An accurate position of each intersection is obtained by using the Newton-Raphson approach to finding the zero value of the excess as a function of distance along the exploratory path.

Contour Following Algorithm

Once the vicinity perimeter has been reached, a contour following algorithm is used to trace the vicinity perimeter defined by a violation index of 0.1 . Once again the excess values of each constraint are monitored so that intersections with constraint loci can be recognized and listed. The vicinity perimeter has been drawn with a dotted line on the chart in figure 4.3 but is not normally displayed.

The contour following algorithm requires a starting point on the contour before tracing can begin. An initial tangent to the contour is determined numerically by separately, and equally, peturbing the two coordinates of the starting point and finding a powerflow solution at each peturbation.

The constrained variable peturbation associated with the real power peturbation is Δ_P . The constrained variable peturbation associated with the reactive power peturbation is Δ_Q . The normal to the contour is then given by

$$\text{Normal} = \Delta_P + j\Delta_Q \qquad (4.4.2.1)$$

The tangent at the starting point then lies perpendicular to the normal.

Subsequent tangents are determined from the chord between the last two points on the contour as shown in figure 4.4 .

The contour tangent is used to estimate the position of the next point on the contour. The next point is STEP away from the last point. An approximation to the powerflow solution at the estimated point is made by a linear extrapolation from the known powerflow solutions at the last two points.

This approximate powerflow solution provides the initial conditions for an accurate powerflow solution at the estimated point. This determines the constrained variable's deviation DEV from the required contour value. If the deviation is less than the maximum permitted deviation DEVMAX then the algorithm has successfully found the next point on the contour.

If the contour deviation is too large then a Newton-Raphson technique is used to improve the estimate. The distance to the next point is kept as STEP but the direction α is altered. During each Newton-Raphson iteration the variation of DEV with respect to α is β which is numerically calculated by peturbing α and using a powerflow to find the associated peturbation in DEV.

$$\beta_i = \frac{\Delta DEV_i}{\Delta \alpha_i} \qquad (4.4.2.2)$$

An improved estimate α_{i+1} can then be calculated from

$$\alpha_{i+1} = \alpha_i - \frac{DEV_i}{\beta_i} \qquad (4.4.2.3)$$

Each change in α is limited to a maximum of 0.5 rads to prevent a wraparound that would cause the algorithm to retrace the contour in reverse.

The value of β changes slowly in magnitude as the contour is traced, however the sign of β remains constant. In regions of high contour curvature the calculated value of β may have the wrong sign. This is corrected by noting the true sign of β from previous calculations. Whenever the sign of β is incorrect it is replaced with a value of +0.2 or -0.2 to get the algorithm back on track. The suitability of these values was determined by experimentation on a variety of charts.

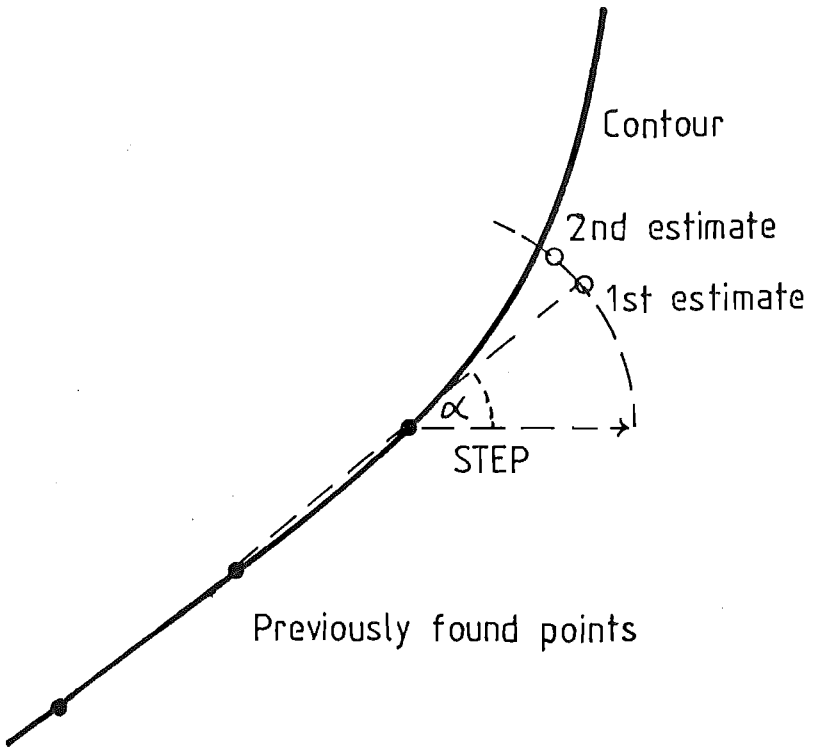

Figure 4.4 Contour Tracing

Two known points on the contour are used to form a tangent. This tangent is then used to estimate the position of the next point on the contour. A Newton-Raphson routine refines the estimate.

The capability charts in this chapter were drawn with the contour following parameters set at

STEP = 10 MVA

DEVMAX = 0.002 pu

Usually only one Newton-Raphson iteration was required to accurately find the position of a point on a contour.

This contour following algorithm will fail if the powerflow does not converge at any stage. The fast decoupled powerflow that is used can be expected to converge within the vicinity of the operating region for most practical power systems.

The intersection of a constraint contour with the vicinity perimeter is approximated by finding the intersection of the constraint contour with the chord between two points on the perimeter. A Newton-Raphson technique is again used to alter the position on the chord until the intersection point has been accurately found.

Tracing of Constraint Contours

After the vicinity perimeter has been traced, the list of constraint contour intersection points is examined. Each intersection point becomes the starting point for the contour following algorithm, which is now used to trace the constraint contour whilst it remains within the vicinity. The point where the contour exits the vicinity is also an intersection point and must be removed from the intersection list to prevent the contour being retraced later.

After each constraint contour has been traced, it is smoothed with a cubic spline and then drawn on the chart. A label is written at a tangent to the contour to explain its significance.

4.4.3 Interpretation of Capability Chart

The primary constraints shown on the capability chart in figure 4.3 are

1. Maximum current of 1.6 pu in the transmission line from busbar 1 to busbar 2. (This implies that both identical lines between busbar 1 and busbar 2 have reached their current limits of 1.6 pu each. The constraints of one line were ignored in order to reduce the total number of observed constraints. The presence of these constraints is not intuitively obvious because the transmission lines do not appear close to busbar 8 on the circuit diagram. However the chart clearly illustrates the nature of the constraints.)

2. Maximum reactive power of 50 MVAR from the generator at busbar 2.

3. Maximum reactive power of 24 MVAR from the synchronous compensator at busbar 8.

4. Maximum reactive power of 24 MVAR from the synchronous compensator at busbar 6.

5. Minimum power output of 0 MW from the slack generator at busbar 1.

6. Minimum reactive power of -6 MVAR from the synchronous compensator at busbar 8.

7. Minimum reactive power of -6 MVAR from the synchronous compensator at busbar 6.

The only secondary constraint evident in the vicinity of the operating region is the maximum voltage of 1.15 pu at busbar 9.

A large portion of the operating region lies in the negative real power half plane. This implies that the load may inject real power into the system. Most industrial and domestic consumer loads will not be capable of this so the negative real power half plane may be ignored in these cases. If the load represents another generation authority then excursions into this half plane will be quite feasible during inter-area power exchanges.

The accuracy of the capability chart was verified by undertaking a detailed powerflow analysis for selected operating points on the chart. The tabulated results from each powerflow output were consistent with the positions of the contours on the chart.

The capability chart shown in figure 4.3 was drawn in 16 seconds of CPU time on a VAX-11/750. The actual plotting time may take up to several minutes depending on the plotting device and graphics software that is used. The charts in this thesis were drawn with the assistance of the widely available PLOT79 graphics software package (Beebe, 1979).

The web of constraint loci is changed if the system configuration is altered. For example if the three winding transformer and synchronous compensator at busbar 8 are taken out of service then the capability chart for busbar 9 is altered to that shown in figure 4.5 . The removal of the transformer and compensator results in a much smaller operating region. Also the operating point lies very close to the boundary of the operating region near the contour representing maximum reactive power output from the generator at busbar 2.

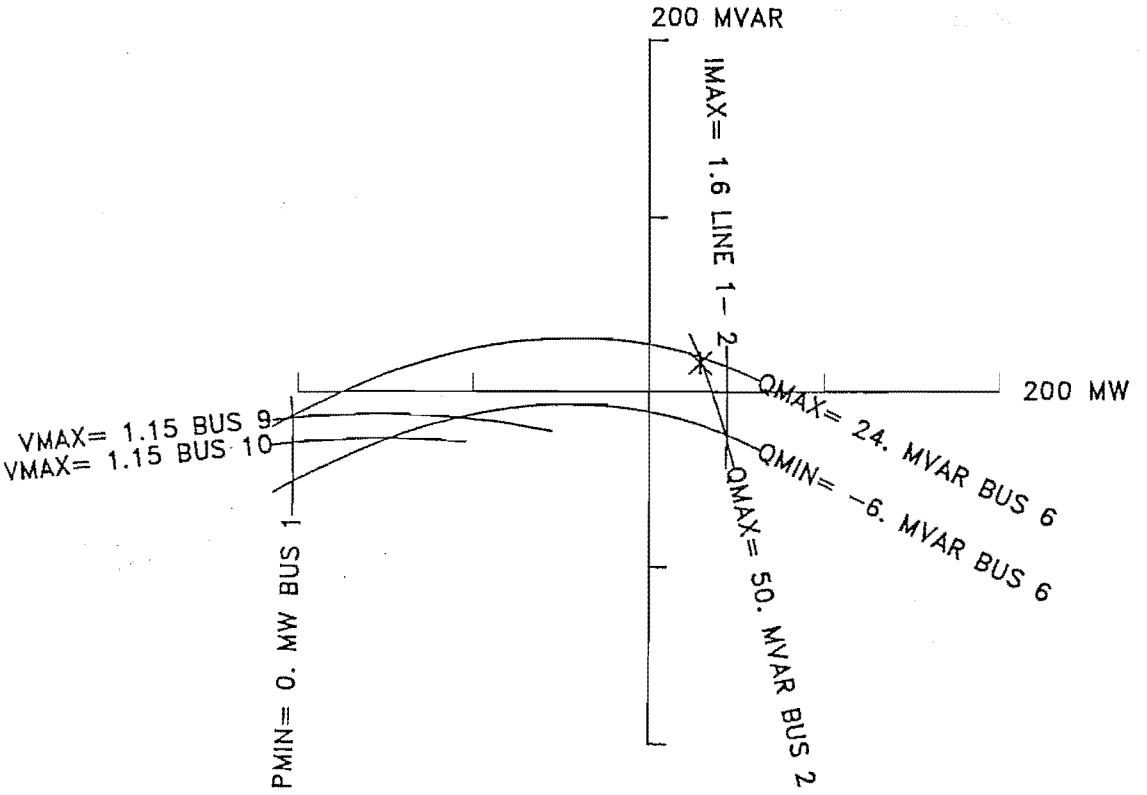

Figure 4.5 Capability Chart for Busbar 9 with Three Winding Transformer out of Service

The removal of the transformer results in a much smaller operating region compared to figure 4.3 . The specified operating point marked by a star now lies at the edge of the operating region.

4.4.4 Holes and Islands

This algorithm recognizes the existence of all contours that intersect the exploratory path or vicinity perimeter. The method cannot recognize contours that lie within the vicinity but do not intersect the path or perimeter. If such a contour exists it would form a hole in the operating region as shown in figure 4.6(a) .

The problem of undetected holes is complementary to the problem of undetected islands that are disjoint from the main operating region but still satisfy all constraints. Disjoint islands are shown in figure 4.6(b) . An operating point in one island cannot be moved into a separate island by adjusting the charted busbar loading, however the adjustment of loads at other busbars may fuse the separate islands to form a single operating region.

The presence of a hole or island may be tested for by carrying out a large number powerflows at various points on the chart. Any point lying within the ostensible operating region but not fulfilling all operating criteria would indicate the presence of a hole. Any point lying outside the operating region that did fulfil all criteria would indicate the presence of an island.

This method is extremely time consuming due to the large number of powerflows involved. Nonconvergent powerflows well beyond the operating region are especially time consuming. This is because a large number of powerflow iterations must be executed before the powerflow algorithm decides that convergence is not possible.

Tests on the capability charts drawn during this study have not shown any evidence of holes or islands. It may well be that the hole and island problem is academic.

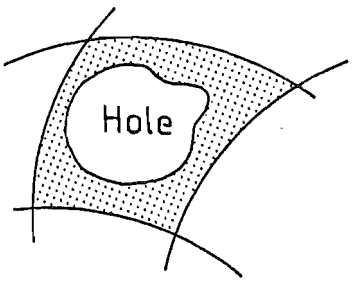

Figure 4.6(a) A Hole in the Operating Region

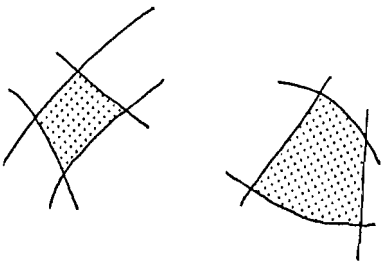

Figure 4.6(b) Disjoint Islands of Operating Regions

4.4.5 Shortened Labels for Diagram Dressing

The capability charts for some power systems can exhibit a large number of separate constraint contours that intermingle in a cluttered and confusing web. Figure 4.7(a) shows the capability chart associated with busbar 10. The long contour labels overlap and make the chart difficult to read.

The confusion can be alleviated by dressing the chart with short labels as shown in figure 4.7(b) . Each short label still uniquely identifies an operating constraint, although some details are omitted. For example V+10 implies the maximum allowable voltage at busbar 10 without specifically stating the voltage value of 1.15 pu. A user with some familiarity with this particular power system would realize that all the maximum busbar voltages were set at 1.15 pu.

4.5 CONCLUSION

This chapter has described a contour tracing algorithm that will draw a capability chart for any busbar in a large general AC power system. The system equations are solved by using an iterative powerflow rather than by the explicit equation derivations used for small systems.

The attention of the algorithm is restricted to the vicinity of the operating region so as to avoid unrealistic operating states. Each constraint locus is treated as a contour and is traced through the vicinity. The algorithm is demonstrated by drawing charts for the IEEE 14 busbar test system.

The algorithm is designed to cope with any twists in the contours but may not recognize holes in the operating region and other disjoint operating region islands. The problem of diagram cluttering is alleviated by the provision of an option to use short contour labels which display only the most essential information.

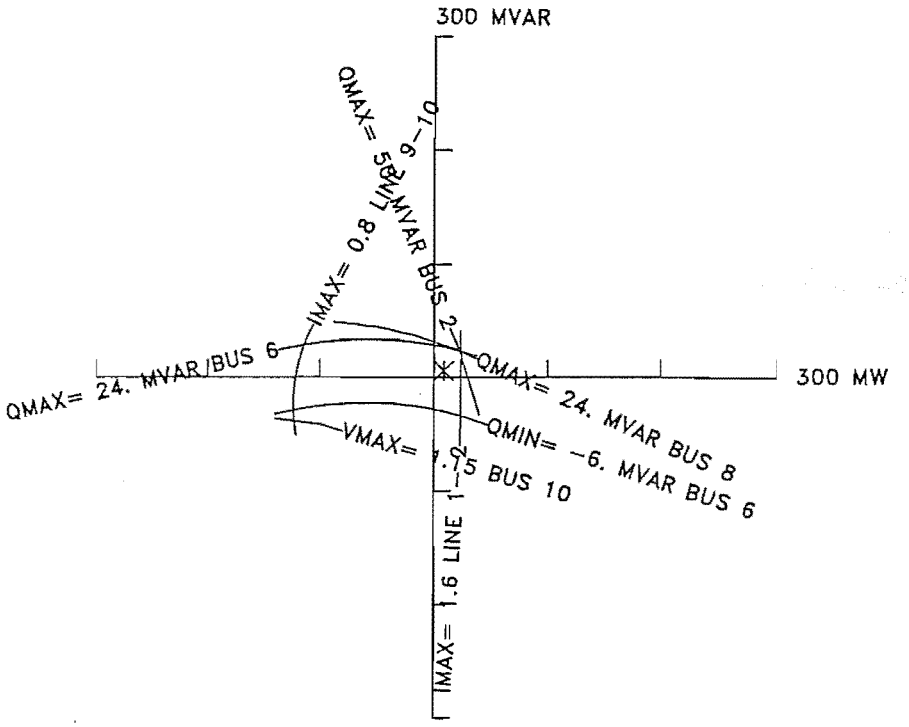

Figure 4.7(a) Cluttering Due to Long Labels

This capability chart for busbar 10 is difficult to read because of the overlapping contour labels.

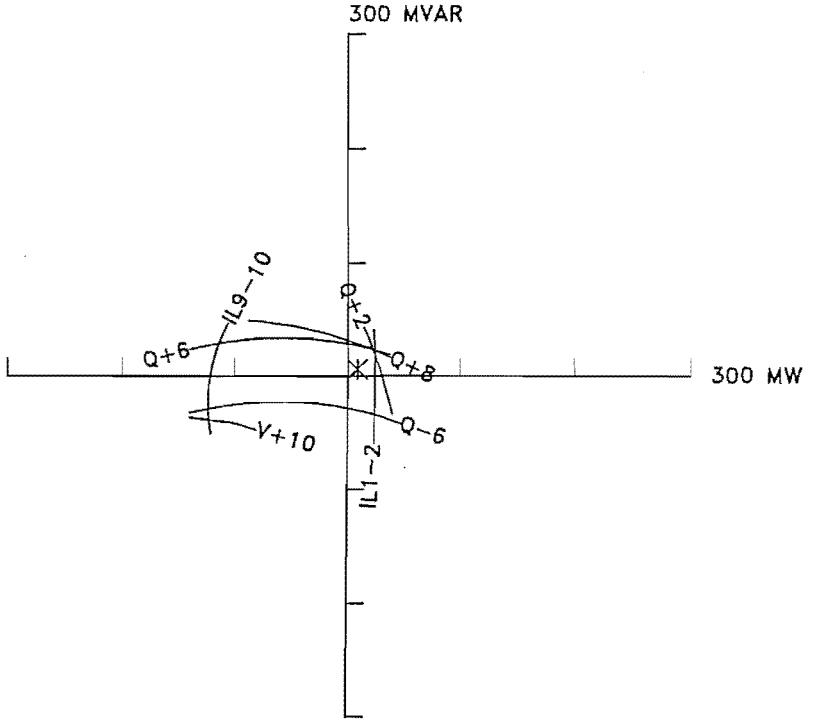

Figure 4.7(b) Shortened Labels to Improve Legibility

The shortened contour labels display only essential information.

Chapter 5
A Fast Capability Charting Algorithm

5.1 INTRODUCTION

Extensive use of the original capability charting algorithm described in chapter 4 provided insights into the nature of capability charts for large systems. In particular the capability charts eventually demonstrated that the constraint contours within the vicinity of the operating region are much better behaved than previously expected.

The families of voltage contours drawn by Price (1984) exhibited many twists and loops. This behaviour was observed because Price's contour maps covered large regions of the complex power plane and were not limited to the vicinity of the realistic operating region. In contrast, all of the charts drawn by the capability charting algorithms have shown that the contours in the vicinity of the operating region are very well behaved. This indicates that bad contour behaviour is associated with unrealistic operating states well outside the vicinity of the operating region.

Price's work influenced the design of the original capability charting algorithm to use the contour tracing approach to cope with the expected bad contour behaviour. The eventual good contour behaviour forced a reconsideration of the original capability charting algorithm and resulted in the design of a new fast capability charting algorithm that exploits the good contour behaviour to reduce the computation required to construct a capability chart.

This chapter describes the fast capability charting algorithm and compares its performance with the original contour tracing algorithm.

5.2 STRUCTURE OF THE FAST ALGORITHM

The technique used by the fast capability charting algorithm is demonstrated on the same IEEE 14 busbar test system shown in figure 4.1 as was used to demonstrate the original capability charting algorithm. The chart for busbar 9 is reconstructed so that the performances of the fast algorithm and the original algorithm can be fairly compared.

The structure of the fast capability charting algorithm is shown in figure 5.1 . First the power system data file is read in and a list of operating constraints is formed. These constraints are identical to those used by the original algorithm.

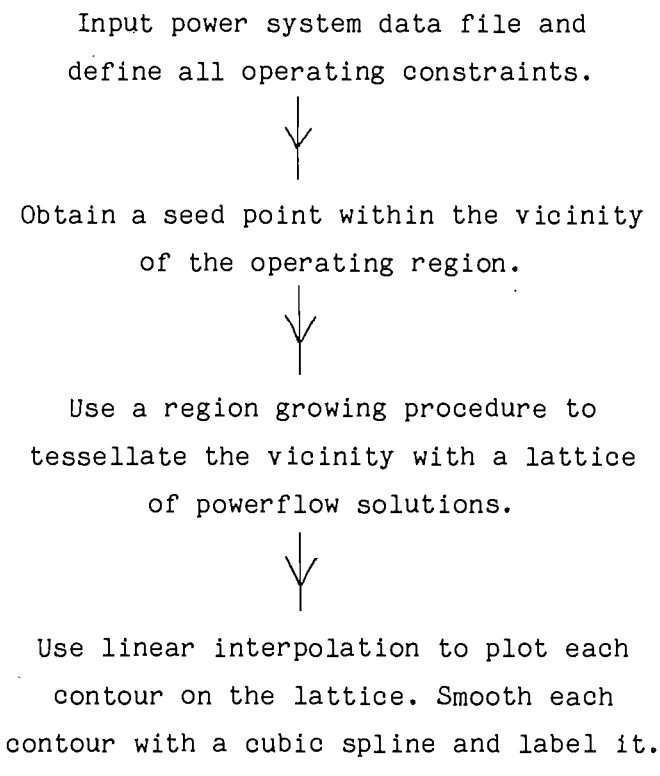

Figure 5.1 Structure of Fast Capability Charting Algorithm

A seed powerflow solution is then obtained to begin drawing the chart. This seed normally corresponds to the nominal system state that does not violate any constraints.

In a similar manner to the original algorithm, the vicinity of the operating region is defined as the region within which all constrained variables are less than 0.1 per unit beyond their limits. By restricting the investigation to the vicinity, the algorithm saves the unnecessary computation associated with the unrealistic states. This strategy also implicitly avoids the badly behaved contours that can occur well beyond the vicinity.

5.2.1 Region Growing

A region growing process is then used to locate the region covered by the vicinity. This process is similar to the technique used in computer vision systems to recognise shapes of objects (Ballard and Brown, 1982). The region growing process shown in figure 5.2 gradually tessellates the vicinity with a lattice of powerflow samples. The lattice points correspond to the vertices of packed equilateral triangles on the complex power plane. To clarify the region covered by the vicinity, the vicinity perimeter obtained from figure 4.3 (p. 65) has been superimposed onto the lattices.

In the first growth phase a powerflow is used to investigate the six nearest lattice vertices to the original seed. At each vertex the system constraints are examined to determine if the vertex is within the vicinity. If any constraint is found to have been exceeded it is added to a summary list of exceeded constraints. The busbar voltage vectors associated with each vertex are also stored for future reference.

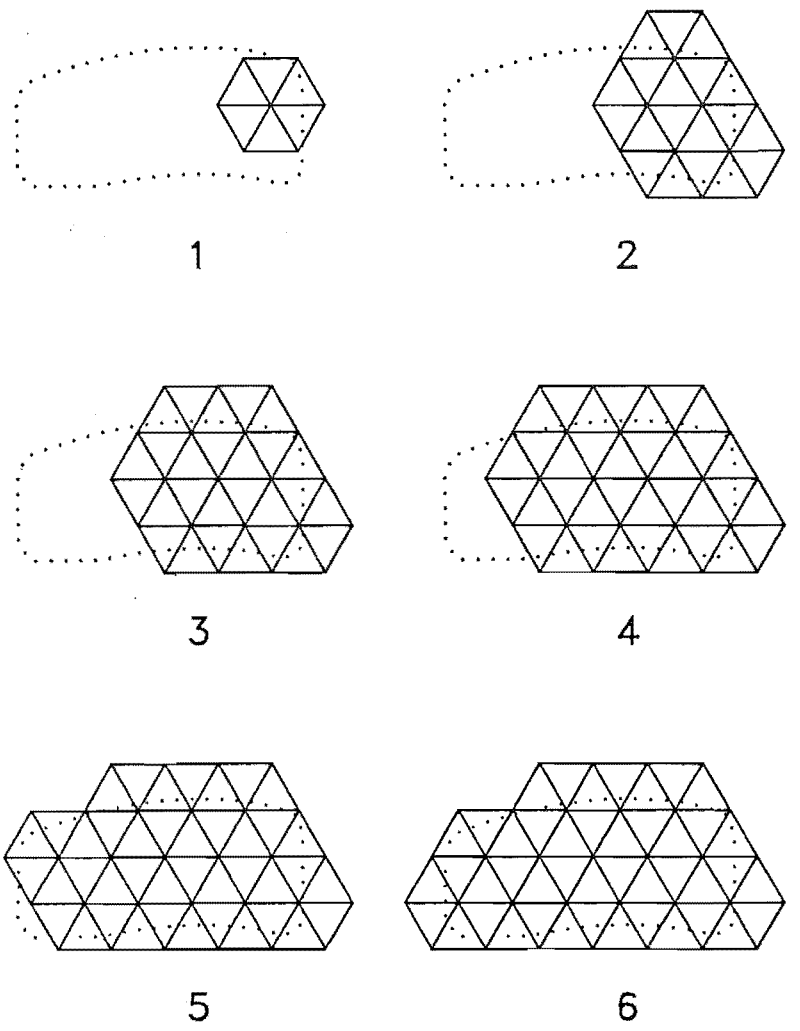

Figure 5.2 Region Growing

The vicinity of the operating region is tessellated by a lattice of powerflow solutions. The lattice is shown gradually growing over the vicinity in six growth phases.

During each subsequent growth phase the region is extended by observing the following four growing rules

1. If a newly grown vertex is within the vicinity then it may be used to grow any neighbours that have not yet been investigated.

2. Vertices that are found to be outside the vicinity may not be used for further growth.

3. If a vertex is associated with a non-converging powerflow then it is assumed to be a non-feasible solution and is excluded from the vicinity. For this rule to be properly applied a robust and reliable powerflow algorithm must be used. The fast decoupled powerflow described by Stott and Alsac (1974) was used in this demonstration and performed very well, converging at all lattice points.

4. The region growing is completed when no more vertices can be grown.

In this particular chart six growth phases were required to completely tessellate the vicinity. In the final growth phase shown, the lattice points around the edge of the region all correspond to rule 2 and lie just outside the vicinity. The distance between lattice points has been chosen to be 50 MVA. This choice is made by the algorithm's user and is a compromise between a small distance which would entail greater computation due to more lattice points and a large distance which would produce a very coarse lattice unsuited to interpolation. The behaviour of the contours also has a bearing on the choice of distance between lattice points. The presence of twisted contours requires a more densely packed lattice to ensure accurate contour plotting.

5.2.2 Contour Plotting

After the region grower has defined the vicinity of the operating region the list of exceeded constraints is examined. For each constraint on the list the stored array of busbar voltage vectors is used to calculate the value of the constrained variable at each vertex. Linear interpolation along the edges of each triangle is then used to estimate the points of intersection between the contour and the lattice. This estimate is very good because the contours are almost linear in the vicinity.

The individual contour intersection points are then joined together to complete each contour. Figure 5.3 shows the plot of the contour representing minimum reactive power output from the synchronous compensator at busbar 6.The contour is smoothed by applying a cubic spline to the interpolated points. All of the contours are then combined to form the capability chart shown in figure 5.4 .

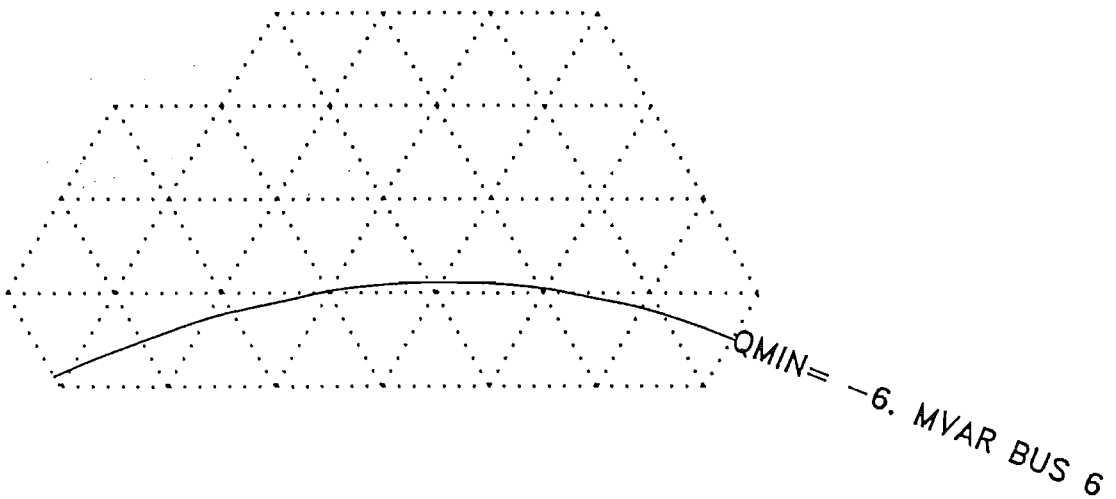

Figure 5.3 Plot of One Contour on Lattice

Linear interpolation is used to estimate the intersection points of the contour with the lattice. The intersection points are then linked together and the curve is smoothed with a cubic spline.

The capability chart produced by the fast algorithm portrays one extra contour than the chart in figure 4.3 (p. 65), which was produced by the original algorithm. The extra contour represents the maximum power output from slack busbar 1. This contour is actually outside the vicinity of the operating region and is included because the periphery of the lattice lies slightly beyond the vicinity perimeter.

The fast capability charting algorithm required 4 seconds of CPU time on a VAX-11/750 to draw the chart shown in figure 5.4 . This is four times faster than the original algorithm which required 16 seconds of CPU time to draw the chart shown in figure 4.3 to the same accuracy. This improvement in speed is typical of performance comparisons using other charts.

The use of the fast algorithm can partially solve the theoretical hole and island problem discussed in chapter 4, section 4.4.4 . A sufficiently dense powerflow lattice will identify any hole in the operating region provided that the hole includes at least one lattice vertex. The drawback to this is that a dense powerflow lattice necessitates a large amount of CPU time.

In contrast a sparse lattice, with a large distance between vertices, could be used to identify disjoint islands. The peripheral vertices of the sparse lattice will extend well beyond the local vicinity and may consequently lie within a separate disjoint vicinity. If this occurs then the region growing procedure will continue to grow the lattice until both islands have been tessellated.

The ability of the fast algorithm to deal with holes and islands is purely speculative since neither holes nor islands have yet been found.

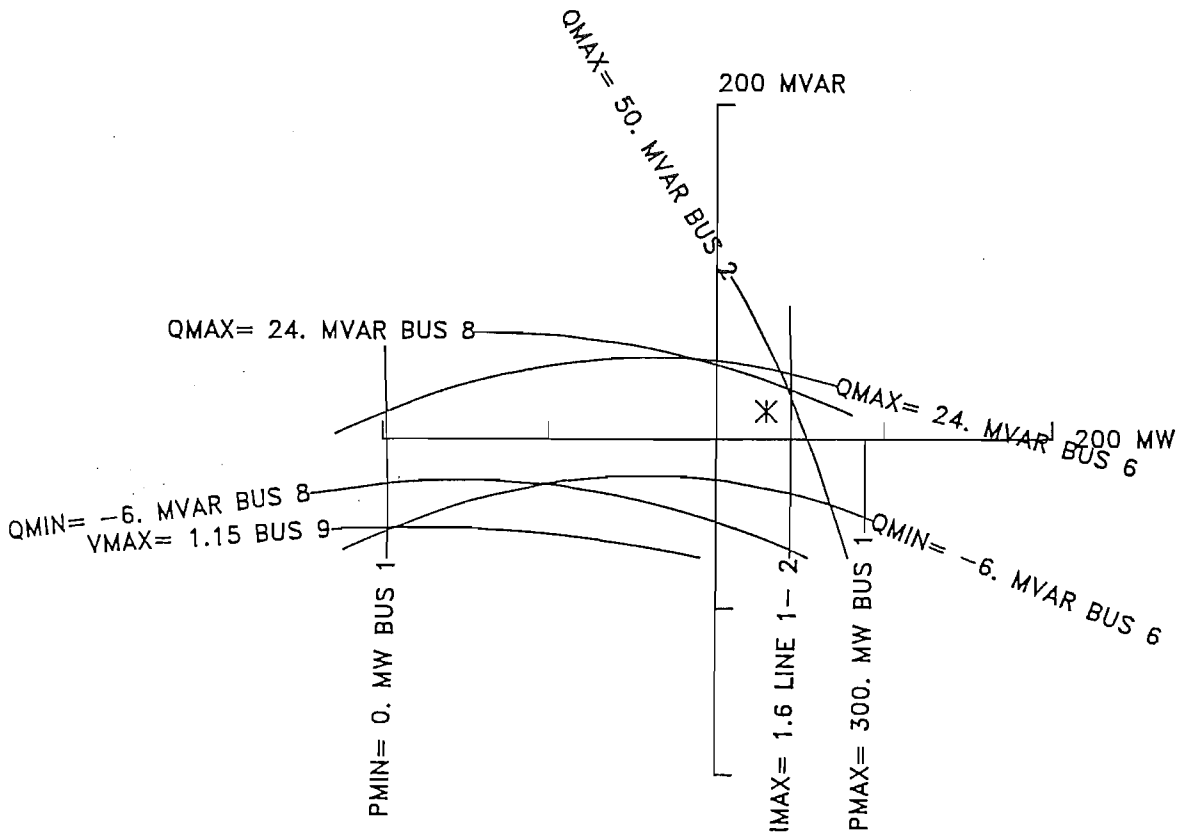

Figure 5.4 Complete Capability Chart as Drawn by Fast Algorithm

This chart is for busbar 9 of the IEEE 14 busbar system. It should be compared with figure 4.3 (p. 65) which shows the same chart as drawn by the contour tracing algorithm.

5.3 POWERFLOW CONVERGENCE BOUNDARY

The fast capability charting algorithm is sufficiently robust to cope with nonconverging powerflows, unlike the original algorithm which will fail if convergence is not achieved.

The failure of a powerflow to converge to a solution can indicate that either the powerflow algorithm cannot find a realistic solution or that such a solution is impossible to achieve. In either case it is useful to indicate regions of nonconvergence on the capability chart.

The boundary of the convergence region on the chart is constructed by linking together all of the convergent lattice points that are adjacent to nonconvergent lattice points. This is illustrated in figure 5.5 which uses the fast algorithm to reconstruct the transmission line capability chart shown in figure 2.11 (p. 27). The undesirable zigzag behaviour of the convergence boundary must be accepted because interpolation cannot be used to provide a smooth curve.

The voltage and current contours in figure 5.5 match the corresponding loci in figure 2.11 . The theoretical voltage stability boundary from figure 2.11 has been superimposed onto figure 5.5 and approximately matches the powerflow convergence boundary. In this particular case, knowledge of the transmission line chart from chapter 2 verifies that the convergence failures are due to nonexistent solutions rather than the unreliability of the fast decoupled powerflow.

It is tempting to always associate the convergence boundary with the edge of a region of nonexistent solutions. However this is only valid if convergence failure is not due to an unreliable powerflow.

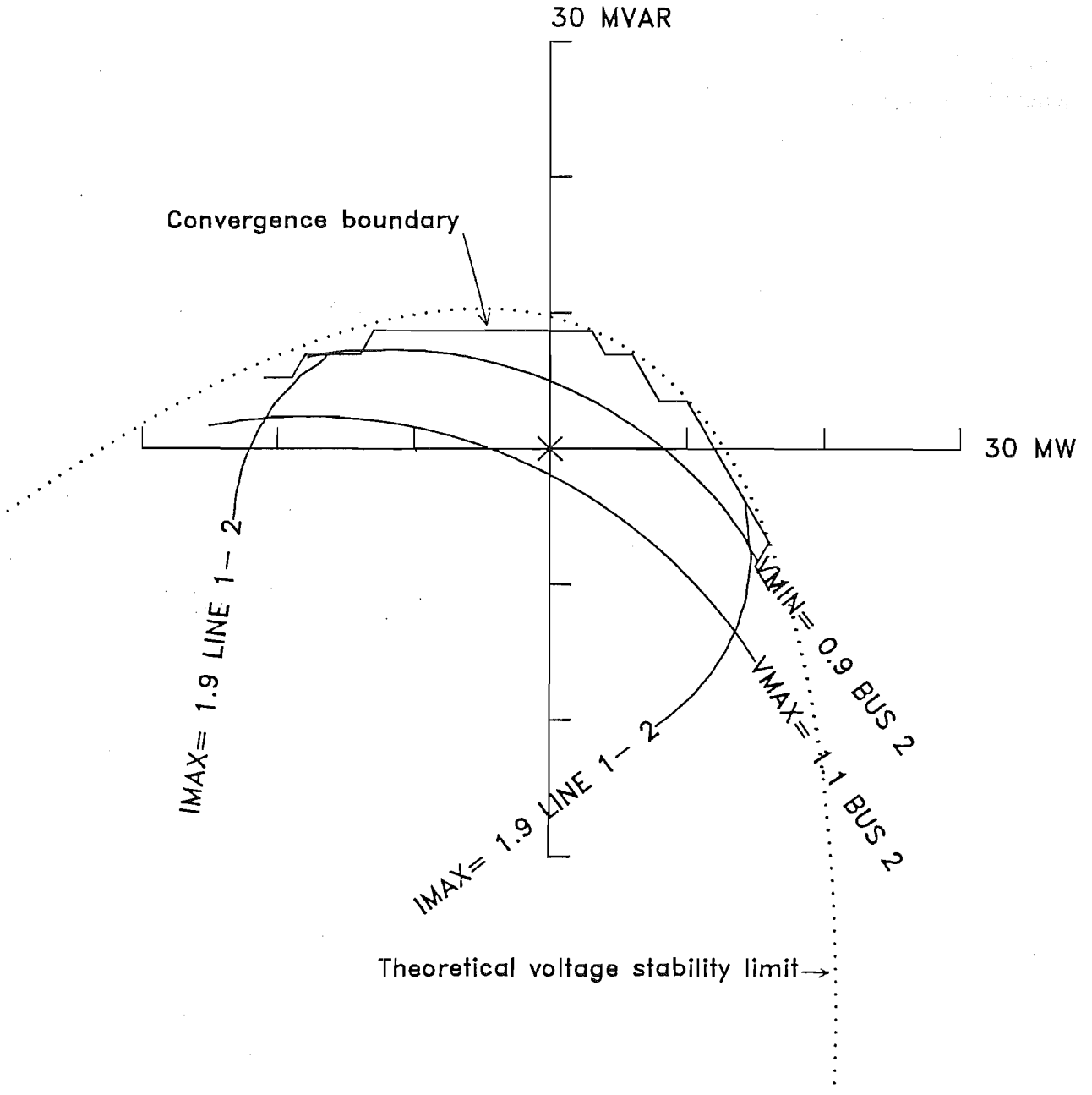

Figure 5.5 Powerflow Convergence Boundary

The powerflow convergence boundary approximates the position of the theoretical voltage stability limit. This chart corresponds to the chart shown in figure 2.11 (p. 27)

5.4 CONTOUR MAPS

The fast algorithm can also be used to construct contour maps on the complex power plane. Instead of drawing contours for several different constrained variables, the algorithm is restricted to drawing a family of contours that represents one particular variable.

The vicinity of the operating region is first defined by the region growing technique. The algorithm's user then specifies the variable that is to be represented by the contour map. The user must also specify the difference between successive contour values. Each separate contour of the family is then drawn over the lattice in the same way as the critical constraint contours are drawn on the capability chart.

Figure 5.6 shows a contour map that represents the voltage at busbar 9 as a function of the complex power consumed at busbar 9 of the IEEE 14 busbar test system. The powerflow lattice used to construct this contour map is the same as the lattice shown in figures 5.2 and 5.3 . The star on the contour map indicates the nominal load at busbar 9.

This map is useful for studying the manner in which the voltage will change as the load power consumption slowly changes. The map is invalid for rapid load changes because steady state operation must be assumed.

The contour maps are similar to those drawn by Price (1984). However these maps are restricted to the vicinity of the operating region whilst Price's maps can cover any specified area of the complex power plane.

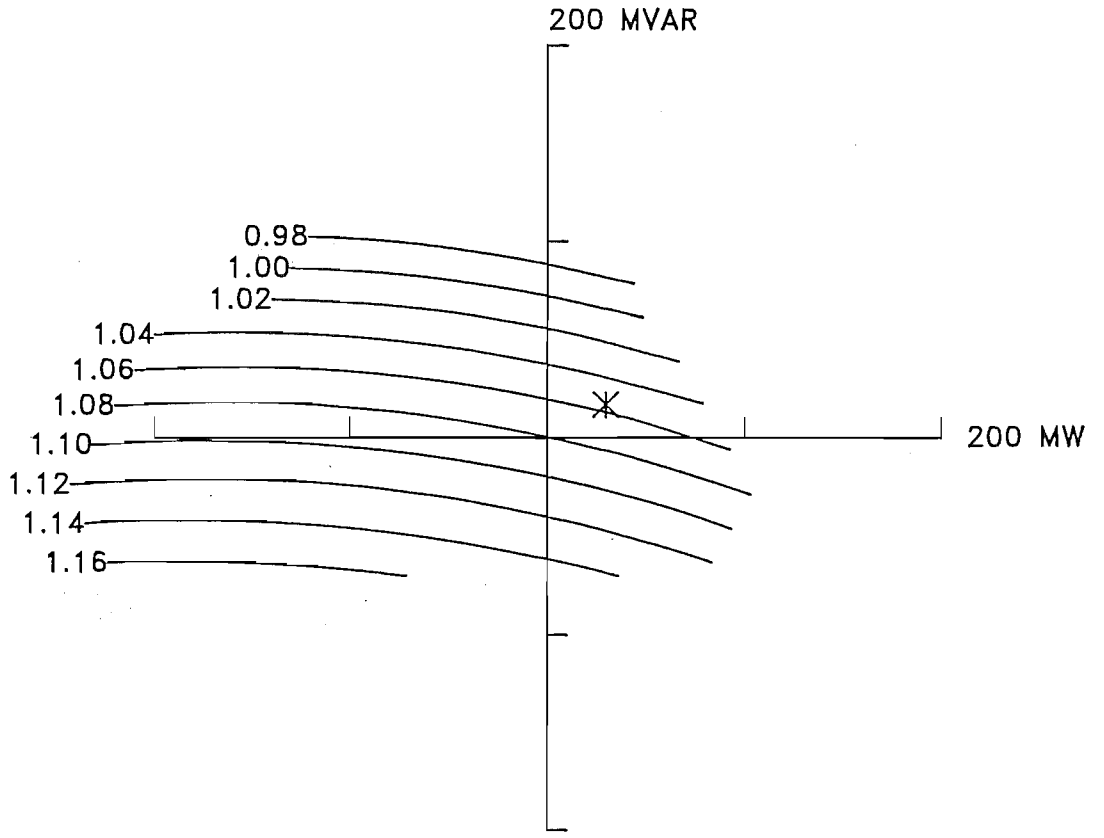

Figure 5.6 Voltage Contour Map

This map represents the busbar 9 voltage as a function of the busbar 9 loading. The map can be used to judge the effect of slow load fluctuations upon the busbar voltage.

5.5 CONCLUSION

Extensive use of the original capability charting algorithm showed that the constraint contours for many practical power systems are extremely well behaved in the vicinity of the operating region. This good behaviour has been exploited in a new fast capability charting algorithm.

The fast algorithm uses a region growing technique borrowed from computer vision systems to tessellate the vicinity of the operating region with a lattice of powerflow samples. The system constraint contours are then drawn by using linear interpolation between the lattice points.

The fast algorithm is demonstrated by constructing the same chart as was used to demonstrate the original contour tracing algorithm. This allows a comparison of performance and shows that the fast algorithm is about four times faster than the original algorithm.

The fast algorithm allows a powerflow convergence boundary to be added to the capability chart. In the case of a simple transmission line, the convergence boundary corresponds to the theoretical voltage stability boundary.

A modification to the fast algorithm allows contour maps to be drawn. These maps can be used to study the effect of slow load fluctuations on other system variables.

Chapter 6
Charts for Large AC/DC Systems

6.1 INTRODUCTION

The contour following capability charting algorithm described in chapter 4, and the fast capability charting algorithm described in chapter 5, are both restricted to drawing charts for AC power systems. To make the charts applicable to the ever increasing number of AC/DC schemes, both algorithms must be extended to cope with the additional operating constraints imposed by the DC systems.

This extension parallels the previous development of the charts for small systems, in which the analysis of the synchronous generator and transmission line was extended to describe the performance of a combined AC system and HVDC link.

Two types of DC system are catered for; the DC rectifier and the two terminal HVDC link. Both types of system may be controlled by a variety of operating strategies.

In order to incorporate these systems into the capability charting algorithms, the DC system operating constraints must be identified and the powerflow routine must be modified to cope with the analysis of AC/DC systems.

6.2 OPERATING CONSTRAINTS OF DC SYSTEMS

The operating constraints that govern the performance of the AC/DC converters in the NZ Benmore-Haywards HVDC scheme have been previously discussed in chapter 3. The capability charting algorithms recognize similar constraints in the operation of DC rectifiers and HVDC links.

6.2.1 Constraints of DC Rectifier

The circuit model of the DC rectifier is shown in figure 6.1 . Power to the rectifier is supplied from an AC busbar at a voltage V_{ac} . A converter transformer provides a commutation reactance of X_c and a tap ratio of a. The rectifying converter employs 12 pulse operation and supplies DC power to a load consisting of a smoothing reactor and a resistance R_{dc} in series with a back emf of E_{dc} .

The allowable operating modes of the rectifier are

1. Constant firing angle.
2. Constant DC current.
3. Constant real power.

The rectifier operating constraints that are considered are

1. Minimum firing angle in converter.
2. Minimum DC holding current through converter valves.
3. Maximum DC current through converter valves.
4. Maximum commutation angle of 60 degrees.

The maximum DC voltage constraint has been omitted because it is assumed that the system can withstand the maximum DC voltage that is imposed when the AC busbar voltage and converter transformer tap are set at their maximum limits and the firing angle is set at zero.

6.2.2 Constraints of HVDC Link

The circuit model of the two terminal HVDC link is shown in figure 6.2 . One end of the link is nominated as the rectifier and the other end is nominated as the inverter. The 12 pulse rectifier is supplied from an AC busbar at voltage V_{acr} through a converter transformer with tap a_r and commutating reactance X_r . The rectifier transfers power to the inverter through a DC transmission line that has smoothing reactors and a resistance of R_{dc} . The inverter circuit is modelled in the same way as the rectifier circuit , the inverter parameters being identified by the subscript i instead of r.

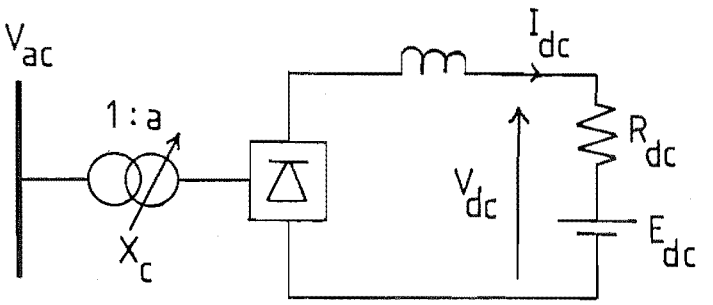

Figure 6.1 Circuit Model of DC Rectifier

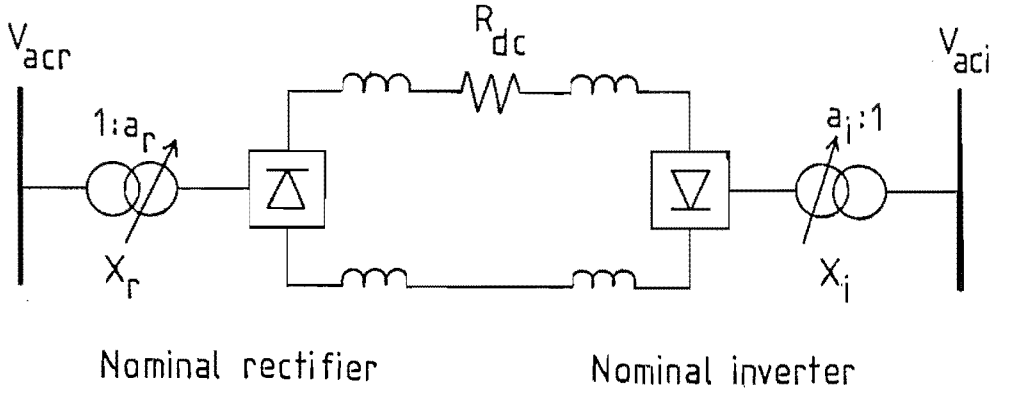

Figure 6.2 Circuit Model of Two Terminal HVDC Link

The allowable operating modes of the HVDC link are

1. Constant rectifier real power input and constant inverter extinction angle.

2. Constant DC current and constant inverter extinction angle.

3. Inverter operating as a power frequency controller with a constant extinction angle, and a real power output which acts to keep constant system frequency. The AC busbar attached to this inverter becomes the slack busbar for real power, hence the voltage angle is fixed. The voltage magnitude is still allowed to vary.

4. Inverter operating as a slack generator. The real power output of the inverter maintains a constant system frequency and the reactive power output of the inverter maintains a constant voltage at the inverter AC busbar. The AC busbar attached to the inverter is the slack busbar.

The operating constraints of the HVDC link that are considered are

1. Minimum firing angle in the nominal rectifier.
2. Minimum firing angle in the nominal inverter.
3. Minimum extinction angle in the nominal rectifier.
4. Minimum extinction angle in the nominal inverter.
5. Minimum dc holding current.
6. Maximum dc current.
7. Maximum commutation angle of 60 degrees in the nominal rectifier.
8. Maximum commutation angle of 60 degrees in the nominal inverter.

Similarly to the DC rectifier, the DC voltage constraints of the HVDC link are not considered.

6.2.3 Allowable Range of Values for DC System Variables

Both the contour tracing capability charting algorithm, and the fast capability charting algorithm, require that the system parameters vary smoothly as the operating state changes. The algorithms cannot construct the constraint contours in the presence of discontinuities and undefined states.

The operation of the AC power system is described by the conventional powerflow equations that have no discontinuities, hence the AC system contours are easily constructed. In contrast, the operating equations of the AC/DC converters (as described in chapter 3) are prone to producing undefined states.

For example, if the DC rectifier circuit shown in figure 6.1 is operating in the constant DC current mode then the DC voltage V_{dc} is given by

$$V_{dc} = E_{dc} + I_{dc}.R_{dc} \qquad (6.2.3.1)$$

The firing angle α is obtained by rearranging (3.4.2.4) to give

$$\cos(\alpha) = \frac{V_{dc} + K_2.X_c.I_{dc}}{K_1.a.V_{ac}}$$

$$= \frac{E_{dc} + I_{dc}.R_{dc} + K_2.X_c.I_{dc}}{K_1.a.V_{ac}} \qquad (6.2.3.2)$$

The firing angle α is smoothly defined whilst $\cos(\alpha)$ remains in the range of -1 to +1 . However if the AC voltage V_{ac} drops below the critical value given by

$$V_{ac,critical} = \frac{E_{dc} + I_{dc}.R_{dc} + K_2.X_c.I_{dc}}{K_1.a} \qquad (6.2.3.3)$$

then $\cos(\alpha)$ will exceed +1 and α will be undefined. This signifies that the AC busbar voltage is insufficient to sustain the constant current I_{dc} , and that a different mode of rectifier operation must be used.

The changeover of operating mode will disrupt the smoothness of the contours on the capability chart and the charting algorithms may consequently fail to work.

This problem is overcome by recognizing cos(α) as the system variable rather than α. Cos(α) is now permitted to vary beyond the range of -1 to +1 because the conversion to α is never made. Similarly, the extinction angle δ is always recognized in the form cos(δ). The operating mode of the converter is not changed hence the system parameters vary smoothly and can be easily represented by contours.

The drawback of this method is that the capability chart contours represent an invalid converter operating mode in regions where cos(α) or cos(δ) are beyond their defined range. Nevertheless the integrity of the operating region is still maintained because the minimum allowable values of α and δ always ensure that the invalid regions of the chart lie outside the operating region.

6.3 IMPROVING THE SEQUENTIAL AC/DC POWERFLOW

The AC system powerflow used by the capability charting algorithms must be extended to handle AC/DC systems in order to determine the operating values of the constrained DC variables. The extended powerflow uses the sequential approach to solving the AC/DC system equations.

Sequential AC/DC powerflow algorithms are popular for determining the steady state operation of AC/DC power systems. This popularity stems from the ease of incorporating a sequential algorithm into existing AC powerflow programs. Unified or simultaneous algorithms can converge to a solution faster than sequential algorithms but the unified methods are much more difficult to program (Arrillaga et al., 1983).

The sequential powerflow that is used here is based on existing conventional sequential routines but also incorporates a simple new modification that improves the convergence characteristics. A short paper on this improved sequential powerflow has been submitted for publication in the Electric Energy Systems Journal (de Silva and Arnold, 1987).

6.3.1 Conventional Sequential Powerflow

Existing sequential powerflow algorithms solve the AC and DC system equations separately in an iterative fashion. When the DC equations are being solved, the AC system is modelled as a set of constant voltage busbars at each AC/DC converter terminal. The real and reactive power consumption of each converter is determined so that when the AC equations are being solved , the DC system can be modelled as constant real and reactive power injections into the AC network.

This technique permits well known AC powerflow algorithms, such as the fast decoupled powerflow (Stott and Alsac, 1974), to be used during each AC iteration. The analysis of the DC system can be easily added to an existing AC powerflow algorithm.

The main weakness of the conventional sequential powerflow involves the modelling of the DC system as constant real and reactive power injections during the AC iteration. The real power injection is known to be approximately constant (Arrillaga et al., 1983), but the reactive power injection is highly dependent on AC voltage, particularly at rectifying converters.

The convergence failures of conventional sequential powerflows can usually be attributed to the algorithm disregarding the voltage dependence of converter reactive power injection. This dependency is particularly significant if the AC system is weak with respect to the converter busbars.

6.3.2 Improving the Sequential Powerflow

The sequential powerflow may be improved during the AC iteration by modelling the DC system as a constant real power injection and a voltage dependent reactive power injection.

If Stott and Alsac's fast decoupled powerflow is being used for the AC iteration then the AC system equations are solved using a Newton-Raphson technique with constant Jacobians. The standard matrix equations for this technique are

$$[\Delta\theta] = [B']^{-1}\left[\frac{\Delta P}{V}\right] \qquad (6.3.2.1)$$

$$[\Delta V] = [B'']^{-1}\left[\frac{\Delta Q}{V}\right] \qquad (6.3.2.2)$$

where $[\Delta P/V]$ and $[\Delta Q/V]$ are the vectors of real and reactive power mismatches at each busbar divided by the corresponding voltage magnitudes. $[\Delta\theta]$ and $[\Delta V]$ are the vectors of changes required in voltage angle and magnitude to minimize the mismatches.

The elements of the Jacobian matrix B'' are equal to the imaginary parts of the corresponding elements of the admittance matrix for the AC system. The elements of the Jacobian matrix B' also correspond to the imaginary parts of the admittance matrix, however shunt susceptances are neglected since they mainly affect reactive powerflows. Both B' and B'' are symmetric.

Equations (6.3.2.1) and (6.3.2.2) are solved iteratively to find the voltage vector solution that is associated with zero real and reactive power mismatches.

Each element of B'' is a constant approximation to the true Jacobian element.

$$B''_{ij} \approx \frac{\partial(Q_i/V_i)}{\partial V_j} \qquad (6.3.2.3)$$

To improve the sequential powerflow algorithm, (6.3.2.3) must be reconsidered for each converter busbar k. The diagonal element of B'' corresponding to busbar k is modified to incorporate the variation of converter reactive power Q_{dck} with voltage V_k .

$$B'''_{kk} = B''_{kk} + \frac{\partial(Q_{dck}/V_k)}{\partial V_k} \qquad (6.3.2.4)$$

Including the dependency between reactive power at one converter and AC voltage at a different converter would involve off diagonal elements of B'' . These off diagonal elements are neglected in order to preserve the symmetry of the Jacobian. The modified Jacobian B''' is therefore identical to the original B'' apart from the the diagonal elements that correspond to converter busbars.

A good approximation to the diagonal element B'''_{kk} must be found before the powerflow iteration sequence begins. This approximation is made numerically by setting the converter AC voltages to a nominal 1 pu and solving the DC equations to find Q_{dck} at each converter. The voltage V_k at each converter busbar k are then individually peturbed and the DC equations are solved again to find the associated peturbation in Q_{dck} . These peturbations allow B'''_{kk} to be evaluated from (6.3.2.4).

The sequential AC/DC powerflow algorithm can then proceed using B''' in place of B'' in (6.3.2.2) during the solution of the AC system equations.

6.3.3 Comparison of Convergence Behaviour

The AC/DC power system shown in figure 6.3 is used as a test case to demonstrate the improvement in the sequential powerflow. The parameters of the system are given in table 6.1 . The DC rectifier at busbar 3 is operating in the constant power mode. The rectifier of the HVDC link at busbar 4 is operating under constant current control and the inverter at busbar 5 is operating under constant extinction angle control.

A maximum power mismatch of 0.1 MVA was used as the criterion for powerflow convergence. A flat 1 pu voltage profile was used to initiate the powerflows.

The improved sequential powerflow with the modified Jacobian converged to a solution in 5 real power and 5 reactive power iterations. This was faster than the conventional sequential powerflow which required 8 real and 9 reactive power iterations.

Table 6.1 Parameters of AC/DC Power System

AC SYSTEM

Power base	100 MVA
Transmission line reactances	0.100 pu
Transmission line resistances	0.002 pu
Transmission line maximum currents	2.0 pu
Filter shunt susceptance on busbar 3	0.3 pu
Filter shunt susceptances on busbars 4 and 5	0.4 pu
Generator voltages	1.1 pu
Slack generator busbar 1 power limits	0 to 200 MW , -150 to 150 MVAR
Slack generator busbar 2 power limits	0 to 200 MW , -150 to 150 MVAR
Busbar voltage limits	0.9 to 1.1 pu
Busbar 7 loading	100 MW , 10 MVAR
Busbar 8 loading	100 MW , 70 MVAR

HVDC LINK

Commutation reactances	0.1 pu
Minimum firing angles	3.0 deg
Minimum extinction angles	10.0 deg
Minimum DC current	0.1 pu
Maximum DC current	1.0 pu
Transformer tap ratios	1.0
DC transmission line resistance	0.01 pu
Busbar 4 rectifier constant current control set at	0.85 pu
Busbar 5 inverter constant extinction angle set at	10.0 deg

DC RECTIFIER

Commutation reactance	0.1	pu
Minimum firing angle	3.0	deg
Minimum DC current	0.1	pu
Maximum DC current	1.0	pu
Transformer tap ratio	1.0	
Constant power setting	80	MW
DC resistance	1.0	pu
DC back emf	0.1	pu

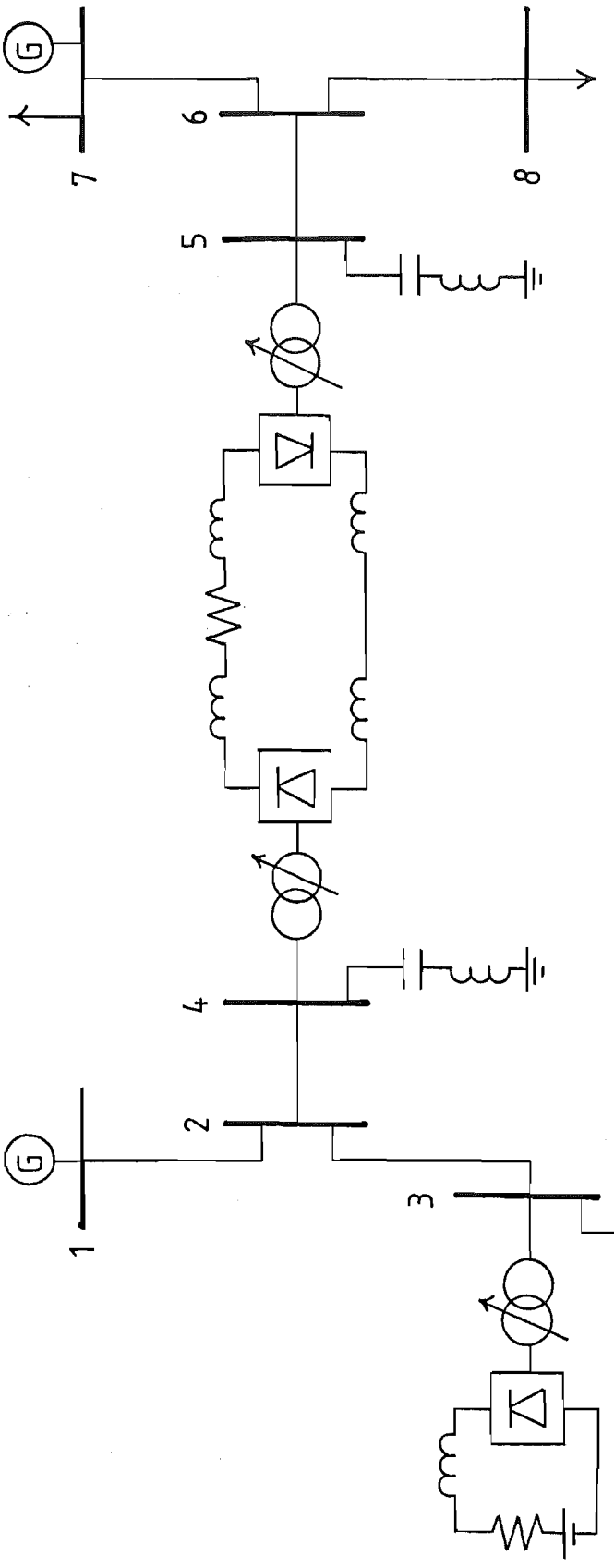

Figure 6.3 AC/DC Power System

The convergence patterns of the rectifier AC voltage at busbar 4 are compared in figure 6.4(a) . This shows that the convergence of the conventional powerflow is only slightly more oscillatory than the improved powerflow. In this case there is no clear superiority shown by the improved powerflow.

In the case of weak AC systems the improved powerflow does perform much better than the conventional powerflow. A very weak AC system was modelled by increasing the reactance of the transmission lines linking busbar 2 to 4 and busbar 5 to 6 from 0.1 pu to 0.4 pu. The voltage at the converter busbars was sustained by increasing the shunt susceptances from 0.4 pu to 0.6 pu.

The improved sequential powerflow converged to a solution for the weak system in 7 real power and 7 reactive power iterations. The convergence pattern of the rectifier AC voltage at busbar 4 is shown in figure 6.4(b) . This figure also shows the conventional sequential powerflow rapidly diverging from the solution.

The two types of powerflow were also compared on the modified IEEE 14 busbar system which was used by Arrillaga et al. (1983) to test various sequential and unified powerflow algorithms. In this system, the transmission line between busbars 4 and 5 is replaced by a series connection of two weak transmission lines and an HVDC link. These circuit modifications are detailed in the appendix.

The HVDC link was set to operate with constant power control at the rectifier, and constant extinction angle control at the inverter. The improved sequential powerflow required 4 real power and 4 reactive power iterations to converge to a solution with a power mismatch of less than 0.1 MVA . (In this case, the rapid convergence matched the speed of convergence of the unified powerflow algorithms.) The conventional sequential powerflow performed poorly, requiring 17 real power and 19 reactive power iterations to reach the same solution.

The convergence characteristics of the two types of powerflow algorithm have also been compared for several other AC/DC systems. If the AC system is strong at the converter busbar then the convergence characteristics tend to be similar. As the AC system becomes weaker then the improved algorithm performs better than the conventional algorithm.

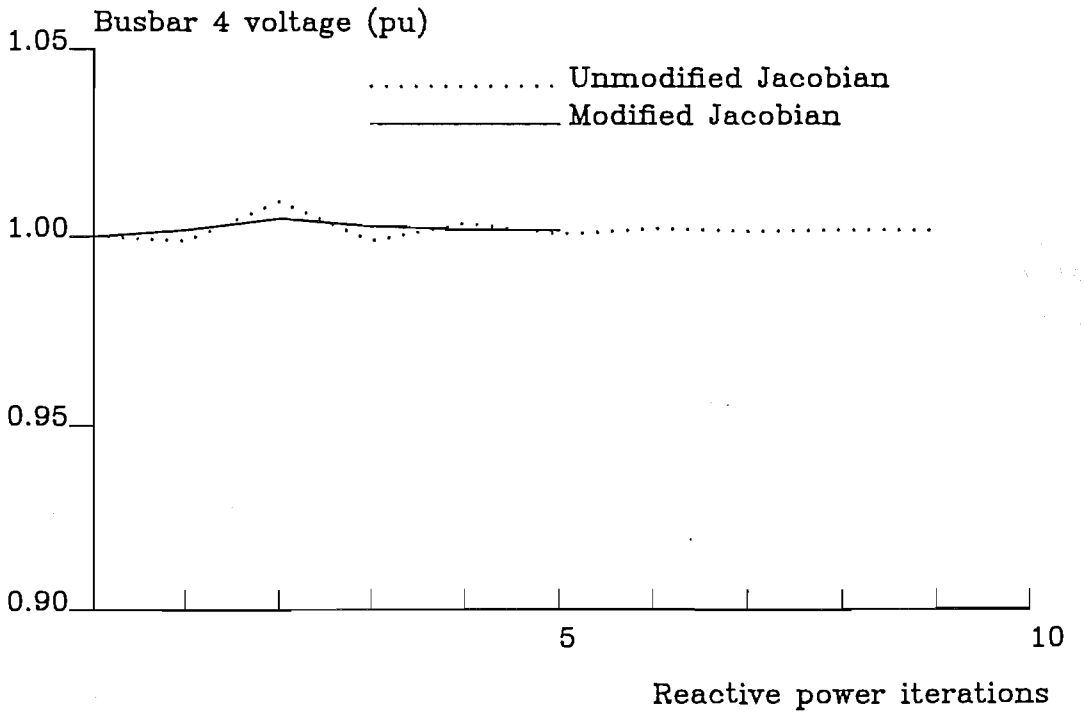

Figure 6.4(a) Powerflow Convergence for Strong AC System

In this case the improved sequential powerflow, using a modified Jacobian, converges to the solution slightly faster than the conventional sequential powerflow.

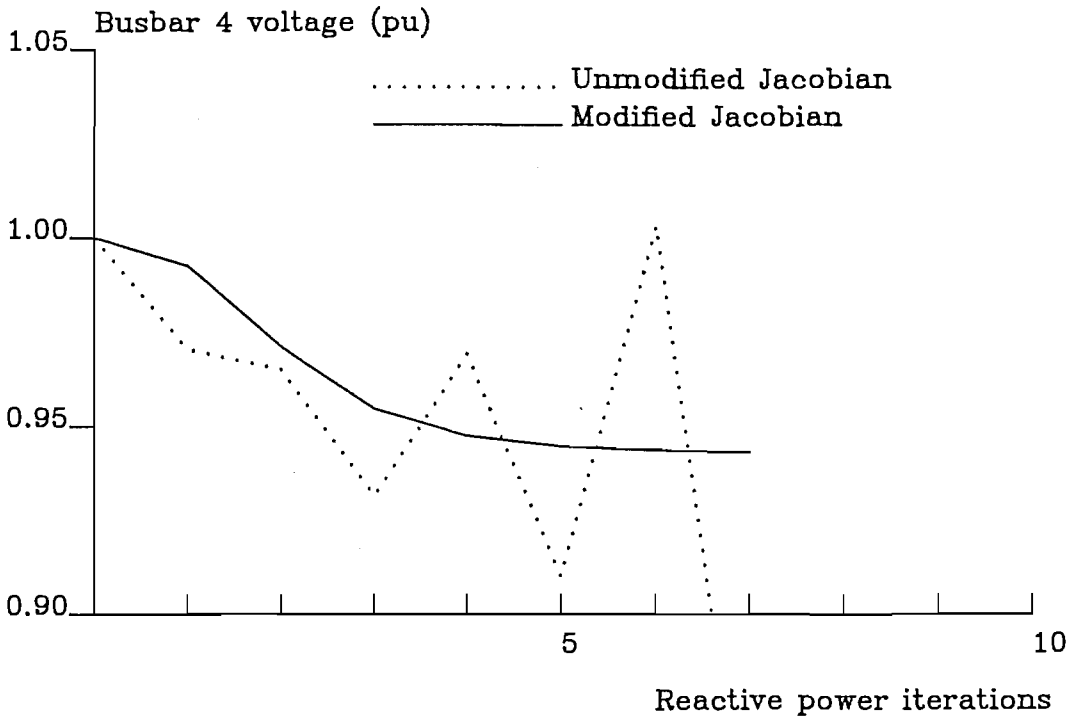

Figure 6.4(b) Powerflow Convergence for Weak AC System

If the AC system is made very weak then the improved sequential powerflow still converges to the solution whilst the conventional sequential powerflow diverges.

6.4 AC/DC SYSTEM CAPABILITY CHARTS

Figure 6.5 illustrates an example of a capability chart for an AC/DC power system. This chart portrays the range of real and reactive power that may be drawn from busbar 8 of the power system shown in figure 6.3 . The fast capability charting algorithm was used in this case.

The specified busbar load of 100 MW and 70 MVAR is represented by the star in the middle of the operating region. The four primary operating constraints that bound the operating region are

1. Minimum real power of 0 MW from the slack generator at busbar 7.
2. Minimum voltage of 0.9 pu at busbar 8.
3. Maximum current of 2 pu in the line from busbar 6 to busbar 8.
4. Minimum firing angle of 3 degrees in the rectifier at busbar 4.

The two secondary constraints that are visible are

1. Maximum reactive power output of 150 MVAR from the slack generator at busbar 7.
2. Maximum real power output of 200 MW from the slack generator at busbar 7.

Of these constraints, the one of particular interest in this chapter is the 3 degree minimum limitation on the firing angle of the rectifier at busbar 4. The presence of this constraint may be accounted for as follows.

As the reactive power consumption at busbar 8 is reduced, the voltages at busbars 5, 6, and 8 will rise. As the AC voltage at busbar 5 rises, the DC voltage at the inverter will also rise because it is operating at constant extinction angle and DC current. The rectifier at the other end of the HVDC link must then increase its DC voltage to keep the current constant. This is achieved by lowering the firing angle until the 3 degree minimum limit is reached.

The capability chart shown in figure 6.5 was also used to provide another comparison between the improved sequential AC/DC powerflow and the conventional sequential AC/DC powerflow. When the improved powerflow

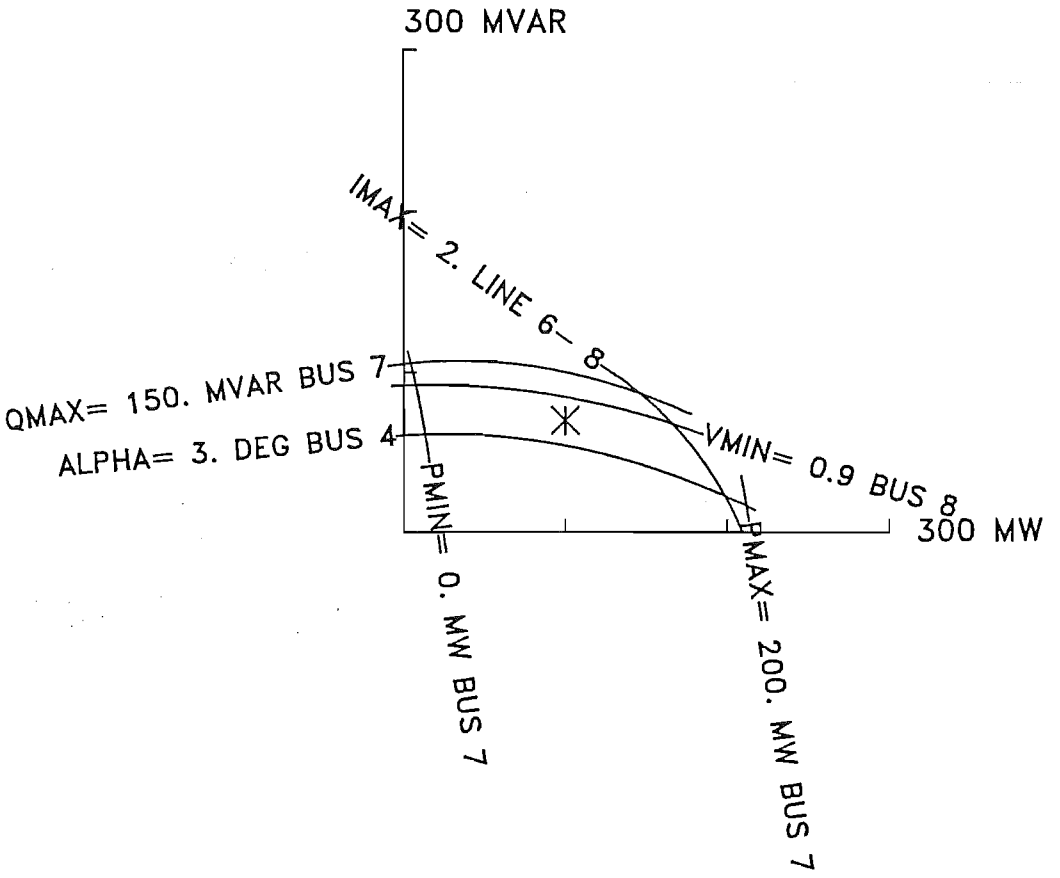

Figure 6.5 Capability Chart for Busbar 8 of AC/DC System

The star marks the specified load point within the operating region. The 'ALPHA' constraint contour represents the minimum firing angle allowable in the AC/DC converter at busbar 4.

was used, 363 real power and 346 reactive power iterations were required to draw the chart. Use of the conventional powerflow more than doubled the number of iterations required with 868 real power and 986 reactive power iterations.

Figure 6.6 illustrates a chart drawn for the simplified NZ Benmore-Haywards HVDC scheme which was described in chapter 3. This chart portrays the real and reactive power that may be delivered to the Haywards 110 kV busbar from the HVDC link whilst the Benmore generators are operating as synchronous compensators. This chart matches the chart shown in figure 3.10 (p. 55) which was constructed using the small systems approach of explicit derivation of loci equations.

The contour tracing version of the capability charting algorithm was required for this chart because the high curvature of the minimum DC holding current contour prohibited the use of the fast algorithm. The HVDC link was operated in the slack inverter mode to allow the link to reveal its full range of complex power output.

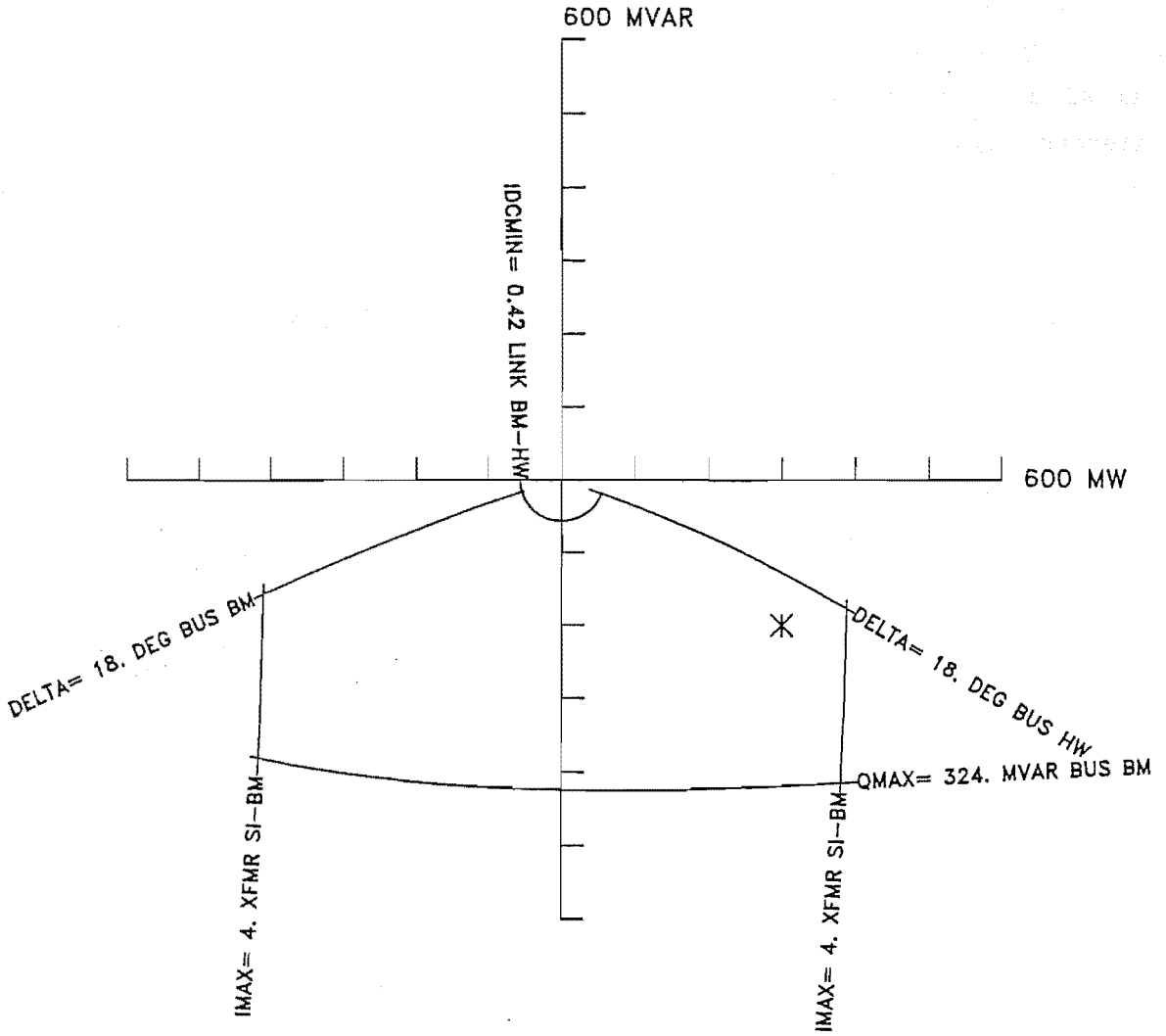

Figure 6.6 Capability Chart For The New Zealand Benmore-Haywards HVDC Scheme

This chart was drawn by the contour tracing algorithm and matches the capability chart shown in figure 3.10 (p. 55). The busbar labels are SI ; South Island 220 kV busbar

BM ; Benmore 16 kV busbar

HW ; Haywards 110 kV busbar

6.5 CONCLUSION

This chapter has described the extension of both capability charting algorithms to portray the performance of AC/DC systems, in addition to the AC systems for which the algorithms were originally designed. The extended algorithms can draw charts for power systems that include DC rectifiers and two terminal HVDC links. These DC systems can be controlled by a variety of operating strategies.

The firing angle and extinction angle constraints of the AC/DC converters require special treatment in order to ensure that the chart contours are smooth. This smoothness is necessary for the capability charting algorithms to work properly. As a consequence of the smoothing treatment, some areas of the charts outside the operating region may not represent feasible converter operating modes.

A sequential AC/DC powerflow algorithm is used to analyze the AC/DC systems. This powerflow algorithm features a simple new improvement to the conventional sequential powerflow. The improvement involves modifying the reactive power Jacobian matrix of the fast decoupled powerflow. This modification accounts for the voltage dependence of converter reactive power consumption. The improved sequential powerflow has superior convergence characteristics compared with the conventional sequential powerflow, especially in cases where the AC system is weak at the converter busbar.

Chapter 7
Planning for a Second N.Z. HVDC Link

7.1 INTRODUCTION

A proposal for a second HVDC link between the North and South Islands of New Zealand is currently being investigated by the Electricity Division of the Ministry of Energy. The new link is intended to work together with the existing link to transfer the predicted surplus of power from the hydro-electric stations in the South Island to the growing load in the North Island. This is anticipated to reduce the North Island's reliance on expensive thermal generation. The new scheme may be commissioned as early as 1991 if the need is sufficiently urgent.

The investigation is still in the early planning stages of selecting tentative sites for the HVDC link terminals.The choice of sites is dictated by the configuration of the existing AC transmission system, cost, and environmental considerations.

This chapter describes how the capability charts can be used to help judge the suitability of converter terminal sites. In this particular case, the HVDC link is envisaged to transmit 600 MW from Bendigo in the South Island to Runciman in the North Island. It is also estimated that each terminal of the link will consume about 300 MVAR of reactive power from the AC system. At this early stage no details of the actual HVDC link circuit have yet been designed, so the link is modelled by its estimated real and reactive power injections.

The fast capability charting algorithm was used to draw the charts shown in this chapter. The contour tracing algorithm can also construct the same charts but requires more CPU time.

7.2 SOUTH ISLAND TERMINAL

The 220 kV South Island primary transmission system as envisaged for 1991 is shown in figure 7.1 . The loading scenario shown on the diagram corresponds to the forecasted winter peak which is the worst case. The circuit data for this system is provided in the appendix.

The existing HVDC link is shown attached to busbar 16 (Benmore 16 kV) and the second HVDC link is shown attached to busbar 18 (Bendigo). The capacitance at busbar 18 represents the harmonic filters that will provide about 200 MVAR of reactive power to the new link.

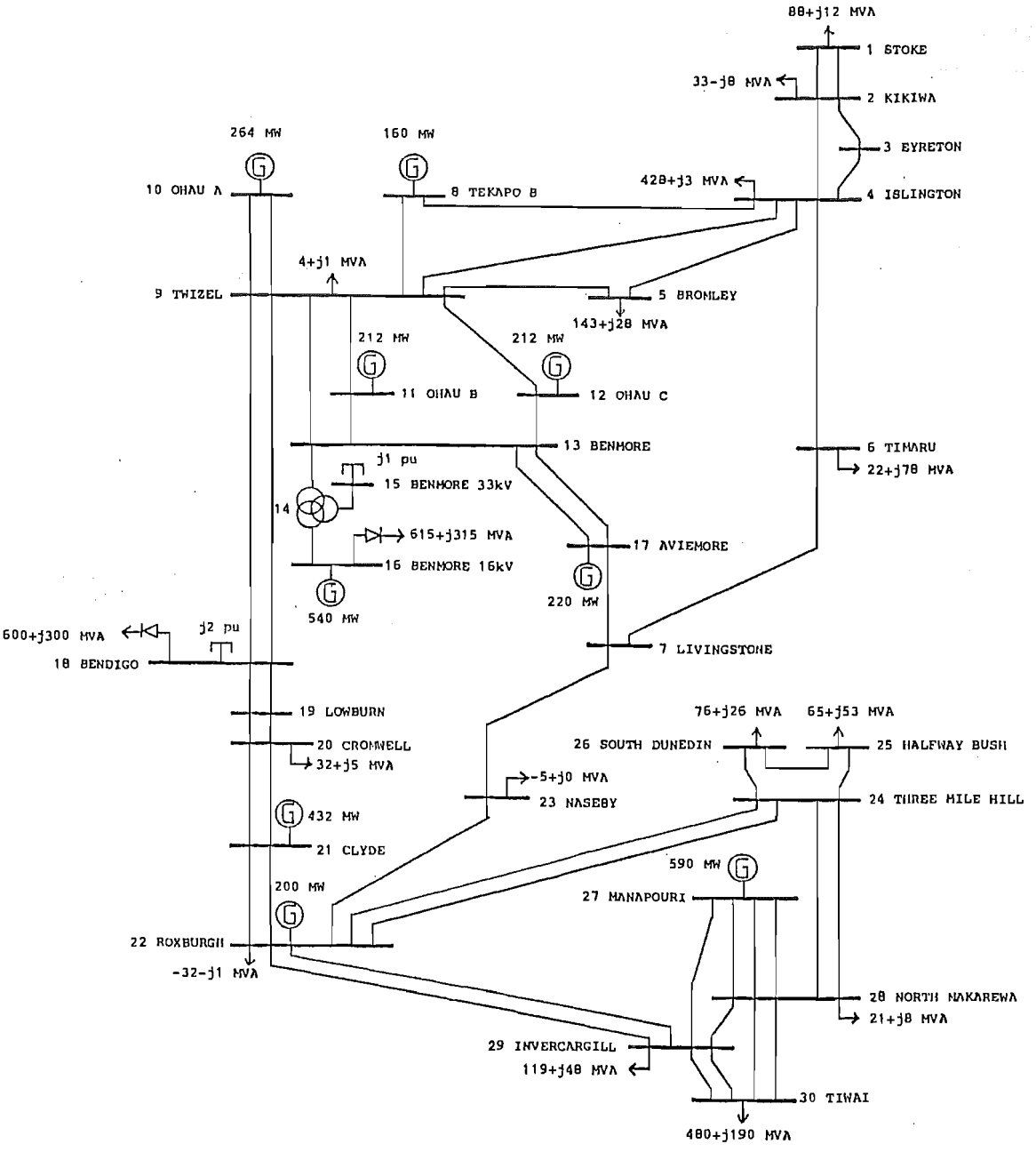

Figure 7.1 South Island 220 kV Primary Transmission System

7.2.1 Capability Chart for Bendigo Converter Busbar

The capability chart shown in figure 7.2 portrays the relationship between the complex power consumption of the second HVDC link, and the critical operating constraints of the South Island system.

The star in the operating region of the chart indicates the nominal power consumption of the AC/DC converter, which is operating in the rectifying mode. Real power consumption can be increased until slack busbar 22 (Roxburgh) is delivering maximum real power output. If the real power consumption of the rectifier is reduced then the real power from the slack busbar also drops, but the reactive power from the slack busbar will increase to its maximum limit. The presence of this reactive power limit is not intuitively obvious but is clearly shown on the chart.

The maximum reactive power consumption of the rectifier is limited by the maximum reactive power that can be supplied from busbar 21 (Clyde). Reducing the reactive power consumption results in a rise in the busbar voltages until busbars 18 (Bendigo),19 (Lowburn), and 20 (Cromwell) eventually reach their upper voltage limits. The lower reactive power limit of busbar 21 (Clyde) is a secondary constraint.

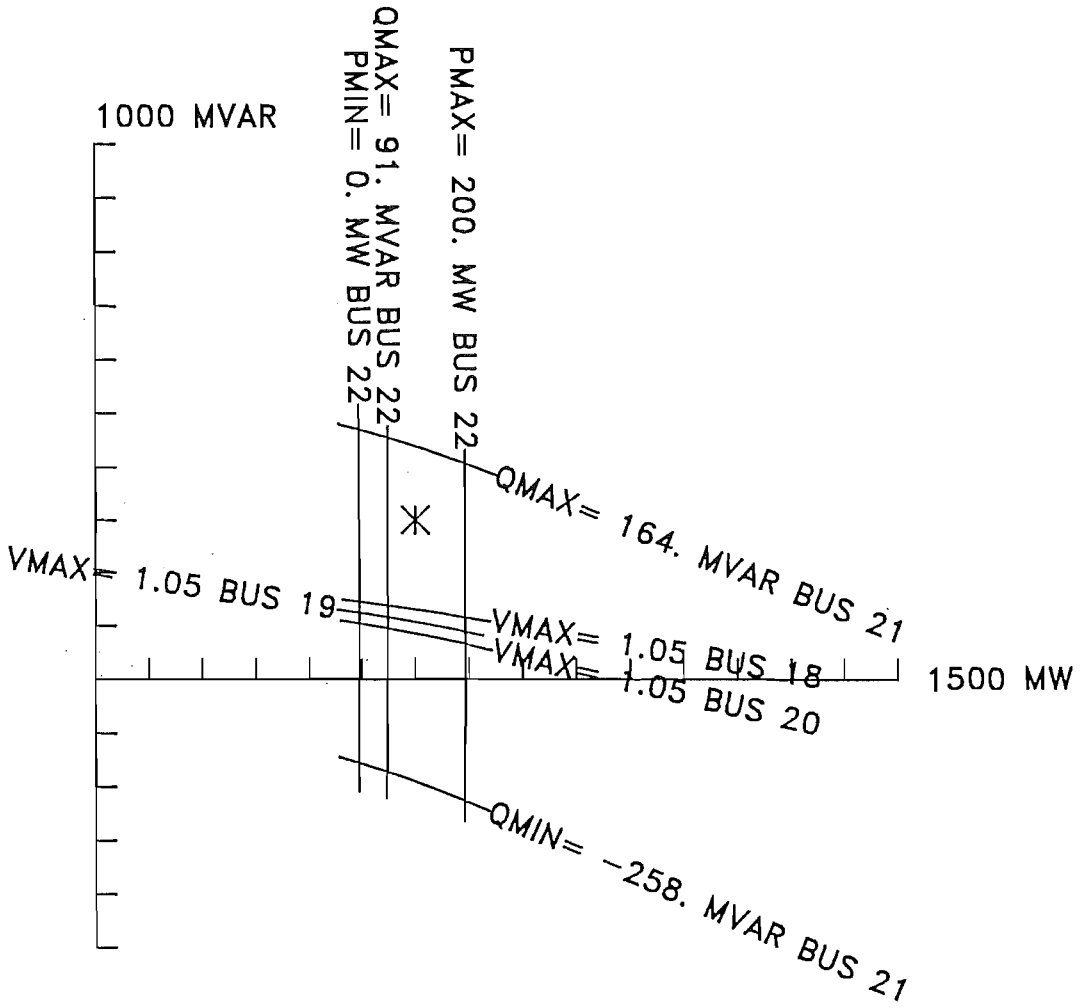

Figure 7.2 Capability Chart for Bendigo Converter Busbar

The nominal complex power consumption of the Bendigo rectifier is indicated by the star in the operating region.

7.2.2 Capability Chart for Ohau A Generator Busbar

The effect of generator control settings can also be displayed on a capability chart. Figure 7.3 shows the chart associated with busbar 10 (Ohau A). This generator busbar must be modelled as a load busbar with variable voltage and power to portray the effects of altering governor and automatic voltage regulator (AVR) settings. Since the chart displays the load power consumption, power generation appears as a negative loading. The real and reactive power limits of the Ohau A generator are approximated by the dashed rectangle that is superimposed on the chart.

The star in the operating region indicates the nominal operating point for the generator at Ohau A. The generator is delivering maximum rated power output and 13 MVAR. The lower limit of real power generation is determined by the maximum real power output of the slack generator. The maximum reactive power available from the generator at busbar 11 (Ohau B) limits the reactive power that can be consumed by the generator at Ohau A. Extra reactive power generation at Ohau A eventually results in the generator's busbar voltage reaching its upper limit. This almost coincides with the maximum reactive power output of the generator.

The good behaviour of the contours can be used to predict that altering the governor power setting at Ohau A will move the operating point in a direction parallel to the maximum voltage contour. Altering the AVR voltage setting will maintain constant real power output and move the operating parallel to the reactive power axis. This type of chart can be consulted by system operators to visually predict the effects of changing generator control settings.

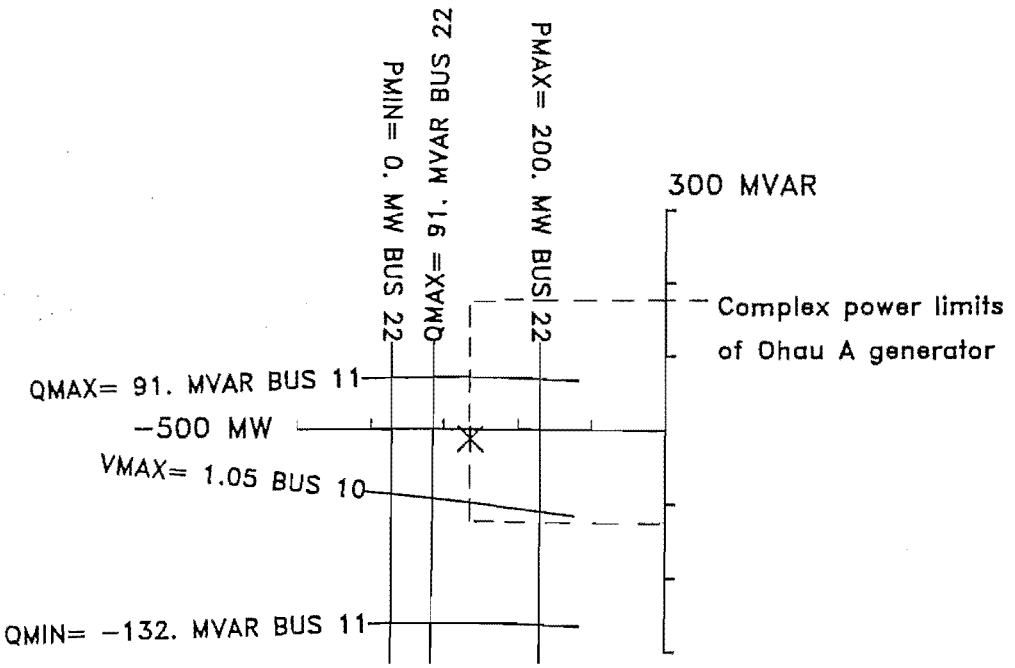

Figure 7.3 Capability Chart for Ohau A Generator Busbar

This chart can be used by system control dispatchers to predict the effect of altering generator governor and AVR settings.

7.2.3 Voltage Fluctuations at the Bendigo Converter Busbar

The ability of the fast algorithm to draw families of contours can be used to portray the slow voltage fluctuations due to gradual loading changes. In this case the voltage fluctuations that are of concern are those occurring at the Bendigo converter busbar due to changes in the power consumption of the HVDC link.

Figure 7.4 shows a contour map that represents the Bendigo AC voltage as a function of the converter power consumption. The map indicates that the worst voltage fluctuation will be approximately 0.01 pu / 70 MVA if the operating point moves perpendicularly to the voltage contours.

The HVDC link may be used in the power modulation mode to control the frequency of the North Island AC system. In this case the Runciman terminal will operate as an inverter, with a constant extinction angle, and the Bendigo terminal will operate as a rectifier, to deliver the slack real power required by the North Island.

Assuming the steady state operation of the new HVDC link will be similar to that of the existing HVDC link, the loci drawn in chapter 3 may be used to approximately predict the behaviour of the new link. If the inverter is operating in a constant extinction angle mode, then the operating point of the inverter will move along the minimum constant extinction angle locus. This locus indicates that the reactive power to real power ratio will consequently remain approximately constant at both inverter and rectifier.

Therefore the Bendigo converter's nominal complex power consumption ratio of 300 MVAR / 600 MW will be maintained as the slack power delivery changes, hence the operating point will move along the locus shown by the dashed line that is superimposed on the contour map. The voltage fluctuation that is associated with the slack power variation is obtained by inspecting the locus crossing the contours. This indicates that the voltage will change by approximately 0.01 pu / 110 MW of slack power variation.

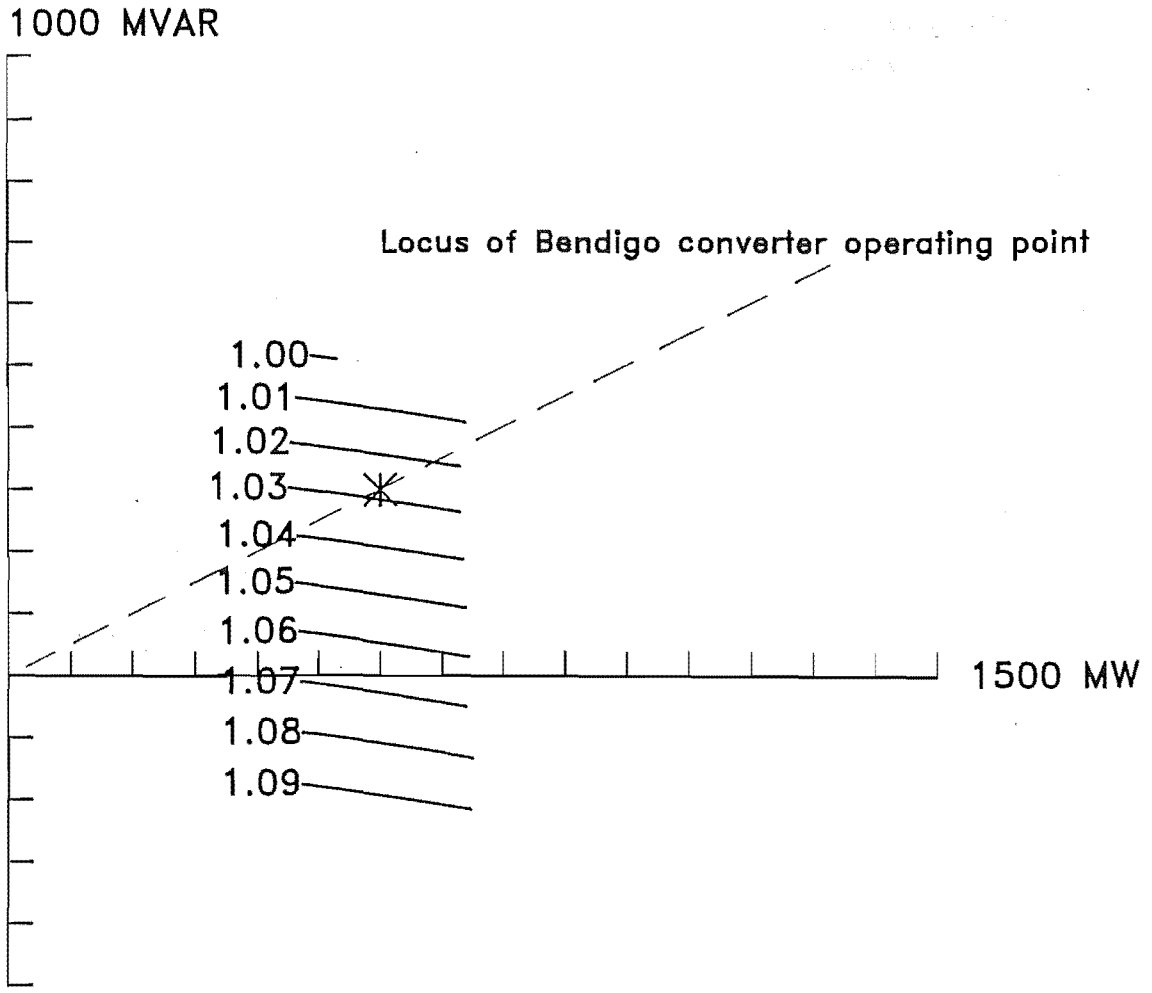

Figure 7.4 Voltage Contour Map for Bendigo Converter Busbar

This map shows the AC voltage fluctuations associated with changes in the converter operating point.

7.3 NORTH ISLAND TERMINAL

The North Island converter terminal of the second HVDC link is shown attached to busbar 47 (Runciman) in the circuit diagram shown in figure 7.5 . This diagram represents the 220 kV primary transmission system that is envisaged for the upper North Island during the 1991 winter peak load. The circuit data for this system is provided in the appendix.

The lower North Island system, which includes the existing HVDC link, has only a small effect on the steady state operation of the Runciman converter. This is because the power from the lower North Island is funnelled Northward through slack busbar 52 (Whakamaru), which tends to decouple the upper and lower systems. Therefore the lower North Island is not considered in detail but is modelled by a constant negative load attached to the slack busbar.

The capacitance at the Runciman converter busbar represents the harmonic filters that provide the full 300 MVAR reactive power requirement of the converter.

The generators at busbar 40 (Otahuhu North 110 kV) and busbar 44 (Otahuhu South 110 kV) are acting as synchronous compensators because their gas turbine generation has been replaced by the cheaper hydro-electric power delivered by the HVDC link.

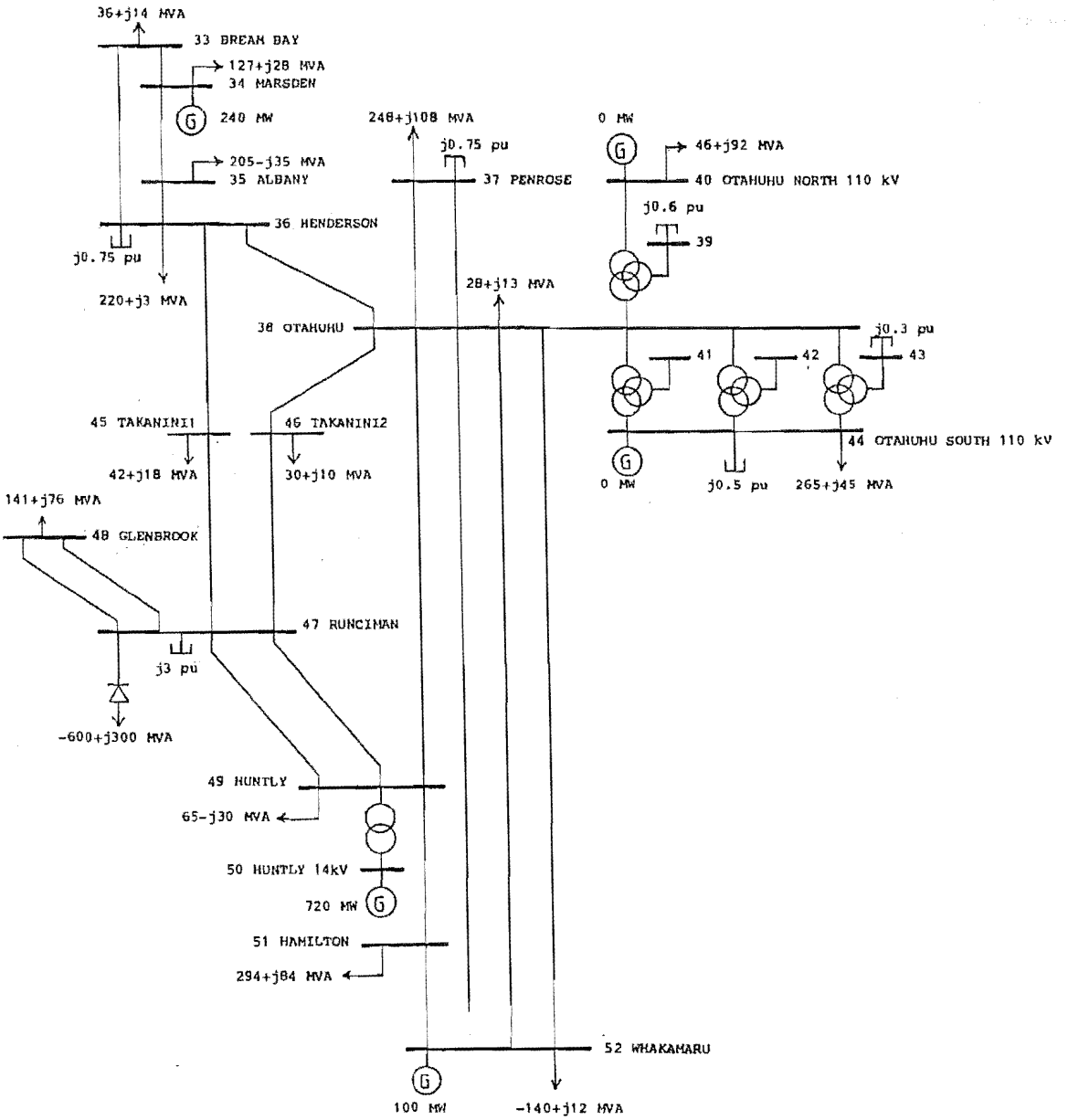

Figure 7.5 Upper North Island 220 kV Primary Transmission System

7.3.1 Capability Chart for Runciman Converter Busbar

The capability chart shown in figure 7.6 portrays the relationship between the nominal operating point of the Runciman converter and the most critical constraints of the upper North Island power system.

The real power delivered by the HVDC link is restricted by the real power output limitations of the slack generator at busbar 52 (Whakamaru). The maximum reactive power output of this generator also defines the maximum allowable reactive power consumption of the converter terminal.

The close reactive power relationship between the converter and the slack generator can be attributed to the strong interconnection provided by the four transmission lines linking the slack generator and busbar 38 (Otahuhu). These lines bring the slack generator electrically close to the converter terminal at busbar 47 (Runciman).

The lower limitation on the reactive power consumed by the converter is imposed by the maximum reactive power consumption of the generator at busbar 40 (Otahuhu North 110 kV) which is acting as a synchronous compensator. A low reactive power consumption at the converter will also result in high voltages at busbar 49 (Huntly) and busbar 35 (Albany).

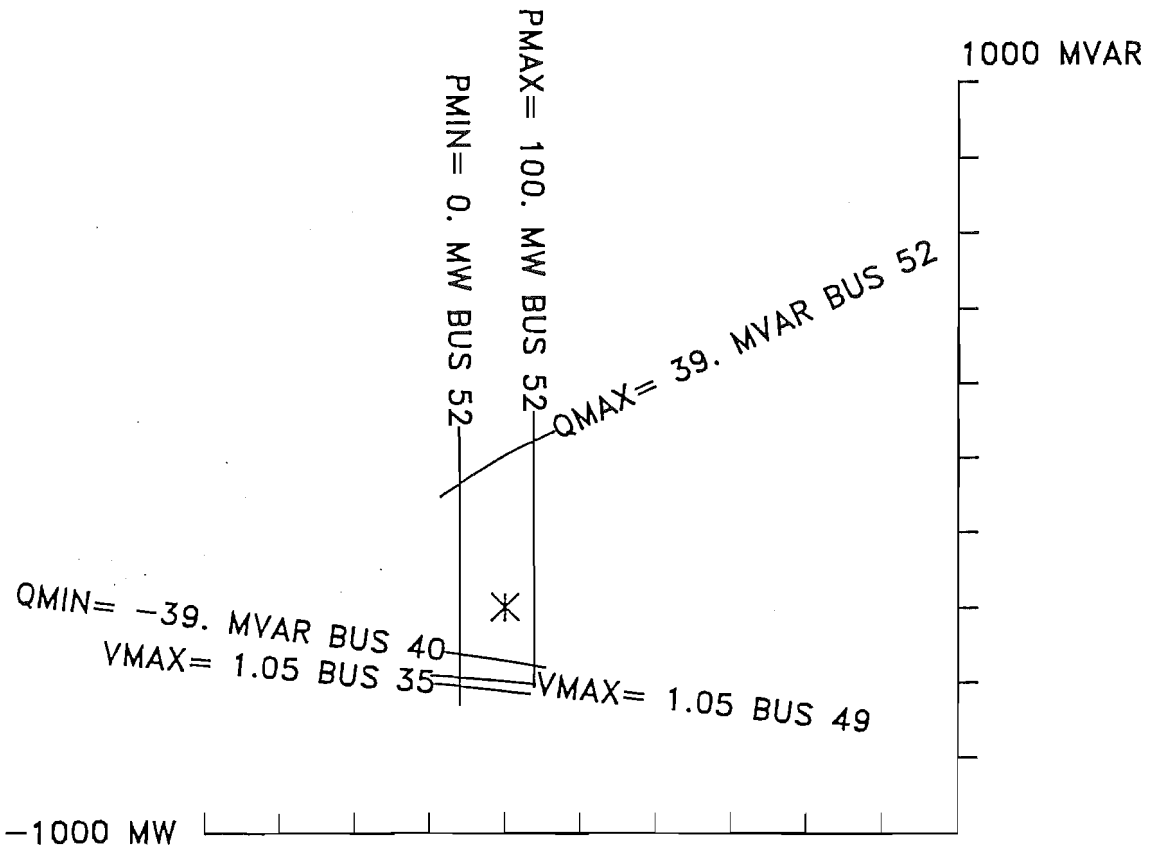

Figure 7.6 Capability Chart for Runciman Terminal Busbar

The real power delivery and reactive power consumption of the Runciman inverter is indicated by the star in the operating region.

7.3.2 Capability Chart for Huntly Generator Busbar

To study the effect of generator governor and AVR settings in the North Island, generator busbar charts can be drawn similarly to the South Island's Ohau A generator capability chart discussed in section 7.2.2 .

Figure 7.7 shows the effect of changing the real and reactive power output of the generator at busbar 50 (Huntly 14 kV). In this case the restrictions on the power output of the generator lie entirely within the dashed rectangle that approximates the total complex power available from the generator.

The Huntly generator busbar is electrically very close to the converter terminal at Runciman, consequently the operating constraints depicted on the Runciman chart in figure 7.6 are repeated on the Huntly generator chart in figure 7.7.

Whilst the types of constraint shown on the two charts are identical, the spatial relationship between the constraint contours is slightly different. In particular, the minimum reactive power limit of the generator at busbar 40 (Otahuhu North 110 kV) is a primary constraint on the Runciman chart and the maximum voltage limit of busbar 49 (Huntly) is a secondary constraint. The priorities of these two constraints are reversed on the Huntly generator chart.

In general, the electrical proximity of any two busbars tends to be reflected in the similarity of their capability charts.

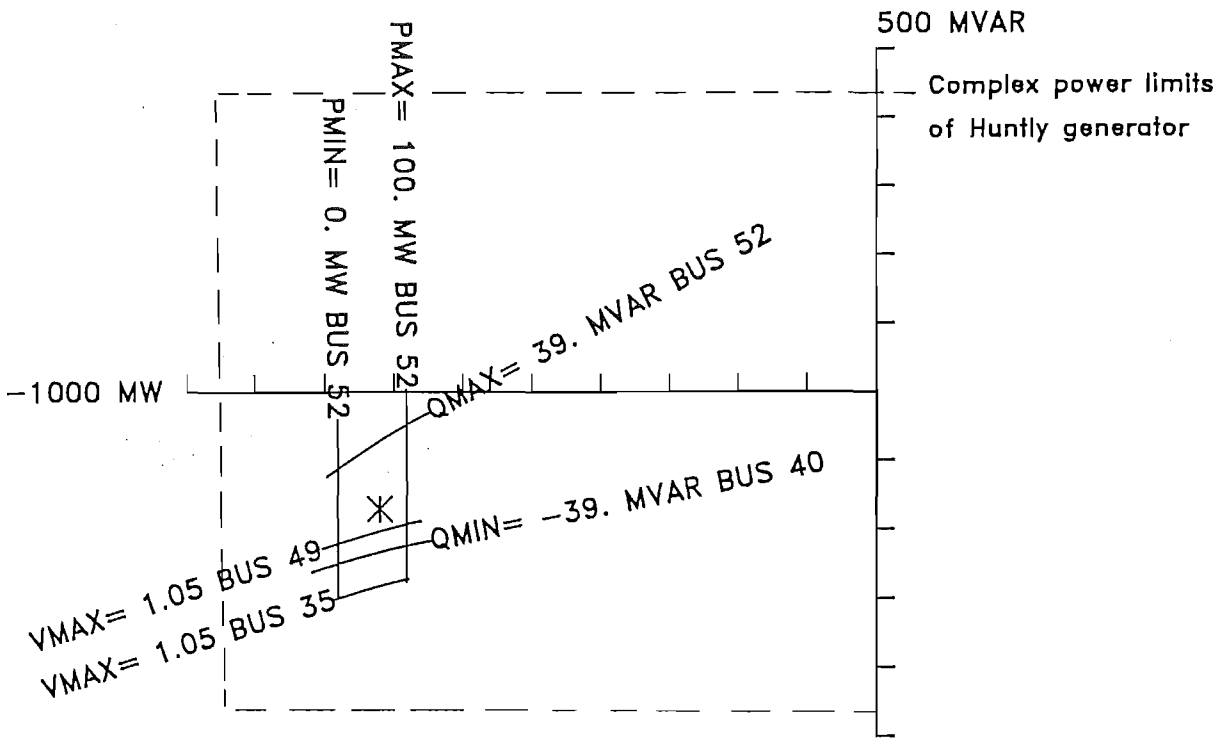

Figure 7.7 Capability Chart for Huntly Generator Busbar

This chart is similar to the Runciman terminal chart shown in figure 7.6 because of the electrical proximity of the Huntly generator busbar to the Runciman busbar.

7.4 CONCLUSION

This chapter has demonstrated the applicability of capability charts to assist in the planning for a second New Zealand HVDC link. In the scenario that was envisaged, the new link transferred 600 MW from Bendigo in the South Island to Runciman in the upper North Island.

The capability charts have identified the AC system operating constraints on the complex power consumption of the two HVDC link converter terminals. The charts associated with generator busbars may be used by system control dispatchers to predict the effects of altering governor and AVR settings.

In addition to the capability charts, a voltage contour map has also proven to be useful in the study of AC voltage fluctuations that arise from using the HVDC link in a power modulation mode.

These practical examples of the use of capability charts are a favourable indication that the charting algorithms will prove to be a useful planning tool in the future.

Chapter 8
Proposed Developments

8.1 INTRODUCTION

This thesis has extended the concept of the synchronous generator capability chart to display the performance of large power systems. The work that has been described is a preliminary investigation so the true utility of the new charts still needs to be confirmed by more extensive use in practical situations. The traditional synchronous generator capability chart eventually became a proven tool and at this introductory stage the new charts also seem to hold great promise.

While the algorithms described in this thesis were being developed, several other improvements and variations could be only briefly considered in the time available. These extra aspects are presented in this chapter as proposals for future development.

8.2 MORE DETAILED MODELS

The number of different types of operating constraint that are portrayed on the capability charts is determined by the model used to represent the power system. A greater variety of operating constraints could be incorporated into the charts by modelling the power system in more detail. This would entail a more elaborate powerflow algorithm, but the capability charting techniques should essentially remain unaltered.

One suggested improvement is the detailed modelling of transmission lines to allow the calculation of the true maximum voltage and current along the line (Shultz and Smith, 1986). At present these constraints are dealt with by assuming that the maxima occur at one of the ends of the line (section 2.3.2). This assumption is only valid for short lines, hence long lines must be represented by a series of concatenated short lines. This concatenation could be avoided if the true voltage and current maxima were evaluated.

Another suggested improvement is the detailed modelling of synchronous generators. The generators in large systems are presently modelled as constant voltage magnitude, constant power sources, apart from the slack generator which is modelled as a constant voltage magnitude, constant voltage angle source. The complex power output limits of each generator are represented by a simple rectangular capability chart. The sides of the rectangle denote the approximate real and reactive power limits.

This rectangular approximation can be replaced with a more accurate chart by using a more detailed generator model. A detailed model would allow all of the constraints shown in the traditional synchronous generator capability chart to be added to the charts for large power systems.

At present the real power slack generation function is confined to one busbar. A more realistic power system model could be represented by distributing this slack generation over several generator busbars.

8.3 GENERATION COST CONTOURS

The capability chart for a generator busbar portrays the constraints on the real and reactive power production of the generator. The power generation authority seeks to operate within all of the constraints, whilst simultaneously seeking to minimise the overall cost of generation.

Both objectives may be achieved by superimposing a generation cost contour map over the capability chart for the generator busbar. The map would represent the overall generation cost for the entire power system.

The operating point of the generator could then be positioned at the point within the operating region which corresponds to the minimum overall generation cost.

It may be possible to use this graphical technique to improve upon the estimated optimal operating point suggested by existing economic power dispatch algorithms.

8.4 OPTIMAL POWERFLOW ALGORITHMS

The present capability charts are limited to displaying the operating regions corresponding to a fixed scenario of governor power settings and AVR voltage settings. If these generator controls are given the freedom to be altered then a larger operating region is feasible. The powerflow algorithm that is used to alter the generator controls must ensure that all of the system operating limits are respected as the controls are adjusted.

An optimal powerflow algorithm similar to those reviewed by Carpentier (1979) would be suitable for this task. The optimal powerflows seek to optimize an objective function by adjusting the generator control settings. These powerflows are usually used to either minimise transmission losses or to minimise power generation cost.

In order to construct a capability chart with the largest possible operating region, the optimal powerflow would be required to minimise the violation index by adjusting generator control settings. This will produce an expanded operating region that will be a superset of the fixed scenario operating region.

8.5 STOCHASTIC POWERFLOW ALGORITHMS

The capability charting programs rely on a powerflow algorithm to solve the system equations associated with each point on the chart. The existing programs use the fast decoupled powerflow described by Stott and Alsac (1974). This is a deterministic powerflow that provides an exact solution, given precisely defined system loading conditions.

When the busbar loads are not precisely known, then an approximate load value must be assumed by the deterministic powerflow. Consequently the powerflow solutions, and the capability charts derived from the powerflow solutions, can only be regarded as approximate results.

Various stochastic powerflow algorithms have been designed to deal with the unpredictable variation in busbar loads (Dopazo et al., 1975 and Allan et al., 1981). The simpler stochastic powerflows model the load

variation as a Gaussian distribution. More sophisticated algorithms are able to cope with any arbitrary random load distribution. The stochastic powerflow solutions are also presented in the form of random distributions. For example the voltage magnitude at a busbar may be presented as the mean and standard deviation of a Gaussian distribution.

If the capability chart is to be used for planning purposes, where future busbar loading can be only roughly estimated, then it would be appropriate to replace the existing deterministic powerflow with a stochastic powerflow. The charting algorithm would also have to be modified to portray effects of the randomly distributed solutions from the stochastic powerflow.

One possible method of portrayal is shown in figure 8.1 . The narrow filaments of the deterministic contours have been replaced by wider bands that represent the possible variation of contour position due to the uncertainty in busbar loading. For example there may be 95 % confidence that the actual contour will lie within the band. As the uncertainty in the busbar loading increases then the bands can be expected to widen.

8.6 EIGENVALUE REPRESENTATION

The present criteria used by the charts for determining the steady state stability of the power system are the voltage phase angle differences across branches and the phase angle differences between the slack busbar and the other generating busbars. These two criteria are rather crude rules of thumb chosen for their simplicity and ease of calculation.

If a better steady state stability criterion is desired then an eigenvalue analysis is suggested. Power system eigenvalue studies consider the damping behaviour of the entire system and require detailed modelling of governor and AVR control loops.

There are a fixed number of eigenvalues associated with any given system configuration. Each eigenvalue is a complex number that represents the damping of a characteristic system oscillation. Stable, positively damped oscillations are represented by eigenvalues with negative real

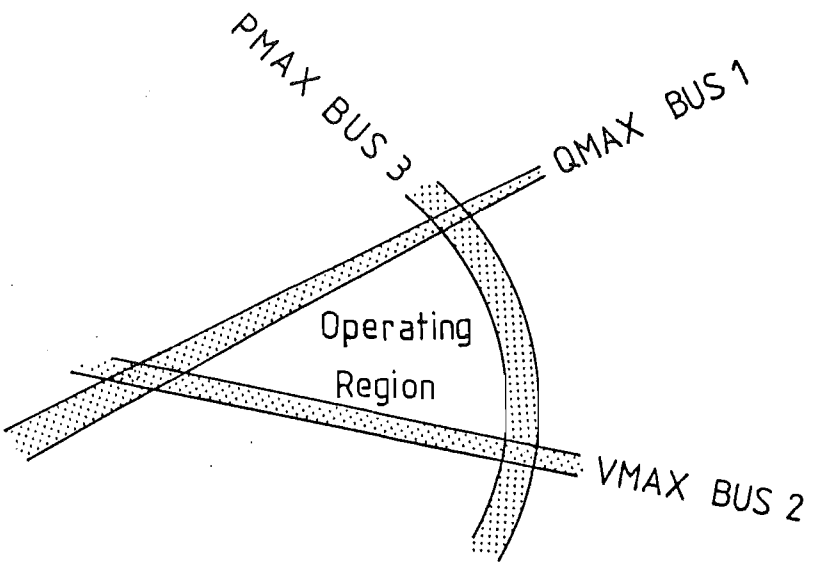

Figure 8.1 Anticipated Stochastic Capability Chart

If the loading at the busbars is randomly distributed then the possible variation in constraint contours could be represented by wide bands.

parts. Unstable, negatively damped oscillations are represented by eigenvalues with positive real parts. The complex parts of each eigenvalue represent the frequency of the oscillation.

The electromagnetic oscillations are usually well damped but the electromechanical oscillations frequently prove troublesome. A system with n generators will typically exhibit n-1 dominant electromechanical natural frequencies of the order of 1 Hz. These are characterised by the large oscillating power swings observed on badly damped systems.

The variation in the real damping term of each eigenvalue has been represented by contour maps on the complex power plane by Wirth et al. (1983). To incorporate this into a capability chart, one particular damping contour from each map could be chosen to represent an upper desirable limit on each eigenvalue damping term. Operation within all of the bounds of the damping contours would ensure steady state stability.

A considerable amount of extra computation will be required for the repeated evaluation of eigenvalues at different points on the chart, especially for large systems. However the eigenvalue stability criteria that is obtained will be much more accurate than the present crude estimates of stability.

8.7 INTERACTIVE GRAPHICS PROGRAMS

The capability charts would make suitable additions to existing power system interactive graphics programs such as IPSA (Lynch and Efthymiadis, 1979) or ADAPOS (Fujiwara and Kohno, 1985). These programs provide an interactive graphical interface to a collection of useful power system analysis algorithms which will perform powerflows, short circuit studies, and transient stability simulations. The graphical interface allows the user to draw a circuit diagram on the display screen and to observe the analysis results superimposed on the diagram.

Incorporating the capability charts into the interactive graphics programs would make the charts easier to use and would also enhance the graphics programs themselves.

If a capability charting algorithm is incorporated into one of these power system graphics programs, then some modifications will be necessary to properly match the two programs. For consistent and efficient program structuring the charting algorithm should make use of the powerflow, graphics routines, and databases that already exist in the graphics program. The charting algorithm should also be able to cope with all of the operating limits associated with devices that are represented in the graphics program.

8.8 SYSTEM CONTROL APPLICATIONS

On-line capability charts situated in a system control centre would usefully assist dispatchers to monitor the power system. Existing alarms in system control centres can already indicate the proximity of operating limits. The capability charts would simplify the dispatcher's job by emphasizing the most critical limits and, more importantly, portraying the relationship between limits,loading, and cost of generation.

The block diagram in figure 8.2 shows an anticipated plan for incorporating the capability chart into the organisation of a system control centre. The power system is controlled and monitored via a system control and data acquisition network (SCADA). The information from the SCADA network is fed to a state estimator which uses the available measured data to estimate other unmeasured system parameters. The complete set of information about the power system is then presented to the dispatchers on a variety of displays.

At present the displays consist of either tabulated data or circuit diagrams on VDU's. The dispatchers can consult these displays and then control the power system via the SCADA network. Graphics terminals displaying capability charts could be appropriately sited alongside the present displays.

The information required by the capability charting algorithm can be provided by the state estimator that already services the existing displays.

Each chart would have to be periodically updated because the shape of the contours will vary as the system operating conditions change. True real time chart displays will not be needed because the charts only represent the steady state operation of the power system. A time interval of 10 to 20 seconds between updates should therefore be adequate.

The time required to update a chart will depend on the following factors;

1. Size of the power system.
2. Number of operating constraints.
3. Size of the vicinity of the operating region being displayed.
4. Accuracy of the contour plotting algorithm.
5. Speed of the computer.
6. Speed of the graphics plotting facilities.

To avoid burdening the dispatchers with unnecessary information, only a few useful charts should be displayed at any one time. The charts that indicate an operating point well within the operating region will be less useful than charts showing operating points bordering on the edge of the operating region.

Cosmetic modifications to the algorithm will be vital to ensure that an ergonomic display is presented to the dispatchers. The use of colour and the style of contour labels will have to be carefully considered. The recommendations for power system monitoring displays by Wise and Abi-Samra (1986) should be helpful.

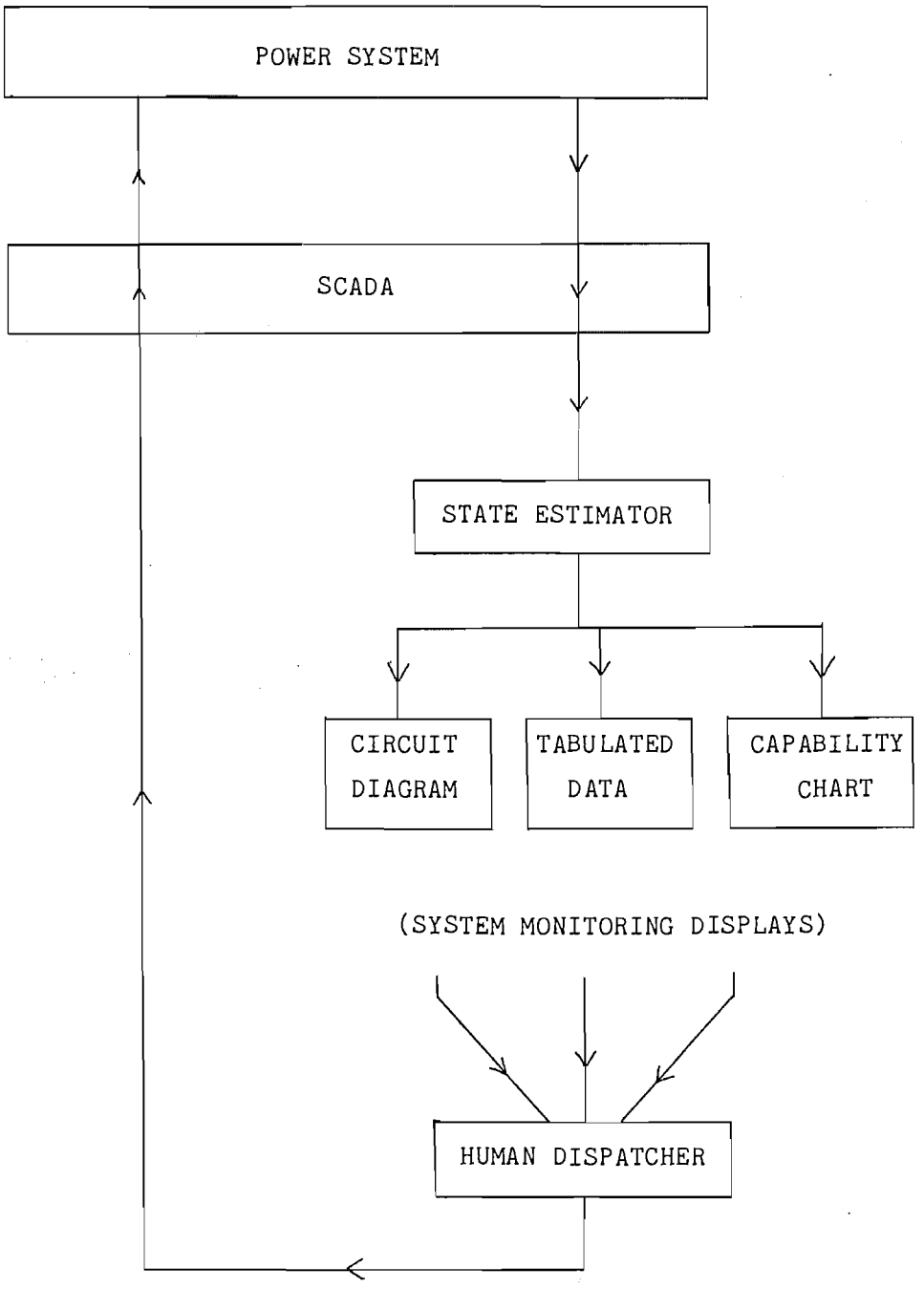

Figure 8.2 Capability Charts for System Control

A capability chart could be appropriately presented alongside the other system monitoring displays. The information required for the chart can be supplied by existing equipment.

8.9 CONCLUSION

Several proposals for the future development of the capability charts have been discussed in this chapter.

If the power system was modelled in greater detail then a greater variety of operating limits could be represented on the charts.

A combination of a total generation cost contour map with a capability chart for a generator busbar would assist power generation authorities to minimize generation costs.

Different types of powerflow could be used to produce different styles of chart. The present charts are produced using a deterministic powerflow. A stochastic powerflow could be used instead to display the uncertainty in contour positions due to the uncertainty in busbar loading. An optimal powerflow could be used to demonstrate the larger operating region that is feasible if generator control settings are not fixed to a particular scenario.

The present crude criteria for steady state stability could be replaced by using a more sophisticated eigenvalue analysis. Critical eigenvalue damping terms would be represented by contours on the chart.

The charts would make suitable additions to existing power system interactive graphics programs as well as to the visual displays in system control centres.

Chapter 9
Main Conclusions

This thesis has extended the concept of the traditional synchronous generator capability chart to describe the steady state performance of transmission lines, HVDC links, and entire AC/DC power systems.

The capability charts are drawn on the complex power plane. Each chart depicts an operating region that represents the real and reactive power that may be supplied to a load from a particular busbar. The boundaries of the operating region are defined by a web of contours that represent the critical operating constraints of the system.

The new capability charts that have been introduced in this thesis will help engineers to gain a better appreciation of power system operation.

The charts for small systems, with specific circuit configurations, can be constructed by manipulating the operating equations into a form suitable for drawing loci on the complex power plane. This technique is used in this thesis to construct charts for generators, transmission lines, and HVDC links.

The operating equations of larger, more general, power systems cannot be easily manipulated, so a different approach is used to construct the charts for large systems. This approach involves using iterative powerflows and contour plotting to avoid the formulation of explicit closed form locus equations.

Voltage contour maps previously presented by Price (1984) had indicated that the contours for large systems could be badly behaved with many twists and loops. The first capability charting algorithm was therefore designed to cope with the expected bad behaviour by gradually tracing the path of each constraint contour. The contour tracing was restricted to the vicinity of the operating region in order to avoid unrealistic operating states.

Contrary to initial expectations, the charts drawn by the contour tracing algorithm demonstrated that the constraint contours for large systems are usually very well behaved in the vicinity of the operating region.

The good contour behaviour is exploited in a fast capability charting algorithm. The fast algorithm uses a region growing procedure to construct a lattice of powerflow sample points over the vicinity of the operating region. Linear interpolation between the lattice points is then used to plot each constraint contour. The fast algorithm draws capability charts about four times faster than the first capability charting algorithm which used the contour tracing approach.

The fast algorithm is not suitable for contours that have a high curvature. The slower contour tracing algorithm is more appropriate in these cases.

Discontinuities in contours cannot be tolerated by the capability charting algorithms. The operating equations of AC/DC converters are particularly prone to discontinuities and therefore require special treatment. The converters are modelled in an intentionally unrealistic manner outside the operating region in order to retain the smoothness of contours. The modelling of the operating region itself still remains quite realistic.

The capability charting algorithms use a sequential AC/DC powerflow to analyze the AC/DC systems. The convergence of the powerflow is improved by modifying the reactive power Jacobian matrix of the fast decoupled AC iteration to account for the voltage dependent reactive power consumption of AC/DC converter terminals.

Capability charts associated with a proposed second New Zealand HVDC link have shown how the charts can be used for practical planning purposes.

The algorithms for drawing the charts would make appropriate additions to existing power system interactive graphics programs. This would allow the charts to be used more easily, and would also enhance the interactive graphics programs themselves.

The charts are also suitable for visual display in system control centres, alongside existing displays of circuit diagrams. The on-line information from the charts would simplify the task of human dispatchers by portraying the relationship between critical operating limits and busbar loading.

References

Allan, R.N., Leite da Silva, A.M., and Burchett, R.C. (1981), "Evaluation Methods and Accuracy on Probabilistic Load Flow Solutions", IEEE Trans. on Power Apparatus and Systems, PAS-100, pp. 2539-2546.

Arnold, C.P., and de Silva, J.R. (1986), "A Capability Chart for Power Systems", Second International Conference on Power System Monitoring and Control, Durham, UK.

Arrillaga, J. (1983), "High Voltage Direct Current Transmission", IEE, Peter Peregrinus.

Arrillaga, J., Arnold, C.P., and Harker, B.J. (1983), "Computer Modelling of Electrical Power Systems", John Wiley and Sons.

Ballard, D.H. and Brown, C.M. (1982), "Computer Vision", Prentice Hall.

Beebe, N.H.F. (1979), "A User's Guide To PLOT79", University of Utah.

Carpentier, J.W. (1979), "Optimal Power Flows", Electrical Power and Energy Systems, vol. 1., no. 1, pp. 3-15.

de Silva, J.R., and Arnold, C.P. (1987), "A Simple Improvement To Sequential AC/DC Powerflow Algorithms", submitted to the Electric Energy Systems Journal.

de Silva, J.R., Arnold, C.P., and Arrillaga, J. (1987), "A Capability Chart for an HVDC Link", accepted for publication in the IEE Proceedings-C Generation, Transmission, and Distribution.

Dopazo, J.F., Klitin, O.A., and Sasson, A.M. (1975), "Stochastic Load Flow", IEEE Trans. on Power Apparatus and Systems, PAS-94, pp.299-309.

Dwight, H.B. (1922), "Electrical Characteristics of Transmission Systems", Trans. AIEE 41, pp. 781-784.

Evans, R.D., and Sels, H.K. (1921), "Circle Diagrams for Transmission Systems", Electric Journal, vol. 18, pp.530-536.

Fujiwara, R., and Kohno, Y. (1985), "User-friendly Workstation for Power System Analysis", IEEE Trans. on Power Apparatus and Systems, PAS-104, no. 6, pp. 1370-1376.

Kimbark, E.W. (1971),"Direct Current Transmission, Vol. 1", Wiley-Interscience, New York.

Lynch, C.A., and Efthymiadis, A.E. (1979), "Network Graphics Based Interactive Power System Analysis", IEEE Winter Power Meeting.

Philip, R.A. (1911),"Economic Limitations to Aggregation of Power Systems", Trans. AIEE 30 (pt. 1), pp. 597-636.

Price, G.B. (1984), "A Generalized Circle Diagram Approach for Global Analysis of Transmission System Performance", IEEE Trans. on Power Apparatus and Systems, PAS vol. PAS-103, no. 10, pp. 2881-2890.

Shultz, R.D., and Smith, R.A. (1985), "Calculation of Maximum Effective Current on Transmission Lines Including All Harmonics Present", Electrical Power and Energy Systems, vol. 8, no. 2., pp.115-119.

Steinmetz, C.P. (1916), "Theory and Calculation of Alternating Current Phenomena", McGraw-Hill.

Stott, B. and Alsac, O. (1974), "Fast Decoupled Loadflow", IEEE Trans. on Power Apparatus and Systems, PAS-93, pp. 859-869.

Szwander, W. (1944), "Fundamental Electrical Characteristics of Synchronous Turbo-generators", Journal IEE, 91, pt. 2, pp. 185-194.

Venikov, V.A., and Rozonov, M.N. (1961), "The Stability of a Load", Izv. Akad. Nauk SSSR (Energetika i Artomatica), 3, pp. 121-125, (Russian).

Walker J.H. (1953), "Operating Characteristics of Salient-pole Machines", Proc IEE, 100, pt. 2, pp. 13-24.

Weedy, B.M. (1968),"Voltage Stability of Radial Power Links", Proc IEE, vol. 115, no. 4, pp. 528-536.

Wirth, E., Bertschi, R., and Castelli, G. (1983), "Determining and Optimizing the Static Stability of Synchronous Generators in Electrical Power Systems", Brown Boveri Rev. 70 (1/2), pp. 13-17.

Wise, J.A. and Abi-Samra, N.C. (1986), "The Design of Display Systems for Electrical Control Centres", IEE Second International Conference on Power System Monitoring and Control, Durham, UK.

Appendix
Circuit Data

A1 IEEE 14 BUSBAR TEST SYSTEM

The operating constraints that are given here have been adopted for demonstration purposes in this thesis.

Power base = 100 MVA

BUSBAR DATA
Type S=Slack, G=Generator, L=Load

Busbar name	Type	Voltage	Load		Generation		
	(SGL)	(pu)	MW	MVAR	MW	MVAR (min)	MVAR (max)
1 SLACK	S	1.060			0. to 300.	-200.	200.
2 GENER	G	1.045	21.7	12.7	40.	-40.	50.
3 SYNCO	G	1.010	94.2	19.0	0.	0.	40.
4 LOAD	L		47.8	-3.9			
5 LOAD	L		7.6	1.6			
6 SYNCO	G	1.070	11.2	7.5	0.	-6.	24.
7 XFMR	L						
8 SYNCO	G	1.090			0.	-6.	24.
9 CAPAC	L		29.5	16.6			
10 LOAD	L		9.0	5.8			
11 LOAD	L		3.5	1.8			
12 LOAD	L		6.1	1.6			
13 LOAD	L		13.5	5.8			
14 LOAD	L		14.9	5.0			

IEEE 14 BUSBAR TEST SYSTEM (continued)

TRANSMISSION LINE DATA

Busbar1	Busbar2	RL (pu)	XL (pu)	BL (pu)	Maximum Current (pu)
1 SLACK	2 GENER	0.01938	0.05917	0.0528	1.6
1 SLACK	5 LOAD	0.05403	0.22304	0.0492	1.6
2 GENER	3 SYNCO	0.04699	0.19797	0.0438	1.6
2 GENER	4 LOAD	0.05811	0.17632	0.0374	1.6
2 GENER	5 LOAD	0.05695	0.17388	0.0340	1.6
3 SYNCO	4 LOAD	0.06701	0.17103	0.0346	1.6
4 LOAD	5 LOAD	0.01335	0.04211	0.0128	1.6
6 SYNCO	11 LOAD	0.09498	0.19890		0.8
6 SYNCO	12 LOAD	0.12291	0.25581		0.8
6 SYNCO	13 LOAD	0.06615	0.13027		0.8
9 CAPAC	10 LOAD	0.03181	0.08450		0.8
9 CAPAC	14 LOAD	0.12711	0.27038		0.8
10 LOAD	11 LOAD	0.08205	0.19207		0.8
12 LOAD	13 LOAD	0.22092	0.19988		0.8
13 LOAD	14 LOAD	0.17093	0.34802		0.8

TRANSFORMER DATA

Busbar1	Busbar2	RL (pu)	XL (pu)	Tap ratio Bus1:Bus2	Maximum Current (pu)
5 LOAD	6 SYNCO		0.25202	0.932	1.0
4 LOAD	9 CAPAC		0.55618	0.969	1.0
8 SYNCO	7 XFMR		0.17615	1.000	1.0
9 CAPAC	7 XFMR		0.11001	1.000	1.0
4 LOAD	7 XFMR		0.20912	0.978	1.0

SHUNT CAPACITOR DATA

Busbar	Susceptance (pu)
9 CAPAC	0.19

IEEE 14 BUSBAR TEST SYSTEM (continued)

BUSBAR VOLTAGE RATINGS

Busbar 7 XFMR	0.	to 2.	(pu)
All other busbars	0.85	to 1.15	(pu)

MAXIMUM GENERATOR BUSBAR VOLTAGE ANGLE DEVIATION FROM SLACK BUSBAR

All generator busbars	30. (deg)

MAXIMUM TRANSMISSION LINE AND TRANSFORMER VOLTAGE ANGLE DIFFERENCE

All transmission lines and transformers.	30. (deg)

A2 HVDC LINK MODIFICATION TO IEEE 14 BUSBAR TEST SYSTEM

This modified system was used by Arrillaga et al. (1983) to test various powerflow algorithms. It is also used in chapter 6 of this thesis to evaluate the performance of an improved sequential AC/DC powerflow.

The transmission line between busbars 4 LOAD and 5 LOAD is replaced by a series connection of two transmission lines and an HVDC link.

Reactance of line from busbar 4 to rectifier AC busbar	0.3 (pu)
Reactance of line from busbar 5 to inverter AC busbar	0.3 (pu)
Filter shunt susceptance at rectifier AC busbar	0.26 (pu)
Filter shunt susceptance at inverter AC busbar	0.28 (pu)
Constant power setting at rectifier	58.6 (MW)
Constant extinction angle setting at inverter	10.0 (deg)
Resistance of HVDC line	.0033 (pu)
Rectifier transformer tap ratio	.972
Inverter transformer tap ratio	.931
Rectifier commutation reactance	.126 (pu)
Inverter commutation reactance	.0728 (pu)

A3 NEW ZEALAND SOUTH ISLAND PRIMARY SYSTEM
(1991 WINTER PEAK LOAD SCENARIO)

Power base = 100 MVA
BUSBAR DATA
Type S=Slack, G=Generator, L=Load

Busbar name	Type (SGL)	Voltage (pu)	Load MW	Load MVAR	Generation MW	Generation MVAR (min)	Generation MVAR (max)
1 STOKE	L		88.	12.			
2 KIKIWA	L		33.	-8.			
3 EYRETON	L						
4 ISLINGTO	L		428.	3.			
5 BROMLEY	L		143.	28.			
6 TIMARU	L		22.	78.			
7 LIVINGST	L						
8 TEKAPOB	G	1.045			160.	-105.	72.
9 TWIZEL	L		4.	1.			
10 OHAUA	G	1.046			264.	-170.	118.
11 OHAUB	G	1.045			212.	-132.	91.
12 OHAUC	G	1.046			212.	-132.	91.
13 BEN220	L						
14 BENTEE	L						
15 BEN33	L						
16 BEN16	L	0.96	615.	315.(HVDC)	540.	-378.	324.
17 AVIEMORE	L	1.043			220.	-133.	77.
18 BENDIGO	L		600.	300.(HVDC)			
19 LOWBURN	L						
20 CROMWELL	L		32.	5.			
21 CLYDE	G	1.046			432.	-258.	164.
22 ROXBURGH	S	1.045	-32.	-1.	0. to 200.	-131.	91.
23 NASEBY	L		-5.	0.			
24 THREEMIL	L						
25 HALFWAYB	L		65.	53.			
26 SOUTHDUN	L		76.	26.			
27 MANAPOUR	G	1.045			590.	-376.	176.
28 NORTHMAK	L		21.	8.			
29 INVERCAR	L		119.	48.			
30 TIWAI	L		480.	190.			

NEW ZEALAND SOUTH ISLAND PRIMARY SYSTEM (continued)

TRANSMISSION LINE DATA

Busbar1	Busbar2	RL (pu)	XL (pu)	BL (pu)	Maximum Current (pu)
KIKIWA	STOKE	.00759	.04354	.07237	2.863
KIKIWA	STOKE	.00759	.04354	.07237	2.863
EYRETON	KIKIWA	.02538	.11732	.23242	3.740
ISLINGTO	KIKIWA	.03330	.20070	.30177	2.863
EYRETON	ISLINGTO	.00099	.00816	.02613	7.481
ISLINGTO	TEKAPOB	.01987	.13379	.38576	4.885
ISLINGTO	TWIZEL	.01625	.13820	.42052	7.481
ISLINGTO	BROMLEY	.00203	.01655	.05383	7.481
ISLINGTO	TIMARU	.01438	.09866	.27384	4.885
BROMLEY	TWIZEL	.01710	.14059	.45081	7.481
TEKAPOB	TWIZEL	.00230	.01554	.04486	4.885
LIVINGST	TIMARU	.00784	.05377	.14924	4.885
TWIZEL	BEN220	.00429	.02935	.08201	4.885
OHAUB	TWIZEL	.00026	.00218	.00674	7.481
OHAUC	TWIZEL	.00080	.00891	.01881	6.260
OHAUA	TWIZEL	.00117	.00685	.01099	3.740
OHAUA	TWIZEL	.00117	.00685	.01099	3.740
BENDIGO	TWIZEL	.00572	.06969	.12878	4.771
BENDIGO	TWIZEL	.00572	.06969	.12878	4.771
BEN220	OHAUB	.00227	.02568	.05263	6.260
BEN220	OHAUC	.00166	.02034	.03738	6.260
AVIEMORE	BEN220	.00326	.01516	.02309	2.443
AVIEMORE	BEN220	.00326	.01516	.02309	2.443
AVIEMORE	LIVINGST	.00741	.03515	.05146	2.443
LIVINGST	NASEBY	.00897	.04251	.06241	2.443
NASEBY	ROXBURGH	.01752	.08300	.12185	2.443
BENDIGO	LOWBURN	.00124	.01515	.02800	4.771
BENDIGO	LOWBURN	.00124	.01515	.02800	4.771
CROMWELL	LOWBURN	.00053	.00647	.01196	6.260
CROMWELL	LOWBURN	.00053	.00647	.01196	6.260
CLYDE	CROMWELL	.00151	.01847	.03413	6.260
CLYDE	CROMWELL	.00151	.01847	.03413	6.260
CLYDE	ROXBURGH	.00521	.03003	.04953	3.740
CLYDE	ROXBURGH	.00521	.03003	.04953	3.740

NEW ZEALAND SOUTH ISLAND PRIMARY SYSTEM (continued)

TRANSMISSION LINE DATA (continued)

Busbar1	Busbar2	RL (pu)	XL (pu)	BL (pu)	Maximum Current (pu)
ROXBURGH	THREEMIL	.00725	.06343	.18700	4.771
ROXBURGH	THREEMIL	.00725	.06343	.18700	4.771
INVERCAR	ROXBURGH	.01915	.11252	.17814	2.863
INVERCAR	ROXBURGH	.01880	.11223	.17208	2.863
HALFWAYB	THREEMIL	.00055	.00325	.00502	3.740
SOUTHDUN	THREEMIL	.00132	.00767	.01300	3.740
HALFWAYB	SOUTHDUN	.00175	.01010	.01664	3.740
NORTHMAK	THREEMIL	.02858	.16711	.26962	3.740
NORTHMAK	THREEMIL	.02858	.16711	.26962	3.740
MANAPOUR	NORTHMAK	.01231	.08624	.23473	3.817
MANAPOUR	NORTHMAK	.01231	.08624	.23473	3.817
MANAPOUR	NORTHMAK	.01233	.08405	.24071	3.817
NORTHMAK	TIWAI	.00336	.02171	.06802	4.885
NORTHMAK	TIWAI	.00336	.02171	.06802	4.885
INVERCAR	NORTHMAK	.00098	.00631	.01978	3.817
INVERCAR	MANAPOUR	.01341	.09017	.28119	3.817
INVERCAR	TIWAI	.00226	.01456	.04596	4.885
INVERCAR	TIWAI	.00226	.01456	.04596	4.885

NEW ZEALAND SOUTH ISLAND PRIMARY SYSTEM (continued)

TRANSFORMER DATA

Busbar1	Busbar2	RL (pu)	XL (pu)	Tap ratio Bus1:Bus2	Maximum Current (pu)
BEN220	BENTEE	.0005	.0230	1.036	4.0
BEN33	BENTEE	.0005	-.0023	1.000	1.2
BEN16	BENTEE	.0005	.0103	1.000	4.0

SHUNT CAPACITOR DATA

Busbar	Susceptance (pu)
15 BEN33	1.0
18 BENDIGO	2.0

BUSBAR VOLTAGE RATINGS

Busbar 14 BENTEE 0. to 2. (pu)

All other busbars 0.95 to 1.05 (pu)

MAXIMUM GENERATOR BUSBAR VOLTAGE ANGLE DEVIATION FROM SLACK BUSBAR

All generator busbars 30. (deg)

MAXIMUM TRANSMISSION LINE AND TRANSFORMER VOLTAGE ANGLE DIFFERENCE

All transmission lines and transformers. 30. (deg)

A4 NEW ZEALAND UPPER NORTH ISLAND PRIMARY SYSTEM
(1991 WINTER PEAK LOAD SCENARIO)

Power base = 100 MVA

BUSBAR DATA
Type S=Slack, G=Generator, L=Load

Busbar name	Type	Voltage	Load		Generation		
	(SGL)	(pu)	MW	MVAR	MW	MVAR (min)	MVAR (max)
33 BREAMBAY	L		36.	14.			
34 MARSDEN	G	1.045	127.	28.	240.	-155.	107.
35 ALBANY	L		205.	-35.			
36 HENDERSO	L		220.	3.			
37 PENROSE	L		248.	108.			
38 OTAHUHU	L		28.	13.			
39 OTAHY-11	L						
40 OTA2-1101	G	1.018	46.	92.	0.	-39.	84.
T1 OTAHYTEE	L						
41 OTAFE-11	L						
T2 OTAFETEE	L						
42 OTABB211	L						
T3 OTABB2TE	L						
43 OTABB111	L						
T4 OTABB1TE	L						
44 OTA1-1101	G	1.018	265.	45.	0.	-116.	131.
45 TAKANIN1	L		42.	18.			
46 TAKANIN2	L		30.	10.			
47 RUNCIMAN	L		-600.	300. (HVDC)			
48 GLENBROO	L		141.	76.			
49 HUNTLY	L		65.	-30.			
50 HUNT-GEN	G	1.07			720.	-432.	468.
51 HAMILTON	L		294.	84.			
52 WHAKAMAR	S	1.043	-140.	12.	0. to 100.	-54.	39.

NEW ZEALAND UPPER NORTH ISLAND PRIMARY SYSTEM (continued)

TRANSMISSION LINE DATA

Busbar1	Busbar2	RL (pu)	XL (pu)	BL (pu)	Maximum Current (pu)
BREAMBAY	HENDERSO	.01549	.09398	.18416	3.740
BREAMBAY	MARSDEN	.00025	.00218	.00657	6.260
MARSDEN	ALBANY	.00878	.07171	.23323	6.260
ALBANY	HENDERSO	.00190	.01559	.05028	7.481
HENDERSO	OTAHUHU	.00226	.01907	.05794	7.176
HENDERSO	TAKANIN1	.00261	.02533	.07952	7.481
OTAHUHU	PENROSE	.00138	.00812	.01274	3.740
OTAHUHU	PENROSE	.00138	.00812	.01274	3.740
OTAHUHU	TAKANIN2	.00035	.00626	.02158	12.519
RUNCIMAN	TAKANIN1	.00038	.00667	.02297	12.519
RUNCIMAN	TAKANIN2	.00038	.00667	.02297	12.519
GLENBROO	RUNCIMAN	.00161	.01332	.04241	7.481
GLENBROO	RUNCIMAN	.00161	.01332	.04241	7.481
HUNTLY	OTAHUHU	.00790	.05420	.16658	4.885
HUNTLY	RUNCIMAN	.00385	.03251	.09880	7.481
HUNTLY	RUNCIMAN	.00385	.03251	.09880	7.481
OTAHUHU	WHAKAMAR	.03552	.16827	.24708	2.443
OTAHUHU	WHAKAMAR	.03552	.16827	.24708	2.443
OTAHUHU	WHAKAMAR	.01758	.11354	.35614	4.885
HAMILTON	HUNTLY	.00463	.03232	.10040	4.885
HAMILTON	WHAKAMAR	.00841	.05434	.17042	4.885

NEW ZEALAND UPPER NORTH ISLAND PRIMARY SYSTEM (continued)

TRANSFORMER DATA

Busbar1	Busbar2	RL (pu)	XL (pu)	Tap ratio Bus1:Bus2	Maximum Current (pu)
HUNT-GEN	HUNTLY		.0249	1.	8.34
OTAHUHU	OTAHYTEE	.00010	.02810	1.	2.09
OTA2-110	OTAHYTEE	.00080	-.0033	1.	2.00
OTAHY-11	OTAHYTEE	.00340	.06810	1.	0.70
OTAHUHU	OTAFETEE	.00032	.0193	1.	1.16
OTA1-110	OTAFETEE	.00126	.0262	1.	1.00
OTAFE-11	OTAFETEE	.00475	.0764	1.	0.60
OTAHUHU	OTABB1TE	.00390	.01738	1.	1.16
OTA1-110	OTABB1TE	.00310	.02359	1.	1.00
OTABB111	OTABB1TE	.00090	.07851	1.	0.60
OTAHUHU	OTABB2TE	.00390	.01738	1.	1.16
OTA1-110	OTABB2TE	.00310	.02359	1.	1.00
OTABB211	OTABB2TE	.00090	.07851	1.	0.60

SHUNT CAPACITOR DATA

Busbar	Susceptance (pu)
36 HENDERSON	0.75
37 PENROSE	0.75
39 OTAHY-11	0.60
43 OTABB111	0.30
44 OTA1-110	0.50
47 RUNCIMAN	3.00

NEW ZEALAND UPPER NORTH ISLAND PRIMARY SYSTEM (continued)

BUSBAR VOLTAGE RATINGS

Central virtual busbars of three winding transformers 0.0 to 2.0 (pu)

Busbar 50 HUNT-GEN 0.90 to 1.20 (pu)

All other busbars 0.95 to 1.05 (pu)

MAXIMUM GENERATOR BUSBAR VOLTAGE ANGLE DEVIATION FROM SLACK BUSBAR

All generator busbars 30. (deg)

MAXIMUM TRANSMISSION LINE AND TRANSFORMER VOLTAGE ANGLE DIFFERENCE

All transmission lines and transformers. 30. (deg)